

Modelling backward erosion piping in tidal deposits

Including the fines fraction in the onset of motion criterion to model backward erosion piping below Groningen sea dikes

Master Thesis

S. C. (Sytze) Veenland BSc

Modelling backward erosion piping in tidal deposits

Including the fines fraction in the onset of motion criterion
to model backward erosion piping below Groningen sea
dikes

by

S. C. (Sytze) Veenland BSc

in partial fulfilment of the degree of Master of Science
at the Delft University of Technology,
to be defended publicly on July 17, 2025 at 13:30

Supervisors:	dr. ir. J.P. (Juan Pablo) Aguilar-López (chair) dr. ir. A.C. (Anne-Catherine) Dieudonné ir. E.M. (Lisa) van der Linde dr. M.P. (Marc) Hijma	TU Delft TU Delft TU Delft, Deltares Deltares
Company supervisor:	ir. J. W. (Jan-Willem) Nieuwenhuis	Waterschap Noorderzijlvest
Institute:	Delft University of Technology	
Faculty:	Civil Engineering and Geosciences, Delft	
Project Duration:	Monday 11th November, 2024 - June 27, 2025	
Student number:	5096626	

Cover Image: ESRI Satellite (Esri, 2024)

Preface

This report is written for the finalization of my Master's thesis, completing the Master's programme in Civil Engineering at the Delft University of Technology. Within the Master's programme in Civil Engineering, I followed the track Hydraulic and Offshore Structures. Focusing on hydraulic structures, I spent the last six months of my Masters conducting research on the modelling of backward erosion piping in sea dikes on tidal deposits for the local water authority Noorderzijlvest.

I want to thank all supervisors for their guidance and feedback at the meetings we had during this thesis project. First, I want to thank Jan-Willem Nieuwenhuis for providing the essential information on the Groningen sea dikes from Noorderzijlvest and showing me what the sea dikes look like in reality. I want to thank Lisa van der Linde for the weekly meetings, starting with discussions about the thesis objectives and delivering interesting literature, followed by clear workshops on modelling in COMSOL, to finally the extensive feedback on my report. Furthermore I want thank Juan Pablo Aguilar-López, for guiding the deliverables in the right direction and making time for discussing data fitting and particle equilibria. I want to thank Marc Hijma for providing the data of the earlier performed tests by Deltares and his knowledge on the physical BEP experiments. I want to thank Anne-Catherine Dieudonné for her advice, which helped shape the report to a structured whole, and her constructive feedback during the meetings. Your support made the finalization of my Master's both pleasant and educational. Finally, I want to thank my family, roommates and other friends for their support during my time at the TU Delft.

*Sytze Veenland
Delft, June 2025*

Summary

Backward erosion piping (BEP) is a common failure mechanism of dikes. Dikes are currently assessed on this mechanism with the Sellmeijer 2011 rule, a method based on experiments with homogeneous deposits. However, the presence of tidal fines positively influences the cohesive strength of soils and the embedding of the soil grains in the soil matrix. For analytical assessment of BEP, a strength factor of 1.4 [-] is currently used in Dutch regulations to incorporate the extra strength due to tidal deposits. Tidal deposits also correlate with anisotropy in hydraulic conductivity due to the layering of tidal deposits. This influences flow patterns in the aquifer, thereby affecting the BEP process.

Numerical modelling of BEP has been explored in recent years, but the models do not yet include the influence of tidal fines. The additional resistance to backward erosion piping can be modelled by adapting the onset of motion criterion. This 'onset of motion criterion' describes the condition under which sediment particles begin to erode, relating the critical shear stress for which a particle is displaced to the actual shear stress acting on this particle. Tidal deposits are found to have more strength against erosion than riverine deposits due to the cohesion caused by clay particles ($d < 2 \mu\text{m}$) and due to the embedding in a fine matrix, caused by the silt fraction ($2 \mu\text{m} < d < 63 \mu\text{m}$). Results of earlier performed physical experiments are used to fit a new onset of motion criterion. These experiments established a correlation between the fines fraction and the resulting strength factor. The strength factor is the ratio between the observed critical head and the critical head as predicted by Sellmeijer's 2011 rule. The adapted onset of motion criterion is determined to be Eq. 1. Only 5% of the model-predicted critical hydraulic heads fall below those observed in physical experiments. This represents a conservative estimate.

$$\tau_c = \eta \frac{\pi}{6} \rho' g d_{70} \tan(\theta \cdot (1 + 0.023 \cdot \%_{silt}^{0.47})) + (0.047 \cdot \%_{clay}^{0.47}) \quad (1)$$

This onset of motion criterion is used in a stepwise steady-state 2D COMSOL Multiphysics model. The COMSOL model was validated by comparing its results to those from the D-Geo Flow application of Deltares by modelling the IJkdijk physical experiment. The model was run with a critical head resolution of 0.1 m. The errors of the COMSOL model, compared to the D-Geo Flow model, vary between 0 and 10% for different combinations of hydraulic conductivity (2-20 m/d) and particle size (0.1-0.3 mm) with critical hydraulic heads ranging from 1.3 to 4.5 m. Results of one of the Hedwigepolder experiments are used to look into the combination of anisotropy and the fines fraction. This shows that the developed model, including both anisotropy and the new onset of motion criterion, overestimates the critical hydraulic head. Therefore, the model used in the case study excludes anisotropy, despite it being more physically realistic. For the Groningen case, two different cross-sections are evaluated, one which was assessed as the weakest and one which was assessed as the strongest cross-section against backward erosion piping. The assessment included the foreshore, which ranged in length from 300 to almost 1000 meters. The numerical COMSOL model showed an increase in strength with a factor of about 1.5 [-] due to the updated onset of motion criterion, resulting in a slight increase over the standard 1.4 [-] strength factor as currently applied on the analytical assessment.

The model is limited in its practical usability due to several factors. Firstly, the model does not take into account the stochastic variability of important parameters, but uses only deterministic parameters. In reality, soil characteristics contain many uncertainties and these have to be taken into account to find a realistic probability of failure. There are also limitations in the understanding of the BEP process. The data used for the onset of motion criterion fit is limited in size and varies in experiment scale. Small- and medium scale tests do not contain anisotropy, but the large scale tests do. This introduces uncertainty regarding the influence of anisotropy on the experiment results. The model also does not take into account 3D BEP behaviour or time-dependencies. 2D models are less conservative than 3D models and tend to overestimate critical heads. There are also uncertainties about the shape and size of the pipe under field conditions, since during the experiment a glass or acrylic plate is used as a roof, while in the field the cover layer consists of clay or peat. Finally, the model's accuracy may be limited by numerical errors due to the mesh size or due to time step size. Numerical models may introduce discretization errors but offer flexibility in modelling complex processes. The case study specific results are limited in accuracy due to leaving out the anisotropy influences. The determined silt and clay fraction contain uncertainties, leading to uncertainty in the final outcome. Only the progression of BEP was analysed for the Groningen case; heave and uplift were not modelled.

It is recommended that future studies conduct more physical experiments on BEP. The measuring of the anisotropy in future experiments is advised. Additionally, experiments focusing on the onset of motion of a single particle in a sediment with different clay and silt fractions is recommended. For further use of the model, it is advised to increase the computational capabilities, to implement the onset of motion criterion in a 3D model and to incorporate stochastic parameters as input to determine the probability of failure instead of the deterministic critical hydraulic head.

Nomenclature

Table 1: Roman Nomenclature

Symbol	Description	Unit
A	Area of pipe cross-section in length direction	[m ²]
a	Pipe depth	[m]
a_{av}	Average pipe depth	[m]
a_{mesh}	Mesh size	[m]
C_{Bligh}	Bligh's creep coefficient	[-]
C_{Lane}	Lanes creep coefficient	[-]
C	Soil cohesion	[Pa]
D	Thickness of the granular layer	[m]
d	Grain size	[m]
d_{70}	70%-quantile of the grain size distribution by weight	[m]
$d_{70,m}$	Median d_{70} of large set of physical BEP experiments	[m]
D_h	Hydraulic diameter	[m]
D_r	Relative density	[%]
F_G	Geometrical shape factor	[-]
F_R	Resistance factor	[-]
F_S	Scale factor	[-]
g	Gravitational acceleration	[m/s ²]
h	Head	[m]
H	Hydraulic head	[m]
H_c	Critical hydraulic head	[m]
i	Hydraulic gradient	[-]
i_{pipe}	Hydraulic gradient inside pipe	[-]
k	Hydraulic conductivity	[m/s]
KAS	Particle angularity	[%]
L	Total seepage length	[m]
L_h	Horizontal seepage length	[m]
L_v	Vertical seepage length	[m]
l	Pipe length	[m]
l_{max}	Maximum pipe length	[m]
p	Pressure	[Pa]
q	Specific discharge	[m/s]
Re	Reynolds number	[-]
S_s	Specific storage	[m ⁻¹]
U	Soil uniformity coefficient	[%]
V	Flow velocity	[m/s]
x_{tip}	x-coordinate of pipe tip	[m]
% $_{clay}$	Percentage of grain size distribution by weight below 2 μm	[%]
% $_{fines}$	Percentage of grain size distribution by weight below 63 μm	[%]
% $_{mud}$	Percentage of grain size distribution by weight below 16 μm	[%]
% $_{silt}$	Percentage of grain size distribution by weight above 2 μm and below 63 μm	[%]

Table 2: Greek Nomenclature

Symbol	Description	Unit
α_x	Fraction of area of a soil particle on which the horizontal cohesive force acts	[-]
α_y	Fraction of area of a soil particle on which the vertical cohesive force acts	[-]
β_{fi}	Friction coefficient of the pipe cross-section	[-]
γ_p	Unit weight of the soil particles	[N/m ³]
γ'_p	Effective unit weight of the soil particles	[N/m ³]
γ_w	Unit weight of water	[N/m ³]
θ	Bedding angle	[deg]
η	White's coefficient	[-]
κ	Intrinsic permeability of soil	[m ²]
κ^*	Fictitious intrinsic permeability of soil	[m ²]
μ	Dynamic viscosity	[Pa·s]
ν	Kinematic viscosity	[m ² /s]
ρ'	Effective volumetric mass density	[kg/m ³]
ρ_p	Volumetric mass density of the soil particles	[kg/m ³]
ρ_w	Volumetric mass density of water	[kg/m ³]
τ	Shear stress	[Pa]
τ_c	Critical shear stress	[Pa]
ϕ	Friction angle	[deg]

List of Figures

1.1	Overview Backward Erosion Piping	1
1.2	Locations of sand boils and different deposits (Van Asselen et al., 2019)	2
1.3	Lognormal distributions through the data. The red line gives the best fit (MLE=Maximum Likelihood Estimation). The black lines give all possible outcomes based on the uncertainty in the model. (Hijma, Van Goor, De Bart, et al., 2023)	3
1.4	Approach	4
2.1	Components of early BEP models	5
2.2	Sellmeijer representation	6
2.3	Modelling framework	8
2.4	Layers formed by tidal influences (Rijkswaterstaat, 2021)	8
2.5	Depth average flow velocity in tidal flats and channels in Wadden Sea (Deltares and Rijkswaterstaat Noord Nederland, 2025)	9
2.6	USDA Soil Texture Triangle (ResearchGate, 2025)	9
3.1	Forces acting on sediment particle with the presence of clay and fines	10
3.2	Mechanism of electrostatic cohesion (Mitchell and Soga, 2005)	11
3.3	Influence of fine matrix on bedding angle (The right figure is more dense than the left figure due to the presence of fines)	11
3.4	Effect of multilayered soil structure on directional hydraulic conductivity	12
3.5	Effect of particle orientation on anisotropic hydraulic conductivity	12
3.6	Earlier found influence of fines fraction on BEP resistance	13
3.7	Conceptual framework of the physical BEP process, highlighting resistance-related factors (green) and loading-related factors (grey)	13
3.8	Equilibrium of forces on sediment particle; the pipe flow is directed in negative x-direction	14
3.9	Plots of critical head with experimental- and predicted results (fitted to the lowest 5% of observed H_c values)	17
3.10	Plots of strength factor with experimental- and predicted results (fitted to the lowest 5% of observed H_c values)	17
3.11	Plots of the influence on silt- and clay fractions on the strength factor (fitted to the lowest 5% of observed H_c values)	18
4.1	Groundwater flow	19
4.2	Schematic representation of pipe flow	20
4.3	Pipe growth due to erosion	21
4.4	Computational mesh in COMSOL	22
4.5	Flowchart for pipe shape	22
4.6	Flowchart for permeability	23
4.7	Flowchart for erosion	23
4.8	Determination of τ_{max}	24
5.1	Geometry of IJkdijk	26
5.2	Results from COMSOL model. The arc length starts at the outer dike toe (0 m) and continues towards the inner dike toe (15 m)	27
5.3	Pressure head [m] output from COMSOL at step 0 and 12	27
5.4	Critical head values from COMSOL for IJkdijk with varying d_{70} and k	28
5.5	D-Geo Flow results with $k=10$ [m/d] and $d_{70}=0.180$ [mm].	28
5.6	Critical head values from D-Geo Flow for IJkdijk with varying d_{70} and k	29
5.7	Model comparison between COMSOL, D-Geo Flow and Sellmeijer 2011	29
5.8	Errors between COMSOL, D-Geo Flow and Sellmeijer 2011, found as validation results	30
5.9	Model geometry of Hedwigepolder experiment	30
5.10	Hydraulic head in Hedwigepolder experiment according COMSOL model	31
5.11	Contour plot of critical head values in the Hedwigepolder experiment, simulated in COMSOL (fines included, anisotropy excluded)	32
6.1	Section D, the dike section with highest probability of failure (Google, 2025)	33
6.2	History Section D (Topotijdreis, 2025)	33

6.3	Results of latest BEP assessment (Noorderzijlvest, 2022b) (in Dutch)	34
6.4	The assessment results per section for the BEP mechanism (Noorderzijlvest, 2022b). The sections evaluated as being the strongest and weakest are indicated with location A and B. (in Dutch)	34
6.5	Subsurface profile example (B63807 00.00-05.00) NAP +1.15m to NAP -2.85m (Wiertsema & Partners, 2018)	35
6.6	Particle grading (MB63807 M006-b) NAP -1.22m to NAP -1.45m (Wiertsema & Partners, 2018) (in Dutch)	35
6.7	The locations selected for modelling in the Groningen dike. The upper figure is the top view, middle figure is the length profile at the crest and the lower figure the length profile at the inner toe.	36
6.8	Soil legend (in Dutch)	36
6.9	Aerial view of the foreshore in front of the Groningen sea dikes (Google, 2025)	37
6.10	Model schematization (not to scale)	37
6.11	Contour plots of critical heads dependent on silt and clay fractions	38
B.1	Plots of critical head with experimental- and predicted results (50% conservative)	66
B.2	Plots of strength factor with experimental- and predicted results (50% conservative)	66
B.3	Plots of the influence on silt- and clay fractions on the strength factor (50% conservative)	67
B.4	Plots of critical head with experimental- and predicted results for mud and fines (95% conservative)	67
B.5	Plots of strength factor with experimental- and predicted results for mud and fines (50% conservative)	68
B.6	Plots of the influence on fines- and mud fractions on the strength factor (95% conservative)	68

List of Tables

1	Roman Nomenclature	iii
2	Greek Nomenclature	iv
3.1	Soil Parameters for Training Group Experiments	16
3.2	Soil Parameters for Validation Group Experiments	16
4.1	Model variables	24
4.2	Stepwise steady-state events	25
5.1	General parameters	26
5.2	IJkdijk parameters	26
5.3	Hedwigepolder parameters	30
5.4	Hedwigepolder results	31
6.1	Safety limits trajectory 6-6	34
6.2	Groningen case parameters (warning level and inland water level are statistically safe, other parameters are mean values)	38

Contents

Preface	i
Summary	ii
Nomenclature	iii
List of Figures	v
List of Tables	vii
1 Introduction	1
1.1 Context	1
1.2 Research problem	3
1.3 Research aim, objective and questions	3
1.4 Research scope	4
1.5 Index	4
2 Theory and Background	5
2.1 Background of BEP modelling	5
2.1.1 Observations and analytical models	5
2.1.2 Numerical models	7
2.2 Tidal deposits	8
2.2.1 Formation of tidal flats and channels	8
2.2.2 Sediment composition	9
3 Onset of Motion Criterion Adaptation	10
3.1 Introduction	10
3.1.1 Physics	10
3.1.2 Physical experiments results	12
3.1.3 Tidal sands framework	13
3.2 New Onset of Motion Criterion	13
3.2.1 Added parameters in Onset of Motion Criterion	13
3.2.2 Fitting the Onset of Motion Criterion	15
4 Method	19
4.1 Model physics	19
4.1.1 Groundwater flow	19
4.1.2 Pipe flow	19
4.1.3 Erosion	20
4.1.4 Boundary conditions	21
4.1.5 Mesh	22
4.2 Model variables	22
4.3 Pipe progression events	25
5 Model Validation	26
5.1 D-Geo Flow validation of basic model	26
5.1.1 IJkdijk geometry	26
5.1.2 COMSOL outputs	27
5.1.3 D-Geo Flow outputs	28
5.1.4 Model errors	29
5.2 Validation of New Onset of Motion Criterion	30
6 Case Study	33
6.1 Background Groningen sea dikes	33
6.1.1 Introduction	33
6.1.2 History	33
6.1.3 Latest assessment	34
6.1.4 Technical aspects	35

6.2	Geometry and materials	36
6.2.1	Aquifer	36
6.2.2	Inflow and exit point	36
6.2.3	Geometry parameters	37
6.3	Results	38
7	Discussion	39
7.1	Soil profile heterogeneities	39
7.2	Physical understanding of BEP process.	39
7.2.1	Limited dataset of tidal deposit experiments	39
7.2.2	3D effects and time-dependencies	39
7.2.3	Pipe size and shape	39
7.3	Numerical limitations	40
7.4	Case study	40
8	Conclusion and Recommendations	41
8.1	Conclusion	41
8.1.1	How is backward erosion piping currently modelled?	41
8.1.2	How do tidal deposits influence soil properties?	41
8.1.3	When will erosion progress in soils with a fines fraction?	41
8.1.4	What is the current water safety situation at the Groningen sea dike?	41
8.1.5	How to develop and validate a numerical model to assess BEP in tidal deposits?	42
8.1.6	How are the Groningen sea dikes evaluated on safety against BEP according to a numerical model for BEP in tidal deposits?	42
8.1.7	Main research question	42
8.2	Recommendations	42
8.2.1	Future physical BEP experiments	42
8.2.2	Future physical experiments on particle scale	42
8.2.3	Increase computational capabilities	43
8.2.4	Implementation in a 3D model	43
8.2.5	Implementation of statistical analysis	43
8.2.6	Case study	43
	References	46
	Appendix	46
A	Python code: Onset of motion criterion fit	47
B	Other fits for onset of motion criterion	66
B.1	50% percentile fit	66
B.2	95% fit on mud and fines.	67
C	Python code: run COMSOL for contour plot	69

Introduction

1.1. Context

Backward erosion piping (BEP) is an internal erosion mechanism for soil embankments. This mechanism occurs beneath a dike, directly under a cohesive and nearly impermeable soil layer during high water levels. The high water levels result in a large hydraulic gradient, causing groundwater flow underneath a dike. The hydraulic gradient is the difference in water head between the inside and outside of the embankment divided by the seepage length. The seepage length is the length over which the groundwater flows between the inner and the outer side of the embankment. The critical head difference is the difference in hydraulic head over the embankment at which the BEP process causes dike failure. Due to the high hydraulic gradient, the groundwater flow will converge to the end of the cohesive layer (blanket layer) or to a crack in this layer. The opening in the blanket layer can be caused by uplift of the blanket layer. This groundwater flow causes the soil particles in the porous aquifer to fluidize and erode. The fluidization of the soil at the groundwater exit point is referred to as heave. A pipe can only form when the porous layer lies beneath a cohesive blanket layer. The blanket layer will function as the roof of the pipe. The formation of the pipe will be initiated at the side of the dike with the lowest hydraulic head, at the groundwater exit point. The pipe will progress towards the outside of the dike if the onset of motion criterion is met. The onset of motion criterion is a physical description of the condition under which sediment particles begin to erode. This may be expressed as a local critical hydraulic gradient, but could also be related to the critical shear stress of the sediment particles. The pipe will continue to grow and eventually reach the upstream side of the dike. This causes the pipe flow to increase even more, resulting in more erosion causing the deepening and widening of the pipe. Finally, the pipe will cause the dike to breach. The BEP process is shown in Figure 1.1.

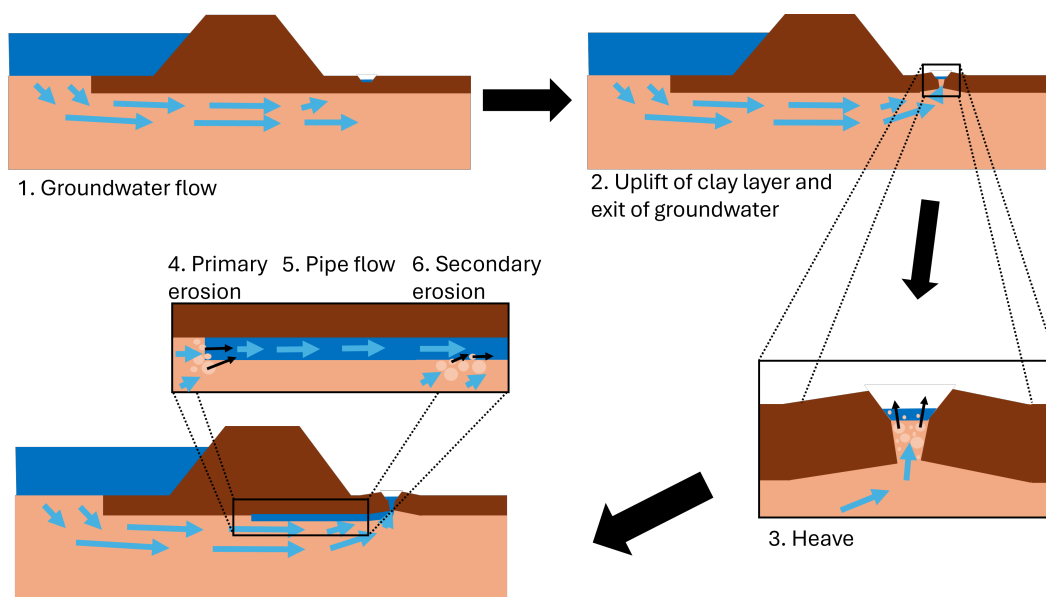


Figure 1.1: Overview Backward Erosion Piping

The failure mechanism of backward erosion piping is, according to Dutch regulations, assessed using the 2011 Sellmeijer rule, which is based on a two-force balance equation (Rijkswaterstaat, 2021; Sellmeijer et al., 2011). The two forces considered are the drag force due to pipe flow and the particle weight. In the earlier Sellmeijer rule from 1988, a four-forces equation is used with the added influence of the horizontal and vertical seepage gradient (Sellmeijer, 1988). The Sellmeijer rule models the erosion of soil particles that leads to pipe formation beneath a dike. The Sellmeijer rule of 2011 assumes the following:

- 2D flow and erosion processes;
- Steady-state;
- Darcyan groundwater flow;
- Linear equations for laminar pipe flow (Hagen-Poiseuille);
- Only secondary erosion is considered, using White's erosion criterion.

However, the physical process of backward erosion piping is more complex. One complexity involves the 3D behaviour of the groundwater flow, allowing groundwater to converge toward the pipe from multiple directions and thus causing a higher loading of the sediment particles near the pipe. Another is the 3D formation of pipes, causing the pipe growth to follow the path of least resistance rather than a straight line. A third complexity is the time-dependent pipe progression, which can cause the pipe to progress at a different pace for short periods of high water. Finally, diverse sediment properties can lead to differences in the backward erosion piping process. The Sellmeijer rule does not fully account for these physical processes. The Sellmeijer rule is calibrated on homogeneous, sieved sands without a fine fraction and is applicable on soils with a d_{70} (70%-quantile of the grain size distribution by weight) of 0.15 to 0.43 mm (Sellmeijer et al., 2011). The tidal deposits on the Northern and Western coasts in the Netherlands have different properties than these homogeneous sands with no fine sediment. Figure 1.2 shows the distribution of sediment types in the Netherlands. Locations of observed sand boils are also included in this figure. A sand boil forms at the pipe exit due to the accumulation of eroded sediment particles transported through the pipe, and is therefore an indicator of BEP.



Figure 1.2: Locations of sand boils and different deposits (Van Asselen et al., 2019)

Tidal deposits are formed by slow, fluctuating tidal motion and are often deposited in thin layers on tidal flats. Tidal fines can also be deposited in tidal channels. Tidal deposits in channels often consist of larger particles than the deposits in tidal flats, since the flow velocity is higher in the channels than in the flats. Tidal deposits differ from these homogeneous deposits in cohesion due to the clay particles fraction and in bedding angle due to the influence of fines on the embedding in the soil matrix. Clay particles are plate-shaped and typically smaller than $2 \mu\text{m}$. Silt particles are sized between $2 \mu\text{m}$ and $63 \mu\text{m}$. Fines are all soil particles smaller than $63 \mu\text{m}$, consisting of both plated clay particles and granular silt particles. The grain size distribution curve of tidal fines can vary significantly below the $63 \mu\text{m}$ threshold. Therefore, two soils with identical fines content can have a different clay/silt ratio. The mud content consists of the particles smaller than $16 \mu\text{m}$. Mud is sometimes used in Deltares literature and observed to be an important parameter to relate the added strength of tidal deposits to the resistance against BEP (Hijma, Van Goor, De Bart, et al., 2023).

Tidal deposits are also characterized by the multilayeredness of the dike foundation, which is the variation in soil layer types at the meter scale. This can cause a difference between vertical and horizontal hydraulic permeability. There are also small scale variations in hydraulic permeability due to small clay and sand lenses and the arrangement of individual sediment particles. This variation is referred to as anisotropy in this report. Multilayeredness and anisotropy cause differences between the vertical and horizontal hydraulic conductivity. Generally, the vertical hydraulic conductivity will be lower than the horizontal hydraulic conductivity. The presence of tidal fines, anisotropy and multilayeredness may lead to an overestimation of the failure probability of dikes founded on tidal deposits, po-

tentially leading to misclassification under national regulations.

In recent physical experiments (Hijma, Van Goor, De Bart, et al., 2023; Lucker and Robbins, 2023), the effect of the presence of a certain fines fraction on the resistance against piping was evaluated. The experiment results show a significant increase in resistance. A strength factor of 1.4 [-] may be used on the calculated critical head by the Sellmeijer rule to analytically incorporate the added strength (Rijkswaterstaat, 2023). This value represents a conservative estimate, based on the 5% lower bound of the experimental results. The results of the large scale physical experiments by Deltares in the Hertogin Hedwigepolder are illustrated in Figure 1.3. The influence of a fines fraction is not yet implemented in numerical models, which are able to give a more tailored safety assessment. This is a motivation to further explore the added resistance as a result of the presence of tidal fines.

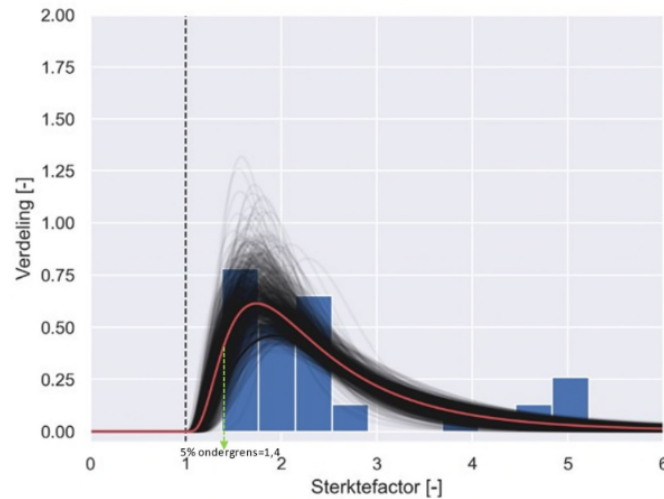


Figure 1.3: Lognormal distributions through the data. The red line gives the best fit (MLE=Maximum Likelihood Estimation). The black lines give all possible outcomes based on the uncertainty in the model. (Hijma, Van Goor, De Bart, et al., 2023)

Sea dikes are an important part of the primary flood defences in the Netherlands. Failure of these flood defences could result in severe flooding. During the last round of sea dike assessments in Groningen for Waterschap Noorderzijlvest (regional water authority), multiple dike sections were assessed as not meeting the national safety standards (Noorderzijlvest, 2022b). One of these sections does not comply with the current standards due to the failure mechanism of backward erosion piping, while the presence of tidal deposits may provide additional resistance against this erosion mechanism. Other sections do not comply with the standards due to macro-instability or failure of the grass revetment.

1.2. Research problem

Currently, the assessment of dikes does not fully take into account the extra resistance due to the presence of tidal sands with higher fines fractions in the onset of motion criterion. A factor of 1.4 [-] is now used in analytical assessments as an additional strength factor for all dikes with the presence of fines, regardless of the specific fines content (Hijma, Van Goor, De Bart, et al., 2023). This factor is a 5% lower limit, while in most cases the added resistance is higher according to the physical experiments. This assessment method thus does not capture the full behaviour of BEP in tidal deposits. Current numerical models for BEP also do not capture the combined influence of multilayeredness, anisotropy, and fines. However, this could be of great value in understanding the BEP process, since numerical models can provide a more tailored assessment of specific dike cross-sections.

1.3. Research aim, objective and questions

The aim of this research is to understand and quantify the impact of the fines fraction on the resistance against backward erosion piping by adapting the onset of motion criterion used in numerical modelling.

The small scale physical experiments by Lucker and Robbins (Lucker and Robbins, 2023), the small and medium scale experiments in the Deltares facilities, and the large scale experiments at the Hedwigepolder are used to fit a suitable onset of motion criterion based on the fines fraction. This onset of motion criterion will be implemented in a numerical model created with COMSOL Multiphysics 6.2. The model will be used to reassess the failure mechanism of backward erosion piping of dike sections in Groningen which do not meet the current safety standards.

The main research question is:

- What is the impact of an onset of motion criterion including the fines fraction on the assessment of backward erosion piping using numerical models?

With the sub-questions:

- How is backward erosion piping currently modelled?
- How do tidal deposits influence soil properties?
- When will erosion progress in soils with a fines fraction?
- How to develop and validate a numerical model to assess BEP in tidal deposits?
- How are Groningen sea dikes currently assessed on water safety?
- How are the Groningen sea dikes evaluated on safety against BEP according to a numerical model for BEP in tidal deposits?

An overview of the approach can be found in Figure 1.4.

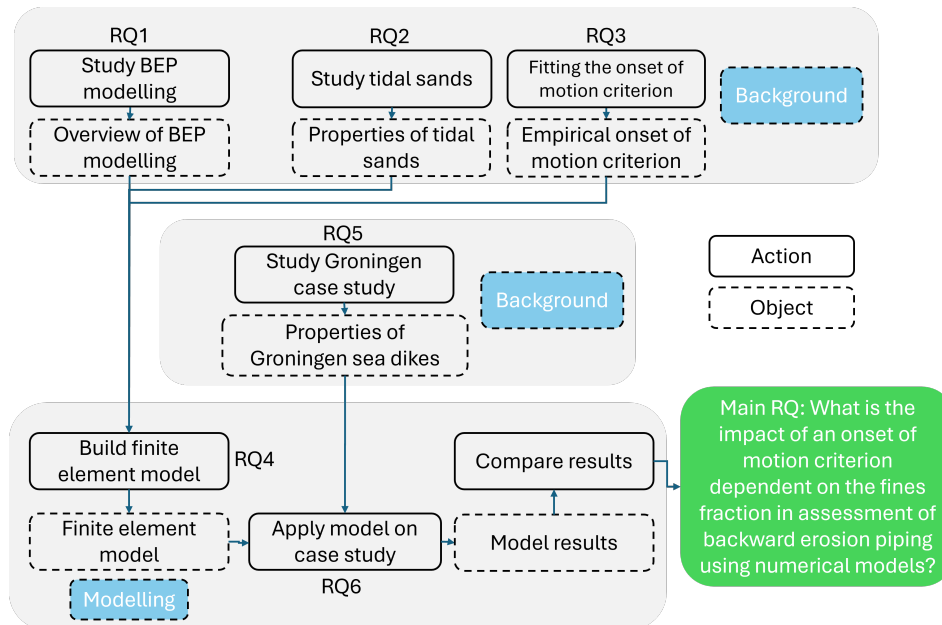


Figure 1.4: Approach

1.4. Research scope

The scope of the research is defined in this section. The research will be limited to the content mentioned in this section. A numerical model will be developed to be able to more accurately assess the strength against backward erosion piping of dikes on tidal deposits. The added piping resistance is determined using a theoretical study of earlier performed physical experiments and numerical modelling. The influence of the tidal fines is captured in the onset of motion criterion. The numerical model will be stepwise steady-state, 2D and is constructed with COMSOL Multiphysics 6.2. The numerical model will be applied in a reassessment of the critical hydraulic head for sea dikes on tidal deposits in Groningen. The numerical model should be applicable for tidal flats as well as tidal channel deposits. In the current assessment method, these deposits are evaluated differently.

Outside the scope of the research is:

- The influence of multilayeredness will not be part of the to be determined onset of motion criterion.
- No extra physical experiments are performed for this research, besides the ones reported in literature.
- Other effects such as the 3D effects and the time dependency are not part of the assessment. 3D effects have a negative influence on the resistance against BEP, excluding 3D effects can cause overestimation of the strength against BEP. 3D effects are excluded due to their complexity. Time-dependency will have a positive effect on the resistance due to the short duration of coastal high water levels.
- Other erosion mechanisms are not assessed.

1.5. Index

Chapter 2 works on the literature review and looks into the background of BEP and tidal sands. The influence of tidal sands on the onset of motion criterion and the adaptation of this criterion is executed in Chapter 3. The method of the model development is worked out in Chapter 4. This results in the development and validation of the numerical model in Chapter 5. The model is then applied on the Groningen case in Chapter 6. The method and results are discussed in Chapter 7. In Chapter 8 the conclusions are drawn and recommendations are made.

Theory and Background

2.1. Background of BEP modelling

This section gives an overview of the historical development in backward erosion piping modelling and the current state-of-the-art. The background and theory is divided in paragraphs on the history of new observations, the development of new analytical models and the development of numerical models. More extensive BEP overviews are available (Van Beek, Knoeff, and Schweckendiek, 2011; Allan, 2018; Vandenboer, 2019; Robbins, 2022).

2.1.1. Observations and analytical models

Early 20th century

The earliest observations of backward erosion piping were studied by Clibborn (Clibborn and Beresford, 1902), he already related the seepage length and hydraulic head to the possibility of dike failure. Failures of embankments alongside irrigation channels were observed in India, giving an initiation to the research of soil erosion in dams. This was followed by empirical studies of dam failures by Bligh, Griffith and Lane (Bligh, 1910; Griffith, 1914; Lane, 1935).

The first observations in India led to empirical equations of backward erosion piping by Bligh (Eq. 2.1) (Bligh, 1910). He related the maximum hydraulic head to the seepage length over an embankment via a creep coefficient. This creep coefficient is dependent on the coarseness of the soil and is empirically fitted on observations from real life failures of weirs and dams. Coarser soils have higher creep coefficients and give more resistance to BEP due to the larger soil particle weight.

$$L = \frac{H}{C_{Bligh}} \quad (2.1)$$

In which:

L : Seepage length [m]

H : Hydraulic head [m]

C_{Bligh} : Bligh's creep coefficient [-]

Lane updated the relationship found by Bligh and used more observations from real life embankment failures to update the creep coefficients (Eq. 2.2) (Lane, 1935). Lane found that the vertical seepage length contributes more to the resistance against piping erosion than the horizontal seepage length and therefore he scaled the horizontal seepage length with a factor of $\frac{1}{3}$. A schematization of the components Bligh and Lane took into account is displayed in Figure 2.1, in this case L_v equals 2·'depth'.

$$L_w = \sum \left(L_v + \frac{1}{3}L_h \right) = \frac{H}{C_{Lane}} \quad (2.2)$$

In which:

L_w : Weighted seepage length [m]

L_h : Horizontal seepage length [m]

L_v : Vertical seepage length [m]

C_{Lane} : Lane's creep coefficient [-]

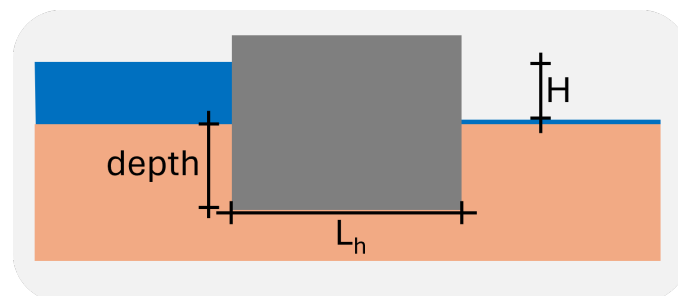


Figure 2.1: Components of early BEP models

Late 20th century

In the second half of the 20th century, multiple physical backward erosion piping experiments were conducted in Germany (Miesel, 1978; Muller-Kirchenbauer, 1980; Hanses, 1985), the USA (Townsend et al., 1981; Schmertmann, 1995) and the Netherlands (Wit, 1984; Silvis, 1991). Part of the new research focused on the influence of soil characteristics on the critical head. They looked into the grain size, porosity, dimensions of the sand bed and type of exit point (Wit, 1984). Other studies focused on the erosion process, differentiating the primary and secondary erosion (Hanses, 1985). Primary erosion is the erosion that occurs at the tip of the pipe and that feeds loose grains in the bottom of the channel, causing the pipe to lengthen. Secondary erosion is the erosion along the pipe, causing the pipe to widen and deepen. During this period, new assessment rules were defined by Sellmeijer and Schmertmann (Sellmeijer, 1988; Schmertmann, 2000).

At the end of the 20th century analytical models were developed by Sellmeijer (Eq. 2.3) and Schmertmann (Sellmeijer, 1988; Sellmeijer et al., 1989; Sellmeijer and Koenders, 1991; Schmertmann, 2000). The model of Sellmeijer used the particle equilibrium with a four-forces model consisting of the horizontal drag force, vertical particle weight and horizontal and vertical seepage gradients to check for erosion. Analytical equations for incipient sediment motion, developed by Shields and White, were used to model the behaviour of sediment particles in a more detailed manner (Shields, 1936; White, 1940). The influences on BEP were captured in 3 factors by Sellmeijer. These factors show the influence of the resistance, scale and geometry on the BEP process.

$$\begin{aligned} \frac{H_c}{L} &= F_R F_S F_G \\ F_R &= \frac{\gamma_p}{\gamma_w} \tan(\theta) \\ F_S &= \eta \frac{d_{70}}{\sqrt[3]{\kappa L}} \\ F_G &= [0.68 - 0.1 \ln(F_S)] \left(\frac{D}{L} \right)^{\frac{0.28}{\left(\frac{D}{L} \right)^{2.8} - 1}} \end{aligned} \quad (2.3)$$

In which:

F_G : Geometry factor [-]

F_R : Resistance factor [-]

F_S : Scale factor [-]

L : Seepage length [m]

H_c : Critical hydraulic head [m]

D : Thickness of the granular layer [m]

γ_p : Unit weight of the soil particles [kN/m³]

γ_w : Unit weight of water [kN/m³]

η : White's coefficient [-]

θ : Bedding angle [°]

d_{70} : 70%-quantile of the grain size distribution by weight [m]

κ : Permeability [m²] ($\kappa = \frac{k \rho_w g}{\mu}$)

k : Hydraulic conductivity [m/s]

ρ_w : Volumetric mass density of water [kg/m³]

g : Gravitational acceleration [m/s²]

μ : Dynamic viscosity [Pa·s]

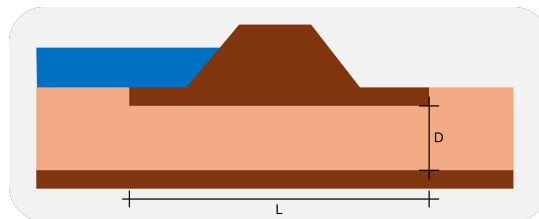


Figure 2.2: Sellmeijer representation

Early 21st century

From 2000 onward, research on backward erosion piping continued. Existing models to assess backward erosion piping have been updated with observations in physical experiments. These experiments have been conducted by Van Beek, Allan, Robbins and more (Van Beek, Knoeff, and Sellmeijer, 2011; Van der Zee, 2011; Van Beek, 2015; Van Beek et al., 2019; Allan, 2018; Robbins et al., 2018; Robbins et al., 2020; Vandenboer, 2019). This research

helped to update the analytical model of Sellmeijer from 1988 to the model of 2011 (Sellmeijer et al., 2011; Van Beek, Knoeff, and Sellmeijer, 2011). The model was mainly updated by leaving out the forces induced by the horizontal and vertical seepage gradient, updating the model from a 4-forces model to a 2-forces model. Additionally, the model was updated by adding empirical correction factors for the relative density, soil uniformity, particle angularity and the particle size as used in experiments. Other studies were conducted to further develop the understanding of the BEP process. These studies helped to capture 3D effects and time-dependency in numerical models.

In 2011 the Sellmeijer rule of 1988 was adapted based on physical experiments from Van Beek, resulting in Eq. 2.4 (Van Beek, Knoeff, and Sellmeijer, 2011; Sellmeijer et al., 2011). In current Dutch practice, the terms containing D_r (relative density), U (soil uniformity) and KAS (particle angularity) are not used in the assessment.

$$\begin{aligned} \frac{H_c}{L} &= F_R F_S F_G \\ F_R &= \eta \frac{\gamma'_p}{\gamma_w} \tan(\theta) \left[\frac{D_r}{D_{r,\mu}} \right]^{0.35} \left[\frac{U}{U_\mu} \right]^{0.13} \left[\frac{KAS}{KAS_\mu} \right]^{-0.02} \\ F_S &= \frac{d_{70}}{\sqrt[3]{\kappa L}} \left[\frac{d_{70,\mu}}{d_{70}} \right]^{0.6} \\ F_G &= 0.91 \left(\frac{D}{L} \right)^{\frac{0.28}{\left(\frac{D}{L} \right)^{2.8} - 1} + 0.04} \end{aligned} \quad (2.4)$$

In which:

D_r : Relative density of the soil [-]

U : Soil uniformity coefficient [-]

KAS : Particle angularity [-]

$d_{70,\mu}$: Mean 70%-quantile of the grain size distribution by weight of a set of experiments [m]

2.1.2. Numerical models

The development of numerical BEP models began in the early 21st century. Numerical models are able to capture more complex processes, which helps model the continuous interaction between groundwater flow, pipe flow and erosion. Numerical models are however not as exact as analytical models due to discretization errors. However, due to the complexity of the interaction of processes in BEP, numerical models are able to combine the different physical processes in 3D and in time, which analytical models cannot achieve. This section elaborates on the main aspects of numerical modelling of BEP. Other overviews on BEP modelling are available (Van Beek and Hoffmans, 2017; Van der Linde et al., n.d.).

Sellmeijer developed the first numerical model for backward erosion piping in 2006 and also applied neural networks in his research (Sellmeijer, 2006). Two distinct domains are defined to model backward erosion piping, namely the aquifer and the pipe. Groundwater flow has to be modelled in the aquifer domain. Pipe flow and erosion have to be modelled in the pipe domain. Some general model choices have to be made, namely the model dimensions and its time-dependence.

The numerical model using Sellmeijers conceptualization assumes the following:

- 2D flow and erosion processes - **general**;
- Steady-state (by stepwise evaluating the steady-state rule with different water levels, a quasi steady-state model is obtained) - **general**;
- Darcy aquifer flow - **groundwater flow**;
- Linear equations for laminar pipe flow (Hagen-Poiseuille) - **pipe flow**;
- Only secondary erosion is considered, using White's erosion criterion - **erosion**.

Following Sellmeijer's work, multiple numerical models have been developed. Bersan used COMSOL Multiphysics to develop a BEP model (Bersan et al., 2013). Van Esch developed a 2D stepwise steady-state model with Darcy aquifer flow and Poiseuille pipe flow with only secondary erosion (Van Esch et al., 2013). Aguilar-Lopez developed a similar model, but only steady-state (including a sensitivity analysis on the pipe shape and size) and looked into using neural networks in BEP (Aguilar-López et al., 2016). Wewer used a 2D model with Darcy aquifer flow, linear pipe flow equations with secondary erosion only and added time-dependence and sediment transport equations (Wewer et al., 2021). Robbins used a stepwise steady-state model with Darcy aquifer flow, linear equation pipe flow, added a third dimension and used primary erosion (Robbins, 2022). Pol combined both 3D and time-dependence in a model with only secondary erosion and using transport equations (Pol et al., 2024).

The previous paragraph showed that numerical models generally consist of three main processes: groundwater flow, pipe flow and erosion. Next to these processes, a choice has to be made on the dimensions and time-dependence of the model. 2D models are less conservative than 3D models, due to the concentration of groundwater flow in the 3D domain at the pipe. Numerical models can be steady-state, stepwise steady-state or time-dependent. An overview of numerical BEP models is shown in Figure 2.3. This overview also shows the area of influence of tidal deposit characteristics on BEP models. The hydraulic conductivity (k), anisotropy and multilayeredness will influence the groundwater flow. The characteristic particle diameter (d_{70}) and the fraction of fines, mud and clay will influence the erosion process.

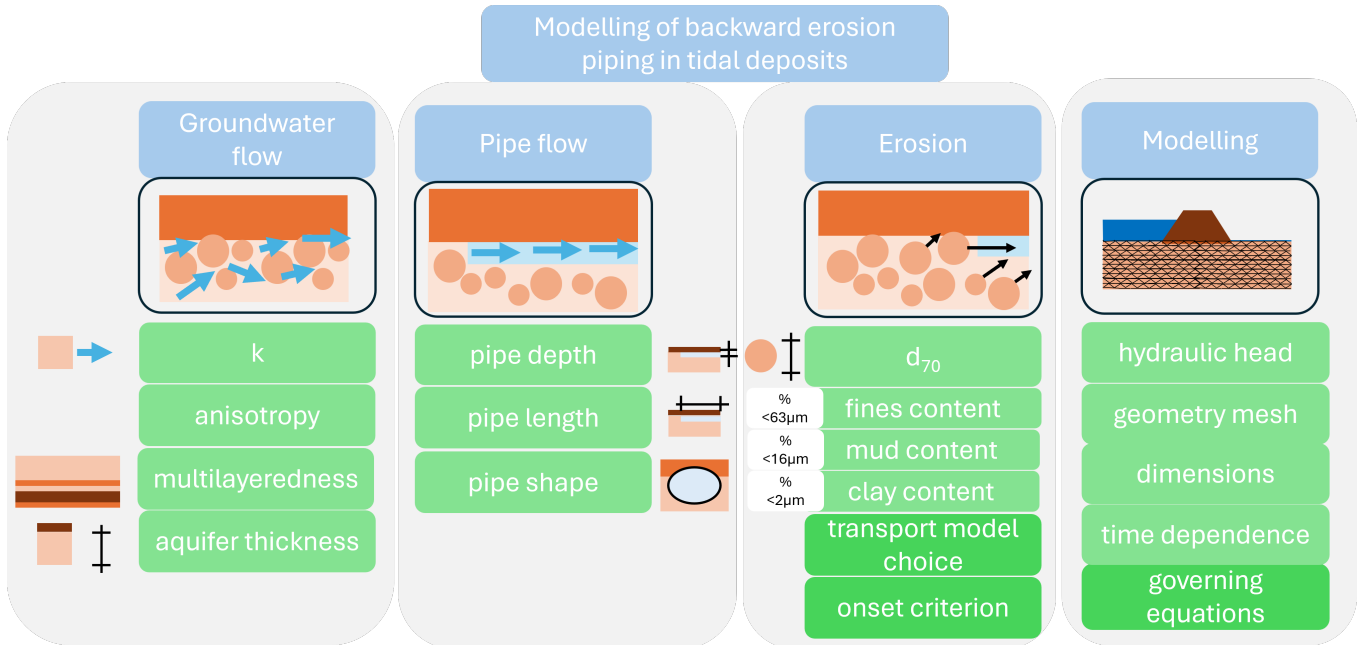


Figure 2.3: Modelling framework

2.2. Tidal deposits

2.2.1. Formation of tidal flats and channels

Sea levels all over the world are slowly oscillating due to gravitational attraction from primarily the Moon and, to a lesser extent, the Sun (Davis Jr. and Dalrymple, 2012). This oscillating behaviour causes water particles to flow. The flow of water is able to transport sediment particles towards the coast with help from the lift force acting on the particles. When the flow decelerates near the shore, this lift force decreases in magnitude, causing sediment to settle on the sea bottom, forming tidal deposits. The magnitude of tidal movement is time-dependent, resulting in time-dependent settlement of sediment particles. When the tidal movement is fast, only heavier particles settle. When the tidal movement slows down, fine particles are also able to settle. This results in layeredness in tidal deposits as seen in Figure 2.4. During storms, bigger waves will reach the shore. Higher waves cause higher orbital velocities at the sea bottom, causing larger particles to be moved towards the shore. Storms therefore are able to deposit sand layers with larger particle sizes.

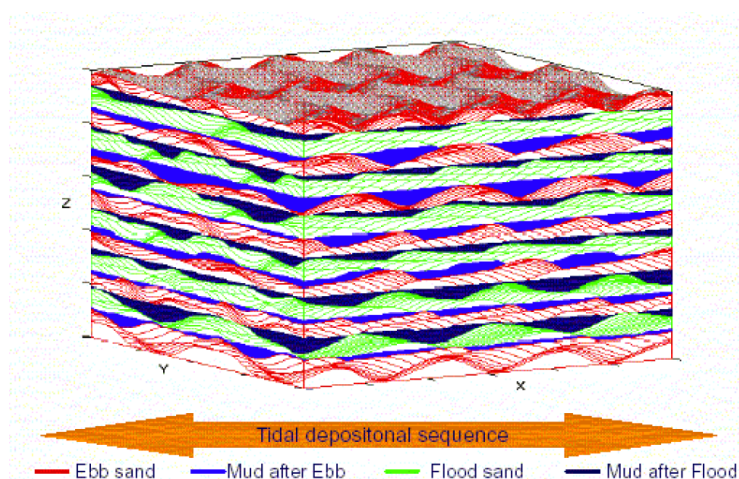


Figure 2.4: Layers formed by tidal influences (Rijkswaterstaat, 2021)

Tidal channels are formed where tidal flows concentrate and cause more erosion to the sea bottom. The flow velocity is higher in these channels, restricting the small particles from settling at these locations. This causes the sediment in tidal channels to be coarser than in tidal flats. The current shape of tidal channels in front of the Groningen shore is shown in Figure 2.5.

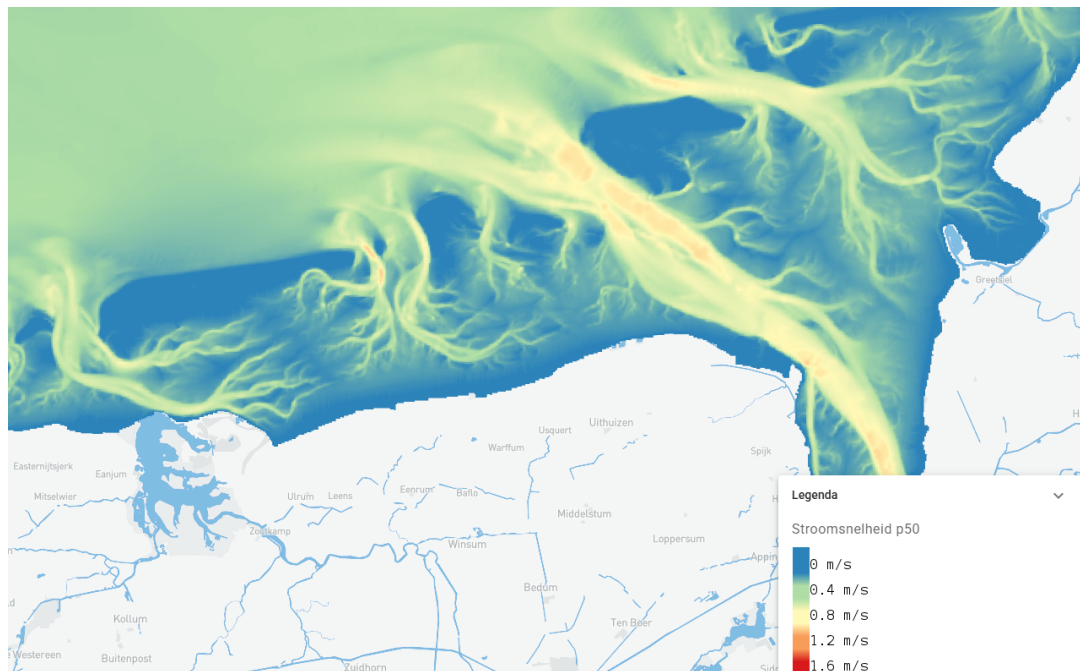


Figure 2.5: Depth average flow velocity in tidal flats and channels in Wadden Sea (Deltares and Rijkswaterstaat Noord Nederland, 2025)

2.2.2. Sediment composition

The sediment deposited by tidal motion consists of clay-, silt- and sand particles. Using the percentages of different particle fractions in a sediment, a soil type can be classified following Figure 2.6. Not all soil types are prone to backward erosion piping. Clay sediments have high cohesion and low permeability, causing them not to erode like homogeneous sand sediment would. In reality, sediments are graded and contain multiple types of particles. Aquifers which are prone to piping consist of sand or loamy sand, this corresponds with a clay fraction of less than 15% according to Figure 2.6. In the previous Dutch norms, a clay fraction larger than 8% was classified to be clay (Normalisatie-instituut, 1989). In the Hedwigepolder experiment, it has been found that the roof of the pipe contained an 8% clay fraction (Hijma, Van Goor, Pruijn, Van Beek, and Wiersma, 2023). This gives reason to assume that only soils with a lower clay fraction than 8% are prone to backward erosion piping.

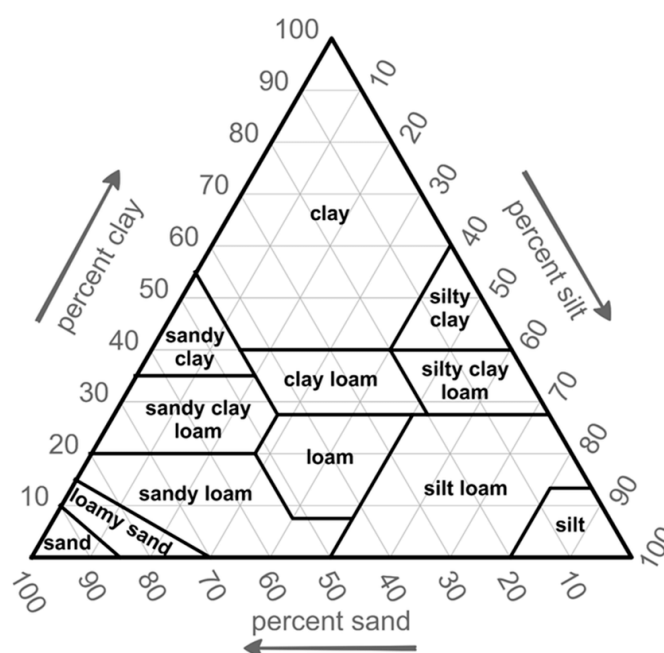


Figure 2.6: USDA Soil Texture Triangle (ResearchGate, 2025)

Onset of Motion Criterion Adaptation

3.1. Introduction

In this section, the current knowledge on the influence of fines on the onset of motion criterion in backward erosion piping is introduced. The influence of fines on the backward erosion piping process can be split in the added cohesion, the embedding of a soil particle in a fine soil matrix and changes in hydraulic conductivity. Observations on these influences are obtained with physical experiments, which are briefly discussed below. Finally a framework on the influence of tidal deposits on BEP is constructed.

3.1.1. Physics

Multiple forces act on a sediment particle subject to erosion in a backward erosion piping channel. The seepage and pipe flow cause a lift force and a drag force to be acting on the particle. These two forces are counteracted by the weight of the particle and the resulting normal force as applied by adjacent particles. The lift force is assumed to be negligible compared to the drag force, normal force and weight. A cohesion force is present for piping in sediments with plated clay particles. The forces are schematized in Figure 3.1.

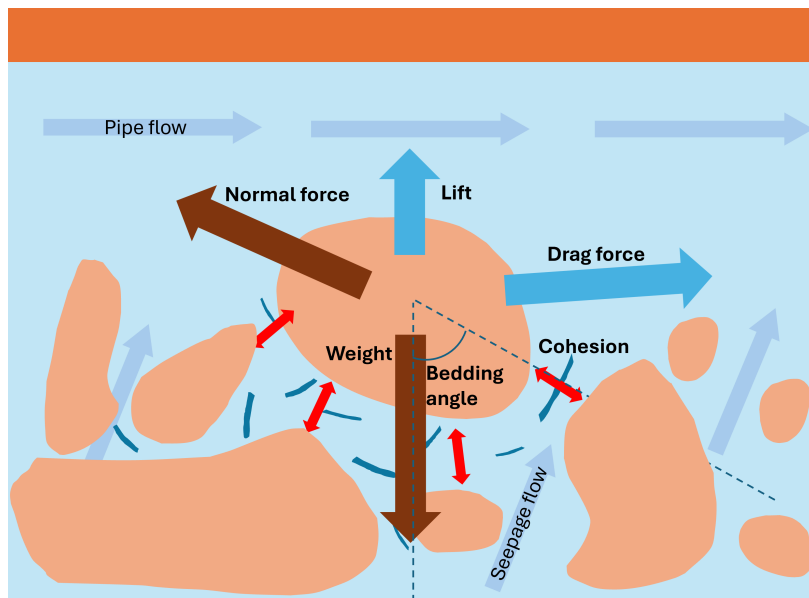


Figure 3.1: Forces acting on sediment particle with the presence of clay and fines

Cohesion

Cohesion of soils is the inter-particle force acting between two adjacent soil particles (Yokoi, 1968). Cohesion of soils can be caused by the affinity of clay particles for water (physical cohesion) and biological cementation (biological cohesion). Physical cohesion is dominated by electrostatic attraction and capillary adhesion. Electrostatic attraction is caused by the presence of positively charged cations between the water molecules present at the interface of two clay particles as seen in Figure 3.2. Higher salinity causes more cations to be present, resulting in higher cohesive forces. Biological cohesion is related to chlorophyll-a content, organic content and EPS content (Methorst, 2020). An exact relation between the biological contents, clay content and the quantitative cohesion force is not available.

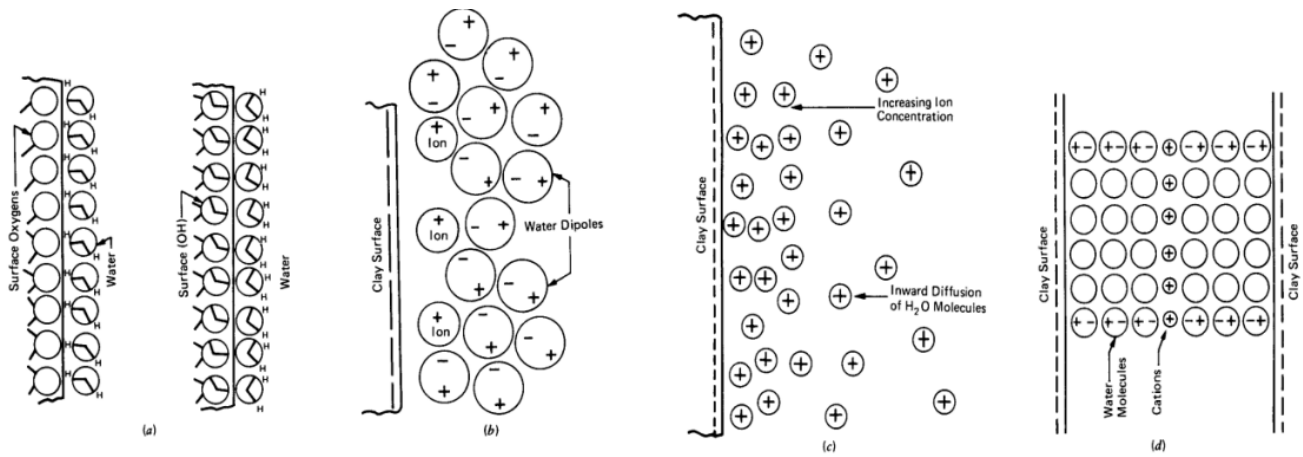


Figure 3.2: Mechanism of electrostatic cohesion (Mitchell and Soga, 2005)

Embedding in fine soil matrix

The addition of fines increases the internal stability of a soil. This is partly due to clay coat coverage of soil grains (Wooldridge et al., 2018). Better graded soils have higher internal stability and due to the presence of fines, soils are better graded (Chang and Zhang, 2013). The grading of a soil is measured by the coefficient of uniformity (C_u) as seen in Eq. 3.1. A soil with a higher coefficient of uniformity is better graded than a soil with a lower coefficient of uniformity.

$$C_u = \frac{D_{60}}{D_{10}} \quad (3.1)$$

In which:

D_{60} : Sieve size which will pass 60% of the sand by weight [m]

D_{10} : Sieve size which will pass 10% of the sand by weight [m]

C_u : Coefficient of uniformity [-]

Soils with a higher uniformity coefficient are better graded and can therefore be packed more dense. If more fines are present, the sieve size which will pass 10% of the sand by weight will decrease, therefore increasing the C_u . This is assumed to result in larger bedding angles, as shown in Figure 3.3.

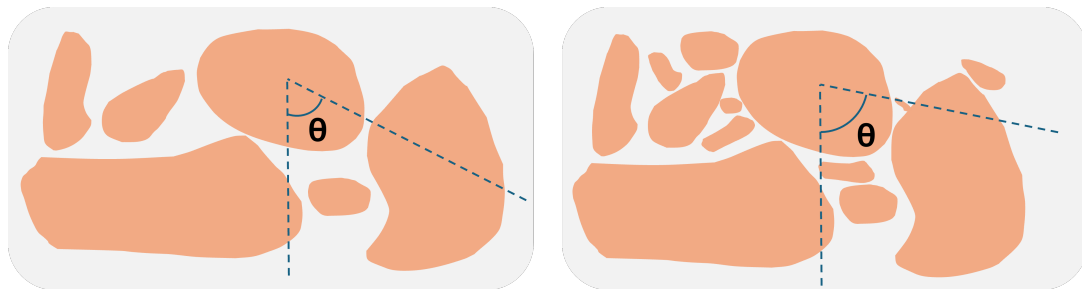


Figure 3.3: Influence of fine matrix on bedding angle (The right figure is more dense than the left figure due to the presence of fines)

Hydraulic conductivity

The presence of tidal deposits does not only influence the resistance of the particles against movement, but also influences the groundwater flow. The soil profile consists of thin clay and sand layers due to the tidal flow fluctuations. In the horizontal direction, the groundwater flow will concentrate in the sand layers and is able to find a path with low resistance. Therefore, the horizontal conductivity remains in the same order of magnitude as normal sand layers. The groundwater flow will however be slowed down in the vertical direction, caused by the horizontal clay layers or denser packed sand layers. This difference in vertical and horizontal hydraulic conductivity is referred to as multilayeredness and shown in Figure 3.4 (Van Asselen et al., 2019). Anisotropy in hydraulic conductivity occurs at a smaller scale than the global soil layers. A specific soil layer itself can be anisotropic due to the positioning of irregular shaped soil particles as seen in Figure 3.5.

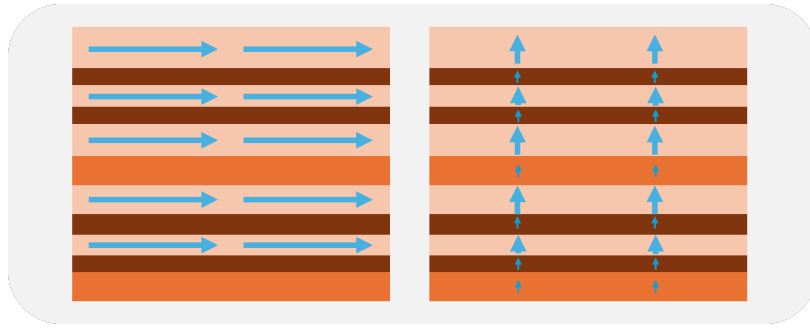


Figure 3.4: Effect of multilayered soil structure on directional hydraulic conductivity

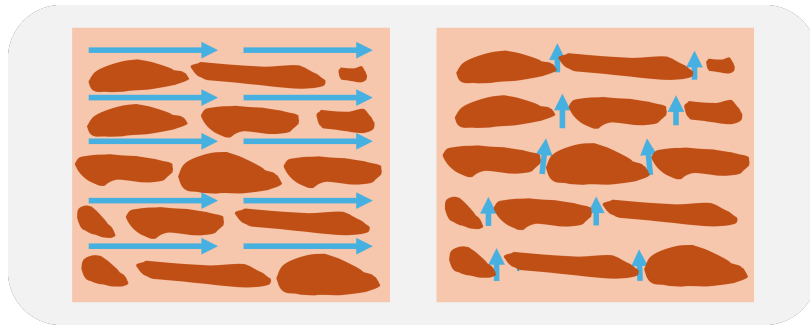
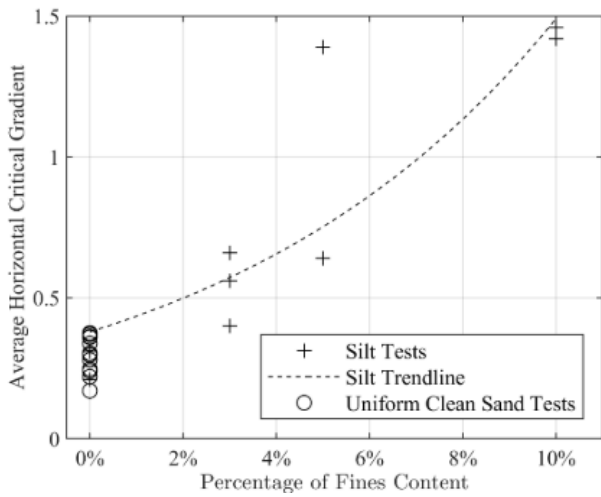


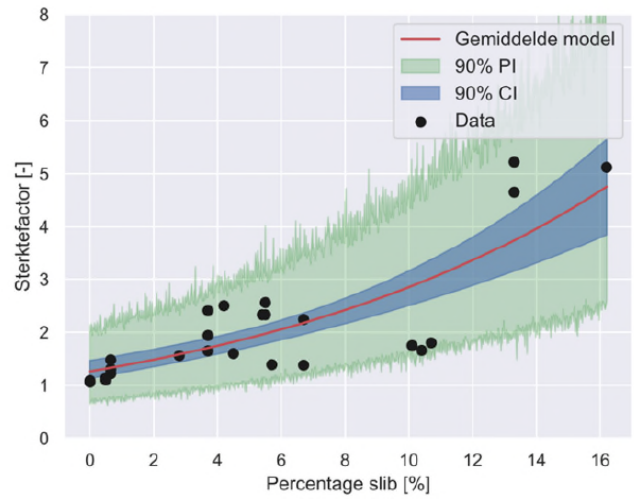
Figure 3.5: Effect of particle orientation on anisotropic hydraulic conductivity

3.1.2. Physical experiments results

In recent years, multiple physical experiments have been performed to gain knowledge on backward erosion piping in tidal sands. The hypothesis was that tidal sands result in added resistance due to cohesion and embedding in the fine soil matrix caused by the fines fraction. More added resistance is caused by the labyrinth structure of overlapping clay and sand lenses, formed by tidal layers, slowing down the pipe progression. A reduction in hydraulic forcing is also expected, due to lowered hydraulic conductivity caused by multilayeredness and anisotropy (Hijma, Van Goor, De Bart, et al., 2023). Both small and large scale experiments have been conducted by Deltares at the Vijfhuisterdijk and the Hedwigepolder in the Netherlands (Hijma et al., 2021; Hijma, Van Goor, De Bart, et al., 2023; Hijma, Van Goor, Pruijn, Van Beek, Wopereis, and Wiersma, 2023). These experiments were accompanied by multiple other theoretical studies on the influence of tidal deposits on BEP (Van Asselen et al., 2019; Methorst, 2020). A 15% increase in critical head per percent point mud ($d < 16 \mu\text{m}$) was found (Hijma et al., 2021). Small scale experiments also have been conducted in the USA (Lucker and Robbins, 2023). For the research by Luckner and Robbins, it is important to note that the critical gradients for different fines percentages were not corrected for the change in hydraulic conductivity (k) and particle diameter (d_{70}) due to the addition of these fines. The critical head gradients do not only increase due to the physical behaviour of the fines, but also due to the changed hydraulic conductivity and particle diameter.



(a) Observed average horizontal critical gradients for different fines fractions ($d < 63 \mu m$) (Lucker and Robbins, 2023).



(b) Found strength factors for different mud ('slib') fractions ($d < 16 \mu m$) by Deltares (Hijma, Van Goor, De Bart, et al., 2023)

Figure 3.6: Earlier found influence of fines fraction on BEP resistance

The physical experiments of Deltares resulted in strength factors which relate the measured critical head to the expected critical head following from Sellmeijer 2011. A strength factor of 1.4 [-] was found as the 5% lower value of the experiments results.

Anisotropy is often present in tidal deposits and also influences the strength against backward erosion piping. Many small- and medium scale tests do however not include the influence of anisotropy, while large scale experiments do include these effects.

3.1.3. Tidal sands framework

The different tidal sand influences on BEP can be ordered in the framework shown in Figure 3.7. The presence of tidal sands influences the resistance against BEP, the differences in horizontal and vertical hydraulic conductivity influence the loading of BEP. The green boxes are related to the resistance against BEP. The grey boxes are related to the loading due to their effect on the groundwater flow. The grey boxes have already been implemented in numerical models, the green boxes now also will be taken into account by adapting the onset of motion criterion.

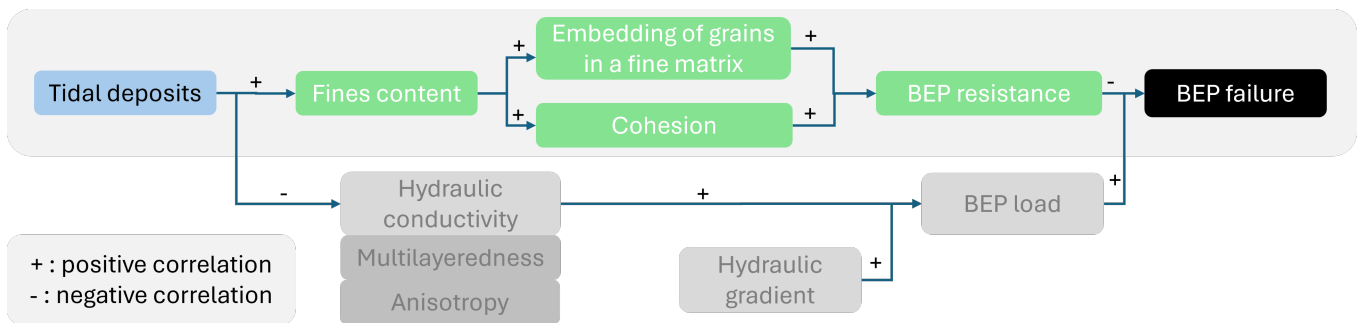


Figure 3.7: Conceptual framework of the physical BEP process, highlighting resistance-related factors (green) and loading-related factors (grey)

3.2. New Onset of Motion Criterion

3.2.1. Added parameters in Onset of Motion Criterion

The original onset of motion criterion proposed by White is given in Eq. 3.2 (White, 1940). This criterion will be made dependent on the silt- and clay fraction. The Mohr-Coulomb relationship is used as inspiration, with the added cohesion force in the determination of the soil shear strength as seen in Eq. 3.3. Mohr-Coulomb uses the internal friction angle (ϕ), which is not the same as the bedding angle (θ) from White.

$$\tau_c = \eta \frac{\pi}{6} \rho' g d_{70} \tan(\theta) \tag{3.2}$$

$$\tau_{Mohr-Coulomb} = \sigma \tan(\phi) + C \tag{3.3}$$

Where:

τ_c : Critical shear stress for movement of a single particle [Pa]

θ : Bedding angle [°]

$\tau_{Mohr-Coulomb}$: Critical shear stress for internal soil failure on a certain plane [Pa]

ϕ : Friction angle [°]

σ : Normal stress on the failure plane [Pa]

C : Cohesive force [Pa]

The onset of motion criterion of White relates the horizontal drag force, the weight and the normal force to find a force equilibrium, as seen in Figure 3.8a. Since the percentage of silt influences the bedding angle, this will be incorporated inside $\tan(\theta)$. Cohesion acts in both horizontal and vertical directions and depends on different contact areas for the horizontal and vertical direction, since cohesion only works as a tensile force. In vertical direction, the whole cohesive area as indicated in Figure 3.8b can act as a tensile force, while cohesion on the left half of the cohesive area cannot act as a tensile force against a displacement in the horizontal direction. The cohesion is dependent on the area of contact of the soil particle with the surrounding particles. The parameters α_x and α_y are the dimensionless fractions of the area (d_{70}^2) over which the cohesive force acts and are dependent on the clay fraction of the soil. For vertical cohesion, the area of a half sphere is not equal to d_{70}^2 but to $\frac{1}{2}\pi d_{70}^2$. In case of the horizontal cohesion, the area of a quarter sphere is equal to $\frac{1}{4}\pi d_{70}^2$. But since $\frac{1}{2}\pi$ and $\frac{1}{4}\pi$ are constant, these parts are assumed to be incorporated in α_y and α_x respectively.

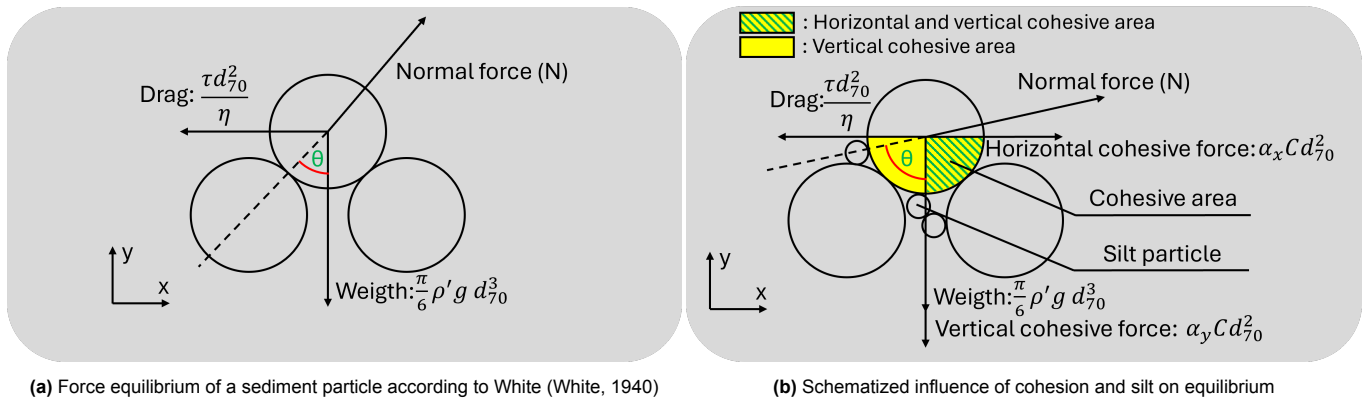


Figure 3.8: Equilibrium of forces on sediment particle; the pipe flow is directed in negative x-direction

The force equilibria, as shown in Figure 3.8, can be used to calculate the critical shear stress for the onset of motion criterion. First, the horizontal and vertical equilibrium of forces is determined in Eqs. 3.4 and 3.5. The normal force is then calculated in Eq. 3.6 by rewriting the vertical equilibrium of forces. By inserting Eq. 3.6 in Eq. 3.4, the balance of forces is found in Eq. 3.7. This leads to Eq. 3.8 to find the critical shear stress.

$$\sum F_x = N \cdot \sin(\theta) - \frac{\tau d_{70}^2}{\eta} = 0 \quad (3.4)$$

$$\sum F_y = N \cdot \cos(\theta) - \frac{\pi}{6} \rho' g d_{70}^3 = 0 \quad (3.5)$$

$$N = \frac{\frac{\pi}{6} \rho' g d_{70}^3}{\cos(\theta)} \quad (3.6)$$

$$\frac{\frac{\pi}{6} \rho' g d_{70}^3}{\cos(\theta)} \cdot \sin(\theta) - \frac{\tau d_{70}^2}{\eta} = 0 \quad (3.7)$$

$$\tau = \eta \frac{\pi}{6} \rho' g d_{70} \tan(\theta) \quad (3.8)$$

The same calculations are made with the included influence of cohesion. First, the cohesion is included in both horizontal and vertical direction. The new horizontal and vertical force equilibria are found in Eqs. 3.9 and 3.10. This results in the new normal force as seen in Eq. 3.11. By inserting the normal force in the horizontal equilibrium of Eq. 3.9, the new balance of forces is found in Eq. 3.12. The influence of d_{70}^2 on the cohesion force is algebraically cancelled out by the d_{70}^2 term in the drag force expression acting on the particle. This leads to Eq. 3.13 to find the influence of cohesion on the onset of motion criterion.

$$\sum F_x = N \cdot \sin(\theta) - \frac{\tau d_{70}^2}{\eta} + \alpha_x C d_{70}^2 = 0 \quad (3.9)$$

$$\sum F_y = N \cdot \cos(\theta) - \frac{\pi}{6} \rho' g d_{70}^3 - \alpha_y C d_{70}^2 = 0 \quad (3.10)$$

$$N = \frac{\frac{\pi}{6} \rho' g d_{70}^3 + \alpha_y C d_{70}^2}{\cos(\theta)} \quad (3.11)$$

$$\frac{\frac{\pi}{6} \rho' g d_{70}^3 + \alpha_y C d_{70}^2}{\cos(\theta)} \cdot \sin(\theta) - \frac{\tau d_{70}^2}{\eta} + \alpha_x C d_{70}^2 = 0 \quad (3.12)$$

$$\tau = \eta \left(\frac{\pi}{6} \rho' g d_{70} + \alpha_y C \right) \tan(\theta) + \alpha_x C \quad (3.13)$$

The vertical influence of cohesion ($\alpha_y C$) is found to be included in the term including $\tan(\theta)$ due to its influence on the vertical force equilibrium. The horizontal influence of cohesion ($\alpha_x C$) became a separate term. The vertical cohesion term only acts against a positive vertical motion of the particle. This vertical motion can be caused by lift and the vertical seepage gradient, these forces are relatively small compared to the drag force, particle weight and normal force. Lift force and seepage gradient are currently not included in the two forces model of Sellmeijer (Sellmeijer et al., 2011). Therefore the term $\alpha_y C$ is excluded from the final onset of motion criterion. The horizontal cohesion force acts when the particle will move horizontally, this is mainly caused by the drag force due to the pipe flow on the particle and will be a significant force. Finally, the influence of silt is included by multiplying the bedding angle θ with a term to be fitted based on the silt fraction. If no silt fraction is present, the term inside the tangent should retain its original value of 37° . This results in Eq. 3.14.

$$\tau_c = \eta \frac{\pi}{6} \rho' g d_{70} \tan(\theta \cdot (1 + silt)) + \alpha_x C \quad (3.14)$$

The term in the equation which includes the cohesion is defined as $\alpha_x C$. In this term, α_x describes the fraction of the area of the particle on which the cohesion force is present. The parameter C represents the cohesive strength, i.e., the tensile stress due to cohesion [Pa]. It is assumed that these parameters are only dependent on the clay fraction in the soil. These parameters will be empirically determined by fitting the model to experimental data obtained from Deltares. The influence of silt will also be fitted to this data and this parameter is assumed to only be dependent on the silt fraction. An exponential fit is applied to model the influence of silt and clay, resulting in the onset of motion criterion as shown in Eq. 3.15.

$$\tau_c = \eta \frac{\pi}{6} \rho' g d_{70} \tan(\theta \cdot (1 + a \cdot \%_{silt}^b)) + (c \cdot \%_{clay}^d) \quad (3.15)$$

Where:

τ_c : Critical shear stress [Pa]

η : White's coefficient [-]. $\eta = 0.25$

ρ' : Density difference between solid and fluid [kg/m^3]

g : Acceleration of gravity [m/s^2]

θ : Bedding angle [$^\circ$]. $\theta = 37^\circ$

d_{70} : Characteristic particle diameter [m]

$\%_{silt}$: Percentage of grain size distribution by weight between $2 \mu\text{m}$ and $63 \mu\text{m}$ [%]

$\%_{clay}$: Percentage of grain size distribution by weight below $2 \mu\text{m}$ [%]

a, b, c, d : Empirical coefficients of silt and clay influence [-]

The new onset of motion criterion will be fitted using the `curve_fit` function from the `scipy.optimize` package to incorporate the added resistance by fines due to cohesion and embedding in a fine soil matrix. The package `curve_fit` uses non-linear least squares to fit parameters in a function to the input data. The Python code used for parameter fitting is provided in Appendix A. An equation in the form of Mohr-Coulomb is used for the new onset of motion criterion, since this clearly distinguishes the influence of cohesion and the bedding angle.

3.2.2. Fitting the Onset of Motion Criterion

BEP experiments have resulted in data linking the clay fraction and silt fraction to the observed hydraulic head via a strength factor (sf). The observed hydraulic head from the experiments divided by the expected hydraulic head according to Sellmeijer's 2011 rule resulted in this strength factor as seen in Eq. 3.16. Assuming that the silt and clay fraction only influence the resistance factor (Eq. 3.17) in Sellmeijer's 2011 rule, a new F_R can be calculated to make Sellmeijer 2011 dependent on the silt and clay fraction as seen in Eq. 3.18.

$$sf = \frac{H_{c,experiments}}{H_{c,Sellmeijer\ 2011}} \quad (3.16)$$

$$F_{R,original} = \eta \frac{\gamma'_p}{\gamma_w} \tan(\theta) \quad (3.17)$$

$$F_{R,new} = \eta \frac{\gamma'_p}{\gamma_w} \tan(\theta \cdot (1 + a \cdot \%_{silt}^b)) + (c \cdot \%_{clay}^d) \quad (3.18)$$

Where:

sf : strength factor [-]

$H_{c,experiments}$: Critical hydraulic head as observed in experiments [m]

$H_{c,Sellmeijer\ 2011}$: Critical hydraulic head as predicted with Sellmeijer 2011 [m]

The new F_R should be equal to the observed strength factor multiplied with the original F_R . To find a safe lower boundary of the fit, 95% of the observed $sf \cdot F_{R,original}$ values should be higher or equal than the predicted $F_{R,new}$. Using *curve_fit* in Python the coefficients can be fitted on Eq. 3.19.

$$np.percentile(F_{R,new} - sf \cdot F_{R,original}, 95) = 0 \quad (3.19)$$

All results of earlier experiments are collected in a dataset. Results of small scale, medium scale and large scale experiments are used. A randomly selected subset of the experiments is used in the training group (Table 3.1). The other experiments are set apart to function as a validation group for the fitted onset of motion criterion (Table 3.2).

Table 3.1: Soil Parameters for Training Group Experiments

Experiment Name	Silt (%)	Clay (%)	d70 (mm)	sf (-)
B146	0.0	0.0	0.150	1.00
MSP43_HWP3	6.6	2.3	0.148	1.30
HWP_264	17.9	7.5	0.131	5.20
GTZG_1_207	2.7	2.2	0.160	2.40
GTFZ_3_214	18.0	1.0	0.130	2.30
HWP_269	8.3	4.6	0.140	1.50
GTFZ_251	11.9	2.7	0.118	2.30
HWP_265	17.9	7.5	0.131	4.70
HWP_263	14.4	2.7	0.122	1.40
B15_3K	0.6	2.4	0.171	3.30
GTZG_2_208	2.7	2.2	0.160	1.90
GTZG_3_209	2.7	2.2	0.160	1.70
hedwige noord	10.7	4.1	0.138	1.40
GTFZ_2_214	18.0	1.0	0.130	2.60
B15_1K	0.2	0.8	0.171	1.30
hedwige zuid	10.7	4.1	0.138	1.40
HWP_271	7.9	3.6	0.139	4.10
Bms19	0.0	0.0	0.150	1.06
HWP_273	10.8	4.9	0.149	1.30
HWP_253	6.3	4.5	0.138	1.40
HWP_260	11.7	1.4	0.127	2.20
HWP_267	13.1	6.9	0.122	1.80
HWP_272	12.8	6.7	0.118	1.80
GTFZ_252	12.6	2.1	0.123	6.10

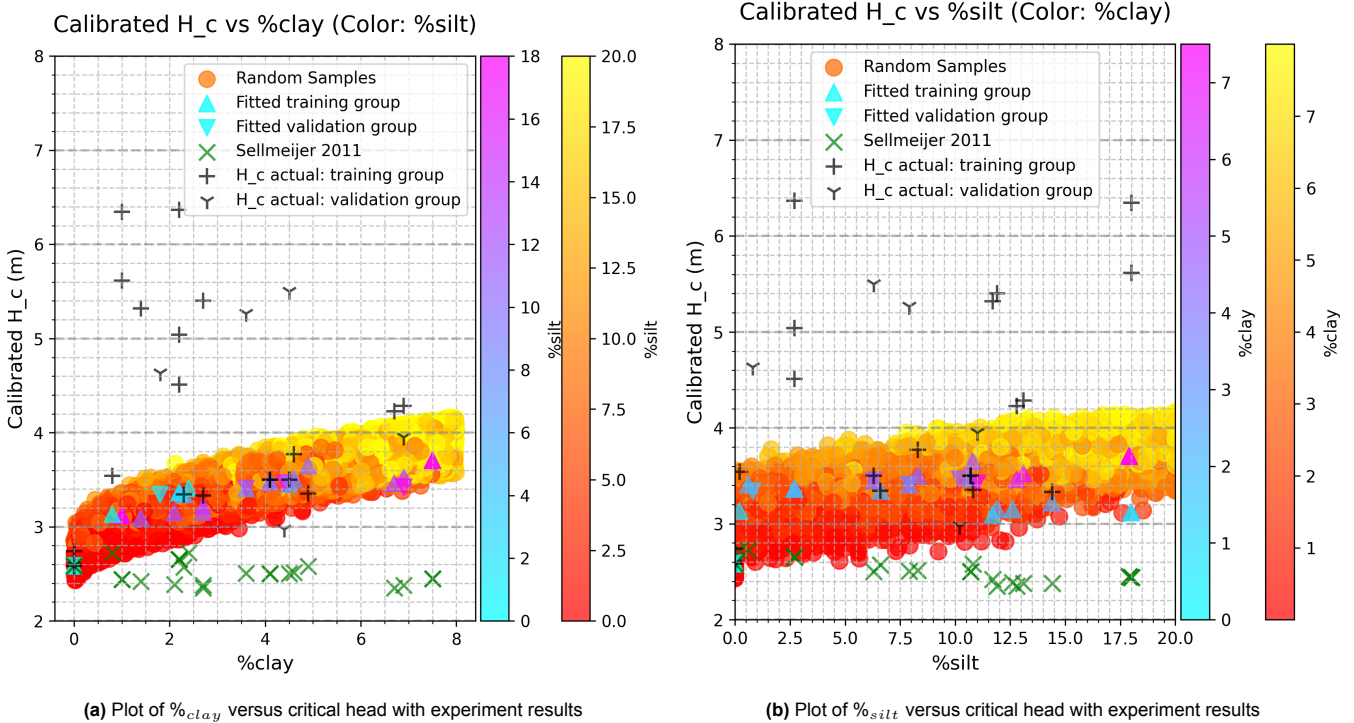
Table 3.2: Soil Parameters for Validation Group Experiments

Experiment Name	Silt (%)	Clay (%)	d70 (mm)	sf (-)
B145	0.0	0.0	0.150	1.00
HWP_268	11.0	6.9	0.115	1.70
MSP42_HWP2	10.2	4.4	0.135	1.20
HWP_270	7.9	3.6	0.139	2.10
HWP_254	6.3	4.5	0.138	2.20
HWP_256	0.8	1.8	0.171	1.70

Both linear and exponential relations between the clay fraction, silt fraction and strength factor have been evaluated to search for a fit. The most physically realistic fits should have a strength factor of 1 for a silt and clay fraction of zero. Also both the clay and silt fraction have a positive effect on the resistance against backward erosion piping, therefore the strength factor should increase with higher values of clay and silt. As silt only influences the bedding angle and clay causes cohesion, the relationship from Eq. 3.15 is assumed. Fitting this relationship results in Eq. 3.20.

$$\tau_c = \eta \frac{\pi}{6} \rho' g d_{70} \tan(\theta \cdot (1 + 0.023 \cdot \%_{silt}^{0.47})) + (0.047 \cdot \%_{clay}^{0.47}) \quad (3.20)$$

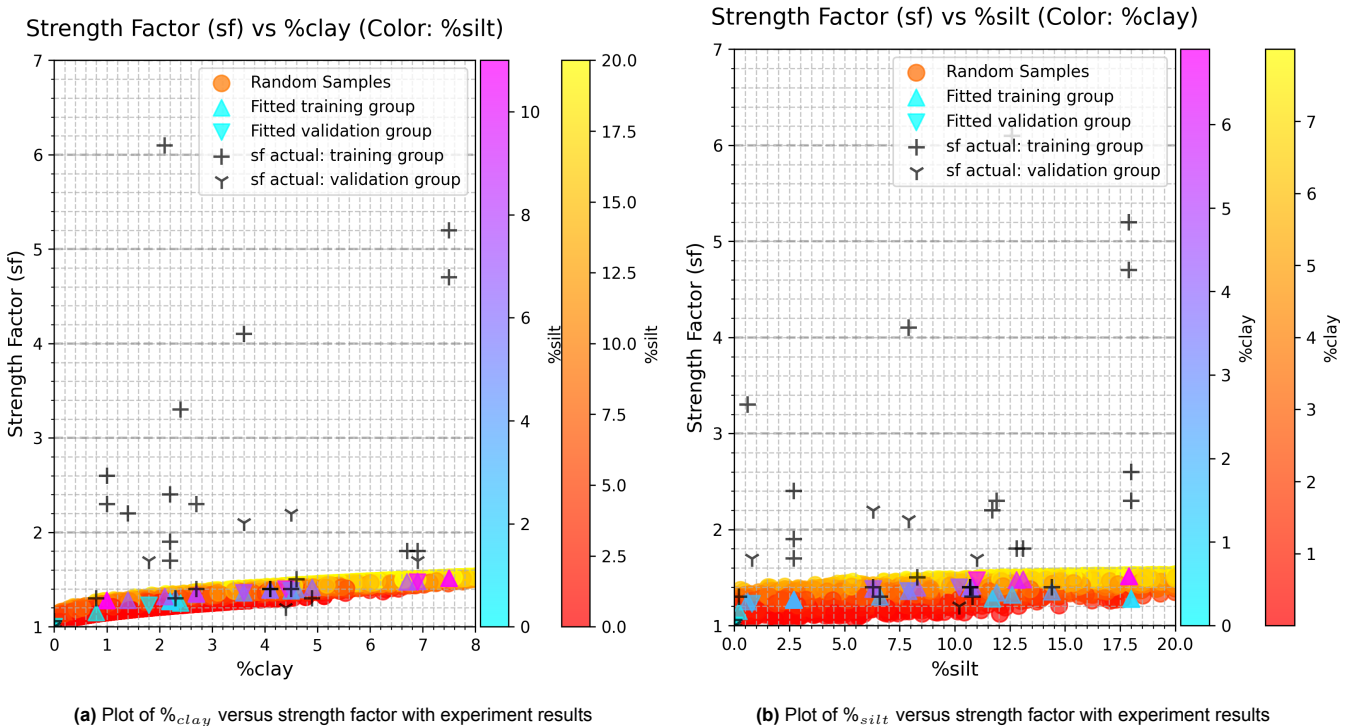
The safety values as predicted by the new onset of motion criterion are plotted as blue/purple triangles in Figure 3.10a and 3.10b. The triangles pointing upward are training data, the triangles pointing downward are validation data. The actual results from the physical experiments are plotted as black '+' signs for the training data, the black 'Y' signs are the actual results from the validation data. Random samples of possible combinations of clay- and silt fractions are plotted with the yellow-orange dots. This shows that for samples with the same clay fraction but with a different silt fraction, the sample with the higher silt fraction gives more strength. It can be observed that the fit follows the lower 5% experimental results. Some experimental results yielded strength factors exceeding 6, indicating substantial resistance in certain soil compositions.



(a) Plot of % $_{clay}$ versus critical head with experiment results

(b) Plot of % $_{silt}$ versus critical head with experiment results

Figure 3.9: Plots of critical head with experimental- and predicted results (fitted to the lowest 5% of observed H_c values)



(a) Plot of % $_{clay}$ versus strength factor with experiment results

(b) Plot of % $_{silt}$ versus strength factor with experiment results

Figure 3.10: Plots of strength factor with experimental- and predicted results (fitted to the lowest 5% of observed H_c values)

The relationships between %clay, %silt and the strength factor are plotted in Figure 3.11a and 3.11b. Both relationships show a square root function due to the fitted powers in the critical shear stress equation. The critical shear

stress is found to be more sensitive to the presence of clay than to the presence of silt.

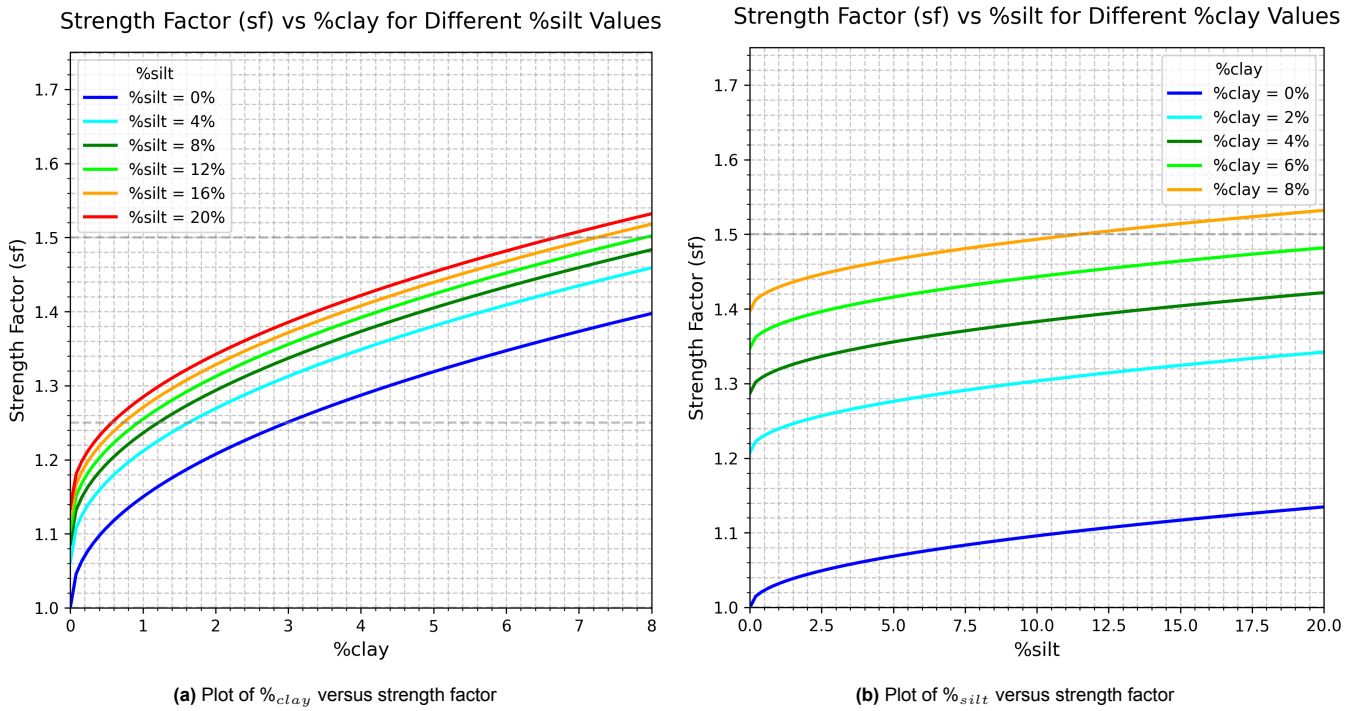


Figure 3.11: Plots of the influence on silt- and clay fractions on the strength factor (fitted to the lowest 5% of observed H_c values)

Additionally, a non-conservative fit which is fitted by using the 50-percentile in Eq. 3.19 and a fit using mud and fines fractions were created. These show a non-conservative fit and a fit with almost no indication for extra safety, respectively. The current fit on clay and silt on the 95-percentile of Eq. 3.19 gives possibilities for finding extra strength, while also giving safe values. The other fits are found in Appendix B.

This chapter describes the method used to develop the numerical backward erosion piping model. The implementation of groundwater flow, pipe flow and erosion process in the model are explained. The implementation of the erosion is adapted based on the results of Chapter 3. The method focuses on the development of a 2D, stepwise steady-state backward erosion piping model. Also, the variables and events as needed in the final model are described in this chapter.

4.1. Model physics

4.1.1. Groundwater flow

Groundwater flow (Figure 4.1) is typically modelled using a combination of Darcy's law (Eq. 4.1) and the conservation of mass (Eq. 4.2). Groundwater flow is dependent on the hydraulic conductivity and on the hydraulic head over a certain aquifer length. Hydraulic conductivity can be rewritten to the permeability by using the gravitational acceleration, fluid viscosity and fluid density as shown in Eq. 4.3.

$$q = -k\nabla h \quad (4.1)$$

$$S_s \frac{\delta h}{\delta t} = -\nabla q \quad (4.2)$$

$$\kappa = \frac{k\rho g}{\mu} \quad (4.3)$$

In which:

k : Hydraulic conductivity [m/s]

κ : Hydraulic permeability [m²]

q : Specific discharge [m/s]

h : Total head [m]. $h = \frac{p}{\rho_w g} + z$

p : Pressure [Pa]

ρ_w : Density of water [kg/m³]

g : Acceleration of gravity [m/s²]

S_s : Specific storage [m⁻¹]

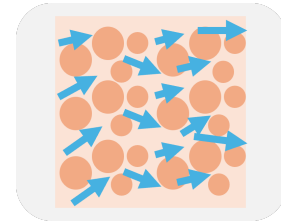


Figure 4.1: Groundwater flow

4.1.2. Pipe flow

A laminar flow regime is generally assumed in the pipe due to the small dimensions of the pipe. This corresponds with low Reynolds numbers, as shown in Eq. 4.4. Pipes in experimental setups are typically shallow, with depths observed in small scale experiments ranging from 1-10 times the sediment particle diameter (Van Beek, 2015; Van denboer, 2019). In large scale experiments, the pipe depth can become larger than 100 times the particle diameter (Hijma, Van Goor, De Bart, et al., 2023). This phenomenon is still under investigation, it could be caused by the type of pipe roof. In real situations the roof consist of clay, in experimental setups an acrylic or glass roof is used. This could influence the pipe in taking different shapes.

$$Re = \frac{\rho V D_h}{\mu} \quad (4.4)$$

In which:

Re : Reynolds number [-]

V : Fluid velocity [m/s]

D_h : Hydraulic diameter of pipe [m]

μ : Dynamic viscosity [Pa · s]

A continuum method (Navier-Stokes) or the Lattice-Boltzman method can also be used to model pipe flow. These methods are however computationally expensive and therefore more often linear methods are used. The flow in the pipe can be modelled with the linear equations of Darcy-Weisbach or Hagen-Poiseuille.

A fictitious permeability of the pipe (Eq. 4.5) can be assumed to apply Darcy's law on the pipe flow (Bersan et al., 2013; Aguilar-López et al., 2016). This permeability is dependent on the pipe shape and size. This method is less computationally expensive than a continuum method.

$$\kappa^* = \frac{2D_h^2}{\beta_{fi}} \quad (4.5)$$

In which:

κ^* : Fictitious permeability [m²]

β_{fi} : Friction coefficient of the pipe cross-section [-]

The value of D_h and β_{fi} depend on the size and shape of the pipe respectively. Often the pipe is assumed to be infinitely wide and shallow as a simplification, giving $\frac{w}{a} \approx \infty$. In which w is the pipe width and a is the pipe depth. In this case D_h is equal to $2a$ and β_{fi} is 96 [-] (Aguilar-López et al., 2016). Aguilar also gives values of these parameters for other pipe shapes. A schematization of pipe flow is shown in Figure 4.2.

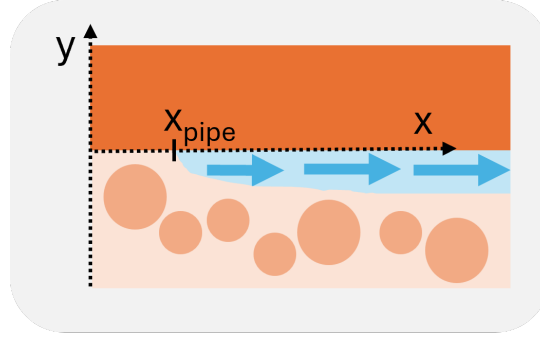


Figure 4.2: Schematic representation of pipe flow

4.1.3. Erosion

The erosion process in backward erosion piping can be split up in primary and secondary erosion (Hanses, 1985). Numerical models can take into account only primary erosion, only secondary erosion or both primary and secondary erosion. Secondary erosion is caused by large shear stresses acting on the walls and bottom of the pipe. If this exceeds a certain critical shear stress, erosion will occur. Erosion is implemented as a binary threshold: if the actual shear stress exceeds the critical value, erosion occurs, regardless of the magnitude of the excess.

The critical wall shear stress as used by Sellmeijer (Sellmeijer, 1988) is based on White's criterion (White, 1940) as displayed in Eq. 4.6. This critical stress is compared to the calculated shear stress on particles in the pipe as shown in Eq. 4.7 to determine if erosion occurs.

$$\tau_c = \eta \frac{\pi}{6} (\rho_s - \rho_w) g d \tan(\theta) \quad (4.6)$$

$$\tau = \frac{D_h}{4} \rho_w g i_{pipe} \quad (4.7)$$

In which:

τ_c : Critical shear stress [Pa]

τ : Shear stress at pipe wall [Pa]

η : White's coefficient [-]

ρ_s : Density of soil particle [kg/m³]

θ : Bedding angle [°]

d : Particle diameter [m]

i_{pipe} : Hydraulic gradient in pipe [-]

To implement the influence of tidal deposits, the new onset of motion criterion from Chapter 3 is used. Also a factor of 0.89 and $\left(\frac{d_{70,\mu}}{d_{70}}\right)^{0.6}$ are added to the onset of motion criterion to correct for larger and smaller particle sizes (Van Beek et al., 2022). This is applied both during validation and in the final model implementation.

$$\tau_{c,new} = 0.89 \eta \frac{\pi}{6} \rho' g d_{70} \tan(\theta \cdot (1 + 0.023 \cdot \%_{silt}^{0.47})) \left(\frac{d_{70,\mu}}{d_{70}}\right)^{0.6} + (0.047 \cdot \%_{clay}^{0.47}) \quad (4.8)$$

In which:

$\%_{clay}$: Percentage of grain size distribution by weight below 2 μm [%]

$\%_{silt}$: Percentage of grain size distribution by weight between 2 μm and 63 μm [%]

$d_{70,\mu}$: Mean value of d_{70} following considered experiments for calibration [m] ($d_{70,\mu} = 0.208 \text{ mm}$)

If the actual wall shear stress exceeds the critical shear stress, the pipe depth is incremented by $0.5 \cdot d_{70}$ in the numerical model, this can be adjusted to larger or smaller values depending on the desired resolution and computational efficiency. Larger growth steps could lead to errors, smaller steps are more computationally expensive. The erosion can be determined locally with the local hydraulic gradient or over the whole pipe with a global hydraulic gradient. The length of the pipe can be related to the pipe depth using Eq. 4.9 and 4.10 (Wewer et al., 2021).

$$a_{av}(l) = n_{particles} \cdot d_{70} \sqrt{\frac{l}{l_{max}}} \quad (4.9)$$

$$l = \frac{a_{av}^2 \cdot l_{max}}{n_{particles}^2 \cdot d_{70}^2} \quad (4.10)$$

In which:

$n_{particles}$: Maximum depth of pipe in number of d_{70} sized particles [#]; $n_{particles} = 10$, in medium scale tests

a_{av} : Average pipe depth over the pipe length [m]

l : Pipe length [m]

l_{max} : Maximum pipe length (dike base length) [m]

The pipe profile does not follow a rectangular shape over its length, but will be more shallow near the pipe tip. The shape of a leftward, upstream propagating pipe can be assumed to follow Eq. 4.11 (Pol, 2022). This equation is calibrated by experiments but was not yet implemented in numerical models. A value of $n_{particles}$ to fit in Eq. 4.9 can be found by rewriting Eq. 4.11 to Eq. 4.12.

$$a(x) = -6 \cdot \sqrt[3]{\kappa_{aquifer} \cdot (x - x_{tip})} \quad (4.11)$$

$$n_{particles} = \frac{6 \cdot \sqrt[3]{\kappa_{aquifer} \cdot l_{max}}}{d_{70}} \quad (4.12)$$

In which:

a : Local pipe depth [m]

x_{tip} : x-coordinate of pipe tip [m]

$\kappa_{aquifer}$: Hydraulic permeability of aquifer [m^2]

The full erosion process can be schematized as shown in Figure 4.3. When a time-dependent numerical model is constructed, transport equations for the sediment transport in the pipe have to be selected. Since the aim of the thesis is to use a 2D, stepwise steady-state model, no transport equations are needed.

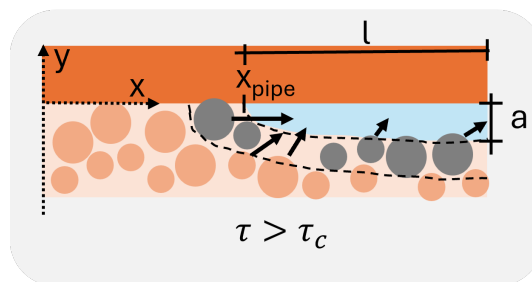


Figure 4.3: Pipe growth due to erosion

4.1.4. Boundary conditions

The model applies only no-flow (Neumann) and constant head (Dirichlet) boundary conditions. The no-flow boundaries are applied at the top of the pipe, functioning as an impermeable clay layer. The constant head boundaries represent the water levels at the sea side and polder side of the dike. These constant head boundaries will be applied on possible schematized foreshores, the aquifer (if acting as groundwater entrance location) and the exit point.

4.1.5. Mesh

A mesh is created over the whole geometry. A relatively wide mesh, compared to the actual pipe depth, is built for the pipe to make the model computationally less expensive. A correction for the actual pipe depth has to be made via the fictitious permeability in the pipe. This is done using Eq. 4.13. Now a mesh size of multiple centimetres can be chosen, while the actual pipe size can stay in the order of 1 mm. No quantitative sensitivity analysis is executed for the mesh size.

$$\kappa_{eq} = \kappa^* \cdot \frac{a_{pipe}}{a_{mesh}} \tag{4.13}$$

In which:

- κ_{eq} : Hydraulic permeability applied on pipe domain [m²]
- κ^* : Fictitious hydraulic permeability [m²]
- a_{pipe} : Depth of actual pipe [m]
- a_{mesh} : Depth of pipe domain in model [m]

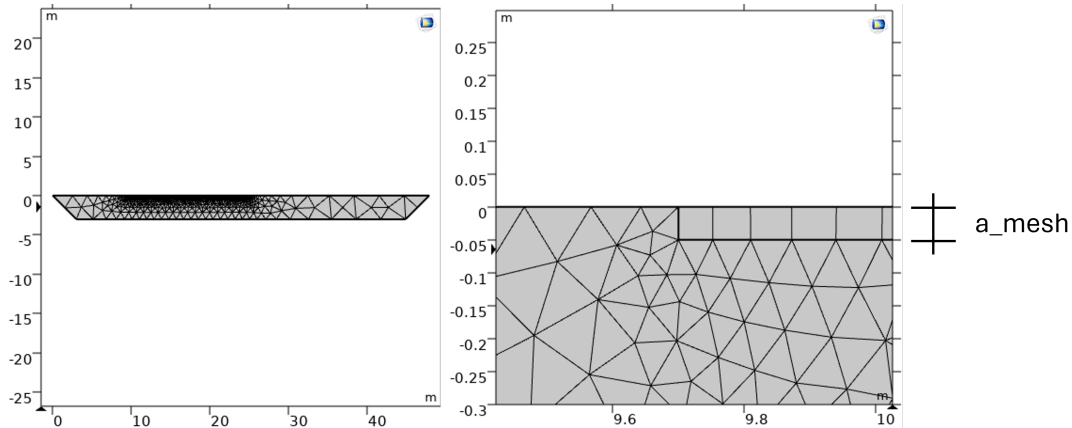


Figure 4.4: Computational mesh in COMSOL

4.2. Model variables

Several variables are defined and re-evaluated at each time step in the model. All variables are shown in Table 4.1. The model (re-)evaluates all these variables for each time step.

Variables for pipe shape

The variable 'a_depth' is extracted from an event as described in Section 4.3. This average pipe depth is needed to evaluate the average hydraulic diameter 'D_h'. The variable 'D_h_loc' is a locally evaluated hydraulic diameter, dependent on 'depth'. The variable 'depth' follows the pipe shape 'depth_profile', as defined in Chapter 4. The variable 'int_depth' is the average depth of the depth according to 'depth_profile', this average depth must match the average depth 'a_depth' as determined by the depth update event. Therefore, the variable 'depth' is calculated by scaling 'depth_profile' with 'a_depth' divided by 'int_depth'. When the pipe depth is updated, the pipe length is also updated, this influences the variable 'pipe_tip', which gives the location of the tip of the pipe (Shown as x_{pipe} in Figure 4.3). The flowchart for the variables determining the pipe shape is shown in Figure 4.5.

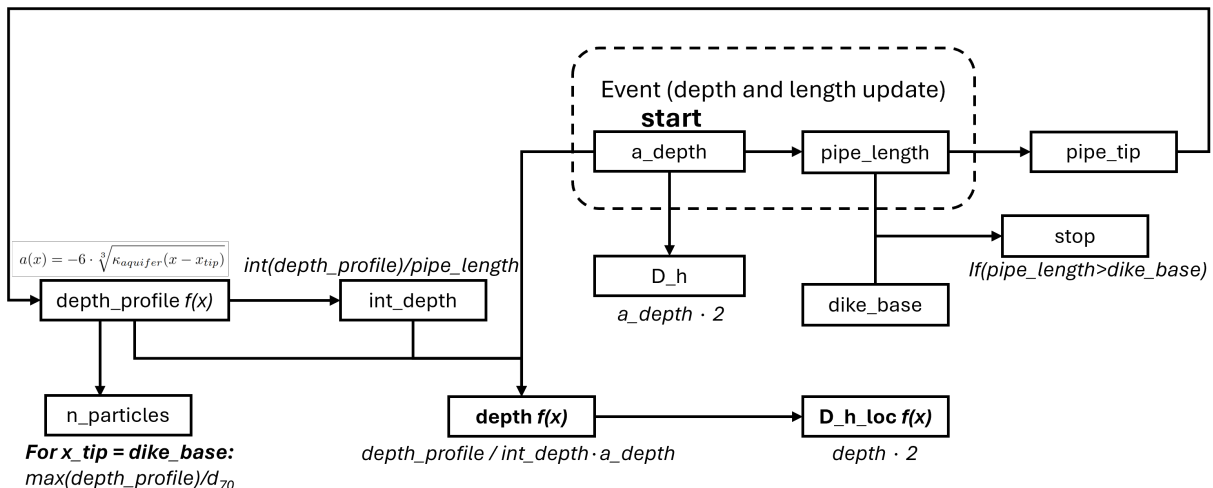


Figure 4.5: Flowchart for pipe shape

Variables for groundwater and pipe flow

All 'kappa_**' values evaluate a hydraulic permeability. The permeability 'kappa_aq' is the hydraulic permeability of the aquifer, 'kappa_loc' is the fictitious permeability for the pipe with the updated pipe depth. The variable 'kappa_pipe' is the permeability applied on the pipe domain, selecting the fictitious permeability for the eroded part of the pipe and the aquifer permeability for the non eroded part. The eroded part is located in the pipe domain where $x = x_pos$, in which the x-coordinates inside the pipe are defined as 'x_pos'. The porosity of the soil is selected to be 0.4 [-], the porosity inside the pipe is 1 [-]. 'Re_pipe' evaluates the flow regime in the pipe to check if the pipe flow is actually laminar. The flowchart for the variables determining the permeability is shown in Figure 4.6.

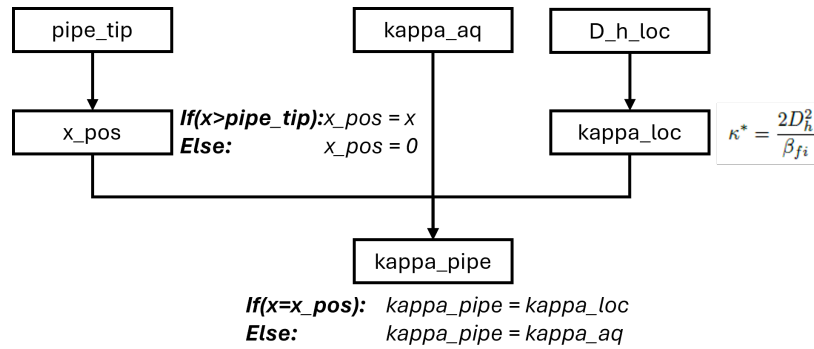


Figure 4.6: Flowchart for permeability

Variables for erosion

To check for erosion, the maximum shear stress inside the pipe has to be determined. The variable 'i_D_h' evaluates the maximum value of the hydraulic gradient times the hydraulic diameter over the pipe domain. The hydraulic gradient and the hydraulic diameter are the only variables with varying values over the pipe domain which influence the maximum shear stress on the sediment particles and therefore need to be evaluated over the whole pipe length to find a maximum shear stress. The hydraulic gradient 'i' is evaluated with '-d(dl.H,x)' over the pipe domain. The variable 'tau_max' evaluates the maximum shear stress over the whole pipe, the location of the maximum shear stress is defined in the variable 'where'. The variable 'tau_crit' is the critical shear stress, defined by the new onset of motion criterion. The variables 'F_g', 'F_r' and 'F_s' calculate the Sellmeijer 2011 factors, so also a strength factor can be calculated by dividing the found H_c with COMSOL by the H_c found with Sellmeijer. The flowchart for the variables determining the erosion is shown in Figure 4.7.

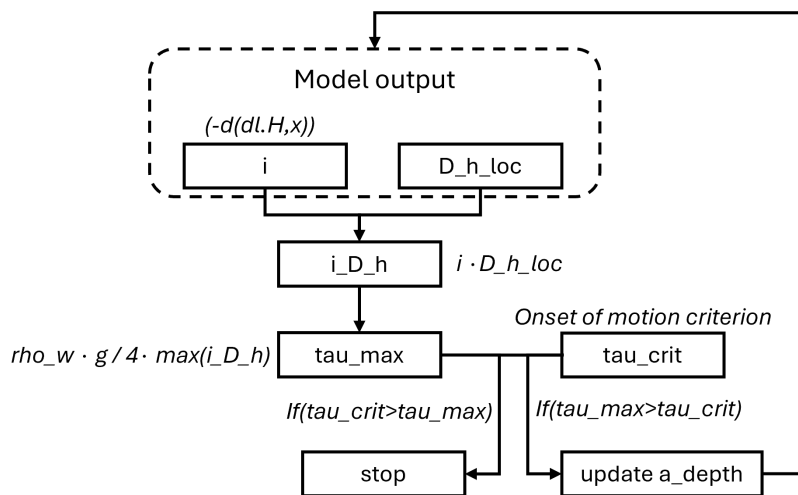


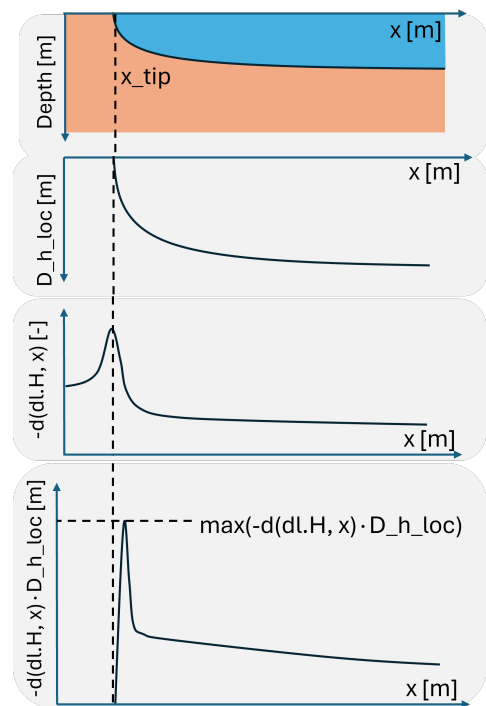
Figure 4.7: Flowchart for erosion

Table 4.1: Model variables

Variable	Expression	Unit
pipe_tip	dike_base+start_dike-length	m
a_depth	pipe_depth [m]	m
D_h	2*a_depth	m
D_h_loc	2*depth	m
depth_profile	6*(kappa_aq*x_pos)^(1/3)	m
int_depth	int_pipe(depth_profile*(x>pipe_tip))/(int_pipe(x>pipe_tip))	m
kappa_aq	(k_sand*dyn_visc)/(rho_w*g)	m ²
kappa_loc	(2*D_h_loc^2)/beta_fi	m ²
kappa_pipe	if(x>pipe_tip ,kappa_loc*depth/(a), kappa_aq)	m ²
x_pos	if(x>pipe_tip, x-pipe_tip, 0)	m
depth	depth_profile/int_depth*a_depth	m
av_u	int_pipe(dl.u*(x>pipe_tip))/(int_pipe(x>pipe_tip))	m/s
Re_pipe	rho_w*av_u*D_h/dyn_visc	-
poros	if(x>pipe_tip , 1, 0.4)	-
av_depth	int_pipe(depth*(x>pipe_tip))/(int_pipe(x>pipe_tip))	m
F_g	0.91*(d_aquifer/dike_base)^(0.28/((d_aquifer/dike_base)^2.8-1)+0.04)	-
F_r	white*(rho_s-rho_w)/rho_w*tan(theta)	-
F_s	d70/((kappa_aq*dike_base)^(1/3))*(d70m/d70)^0.6	-
H_c_sell	F_g*F_r*F_s*dike_base	m
tau_crit	0.89*white*pi/6*(rho_s-rho_w)*g*d70*tan(theta*(1+0.023*per_silt^0.47))* (d70m/d70)^0.6+0.047*per_lutum^0.47	Pa
tau_max	rho_w*g*i_D_h/4	Pa
i_D_h	if(maxop1((-d(dl.H,x)-n_basic*i_basic)*(x==where))>0, maxop1(D_h_loc*n_basic* i_basic*(x==where)), maxop1(D_h_loc*d(dl.H,x)*(x==where)))	m
where	maxop1(D_h_loc*if(-d(dl.H,x)>n_basic*i_basic,n_basic*i_basic,-d(dl.H,x)) *(pipe_tip<x)*(x<(pipe_tip+length)),x)	m
i_where	maxop1(-d(dl.H,x)*(x==where))	-
dh_where	maxop1(D_h_loc*(x==where))	m
i_basic	H_left/dike_base	-
depth_max	6*(kappa_aq*dike_base)^(1/3)	m
n_particles	depth_max/d70	#

The maximum shear stress is found as shown in Figure 4.8. The shear stress is dependent on two variables which are dependent on x (their location in the pipe). The first variable is the hydraulic gradient, the second variable is the hydraulic diameter of the pipe. The hydraulic gradient peaks at the tip of the pipe, while the hydraulic diameter is zero at this location. The maximum shear stress is therefore found just after the pipe tip and can be found with Eq. 4.14.

$$\tau_{max} = \max(-d(dl.H, x) \cdot D_{h\ loc}) \cdot \frac{\rho g}{4} \quad (4.14)$$

Figure 4.8: Determination of τ_{max}

4.3. Pipe progression events

For each time step, a new pipe depth and pipe length is determined. The initial pipe length is $\frac{dike_base}{100}$ and the initial pipe depth is determined by substituting the initial pipe length in Eq. 4.9. The new depth and length are found as seen in Table 4.2. The pipe depth is updated by relating the maximum shear stress (Eq. 4.7) to the critical shear stress (Eq. 4.8). The pipe depth increases if the shear stress is found to be larger than the critical shear stress. If the shear stress is smaller than the critical shear stress, the pipe depth stays the same and no further erosion will occur. The length is dependent on the new pipe depth as shown in Eq. 4.10. The COMSOL model was run via the MPH package in Python. A Python script is used to run the model in a for-loop, varying the hydraulic head from low to higher values with steps of 0.1 m. A stop condition is activated when 'length' is larger than 'dike_base', this is the time step for which the pipe is fully progressed underneath the dike. When this condition is met, the critical head is exported to python and saved in an array, to be able to review the obtained values.

Table 4.2: Stepwise steady-state events

Variable	Expression	Unit
pipe_depth (local gradient)	if($\tau_{max} > \tau_{crit}$, pipe_depth+0.5*d70, pipe_depth)	m
length	$(pipe_depth^2 * dike_base) / (n_{particles}^2 * d70^2)$	m

The determination of the maximum shear stress can be influenced by errors in the numerical model. In most cases, the maximum shear stress in the pipe is found close to the pipe tip. This is however at a boundary between the pipe- and aquifer domain, with different hydraulic permeabilities. The interface between these boundaries at the tip can result in errors of 50% to 300% for 1D pipe elements (Robbins et al., 2022). Since the model in this research uses 2D pipe elements, this error will be significantly smaller.

Model Validation

This chapter focuses on the model validation. The model is developed in COMSOL-Multiphysics 6.2. At first, the basic model without the addition of the fines influence is validated with the Deltares application D-Geo Flow. The basic model refers to the COMSOL implementation of backward erosion piping without the influence of fines (i.e., silt and clay fractions set to zero). Then the added influence of fines is used in modelling the Hedwigepolder experiment to validate the updated onset of motion criterion. Also the impact of the combination of fines and anisotropy influences is investigated.

5.1. D-Geo Flow validation of basic model

The D-Geo Flow application, developed by Deltares, can calculate a critical head for a dike geometry with as input the hydraulic conductivity of the materials and the d_{70} at the location of the pipe. The IJkdijk geometry, also used by Aguilar and Wewer, is implemented in D-Geo Flow and COMSOL Multiphysics for different model parameters to validate the COMSOL BEP model (Aguilar-López et al., 2016; Wewer et al., 2021). The general onset of motion criterion is used to validate the model, the fines fractions are set to zero at first. The general parameters from Table 5.1 are used in the whole report if not specified further.

Table 5.1: General parameters

Parameter	Value	Unit
Gravitational acceleration (g)	9.81	[m/s ²]
Volumetric mass density of soil particles (ρ_s)	2650	[kg/m ³]
Volumetric mass density of water (ρ_w)	1000	[kg/m ³]
Dynamic viscosity (μ)	0.001	[Pa·s]

5.1.1. IJkdijk geometry

The parameters and geometry as used in D-Geo Flow for the model validation is shown in Table 5.2 and Figure 5.1. The geometry consists of 2 domains, namely the aquifer and the pipe. 2 different boundary types are applied, namely no-flow boundaries and constant pressure boundaries.

Table 5.2: IJkdijk parameters

Parameter	Value IJkdijk	Unit
Aquifer permeability (κ)	$1.07e^{-11}$	[m ²]
Representative grain diameter (d_{70})	0.180	[mm]
Potential seepage length (L)	15.0	[m]
Aquifer depth thickness (D)	3.0	[m]
Mesh size in pipe (D-Geo Flow)	0.1	[m]
Mesh size in pipe (COMSOL)	0.01	[m]

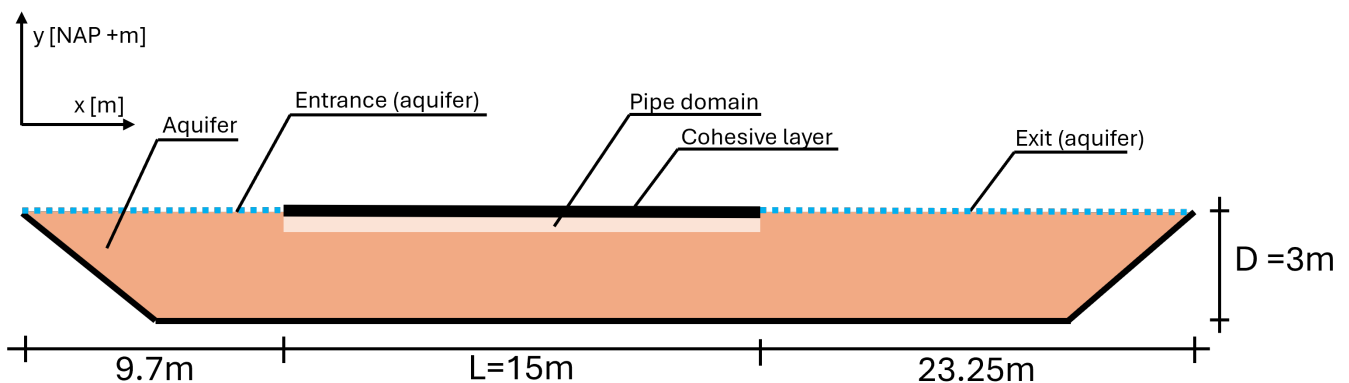


Figure 5.1: Geometry of IJkdijk

5.1.2. COMSOL outputs

Figure 5.2 shows two output graphs from the COMSOL model for the IJkdijk geometry. Figure 5.2a shows the non-rectangular pipe shape. The pipe reached a depth of approximately 2.7 mm at the last time step, the time step for which the pipe fully progressed over the dike base. Figure 5.2b shows the hydraulic head over the dike base. The head drops at the location where the pipe has grown. At the final time step, the hydraulic head drops almost linearly over the dike width.

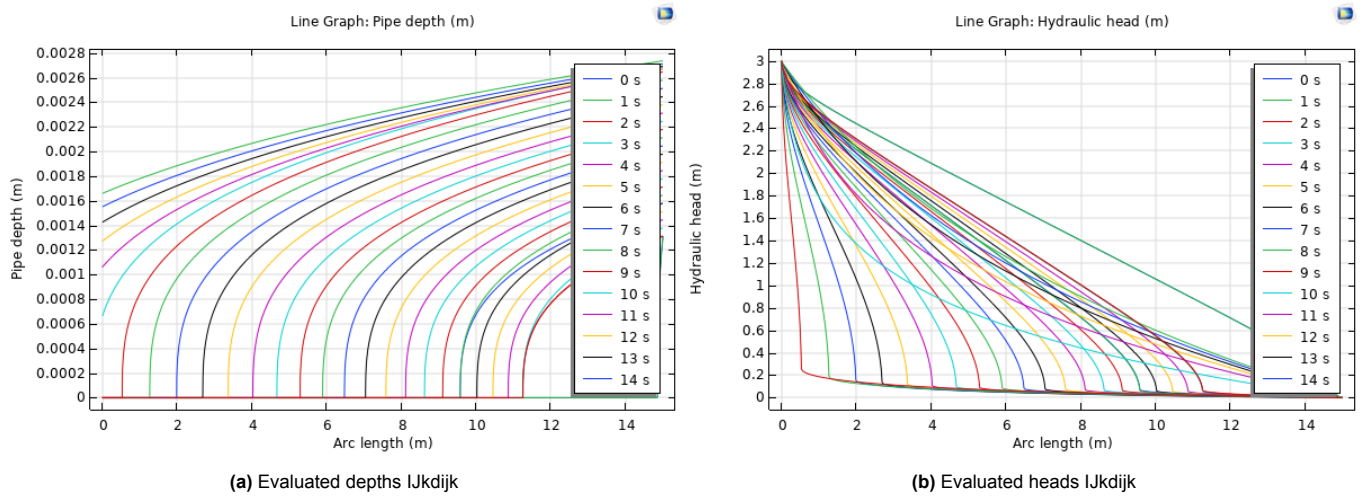


Figure 5.2: Results from COMSOL model. The arc length starts at the outer dike toe (0 m) and continues towards the inner dike toe (15 m)

Figure 5.3 shows the influence of the pipe progression on the hydraulic head over the aquifer. At the location where the pipe is present, the hydraulic head has decreased significantly.

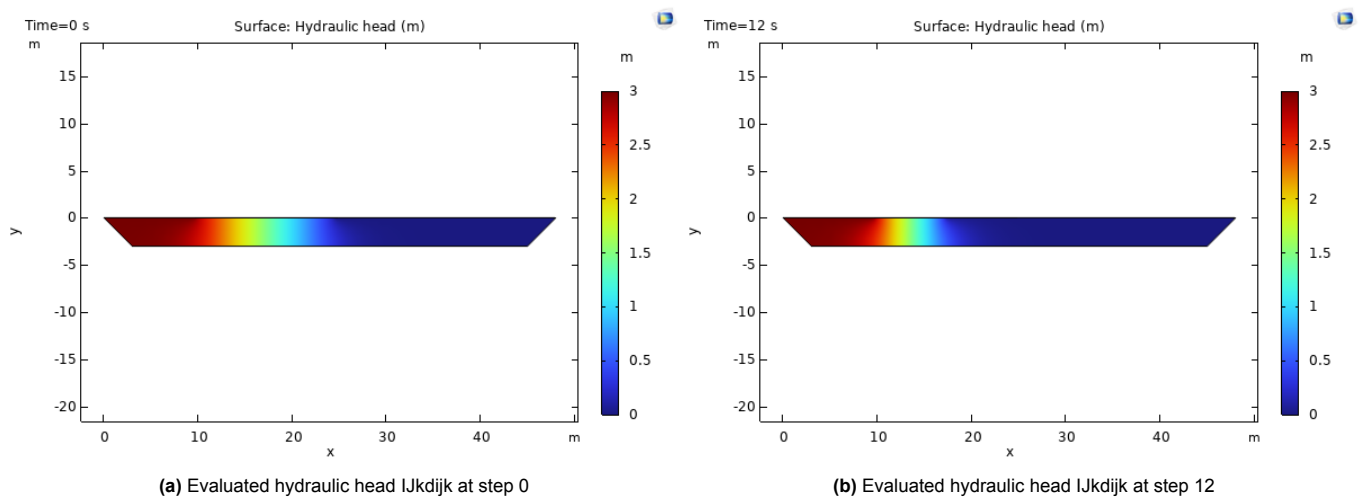


Figure 5.3: Pressure head [m] output from COMSOL at step 0 and 12

The model is run with different values of the particle diameter (d_{70}) and the hydraulic conductivity (k) to find the model sensitivity to these parameters. In Figure 5.4 the results are plotted of the COMSOL model. The combination of low conductivity with large particles is not common, since large particles result in larger voids in the soil, causing higher hydraulic conductivities. Lower values of d_{70} (0.1-0.2 mm) with lower values of k (2-10 m/d) are relevant for tidal deposits. It is important to note that the critical head is found with a precision of 0.1 m. More precision requires longer run times, for which no time was available. Time was limited due to the maximum connection time with the TU Delft VPN-server to be able to run COMSOL-Multiphysics. Deviations in smoothness of the lines in Figure 5.4 are expected to be caused by this lack of precision.

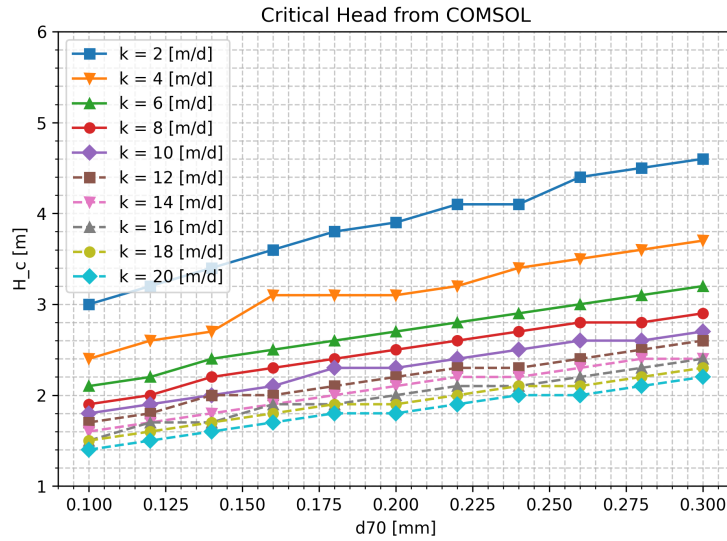


Figure 5.4: Critical head values from COMSOL for IJkdijk with varying d_{70} and k

5.1.3. D-Geo Flow outputs

The same geometry of the IJkdijk is created in D-Geo Flow as in COMSOL. D-Geo Flow is able to find the critical head for which the embankment will fail to backward erosion piping. A screenshot of the D-Geo Flow model is shown in Figure 5.5. This figure shows the critical head in the left side of the embankment. The hydraulic head decreases over the embankment, going from red to blue. The calculation input and output is shown in the right side of the figure. The critical head is found to be 2.1 m, with a critical pipe length of 1.4 m and a pipe depth of 0.001 m. The critical head was determined by incrementally increasing the upstream head in steps of 0.1 m, starting from 0 m, until backward erosion piping was predicted. In the screenshot a mesh size of 1 m is used in the pipe domain. A mesh size of 0.1 m is used for finding the critical heads with more precision in the validation.

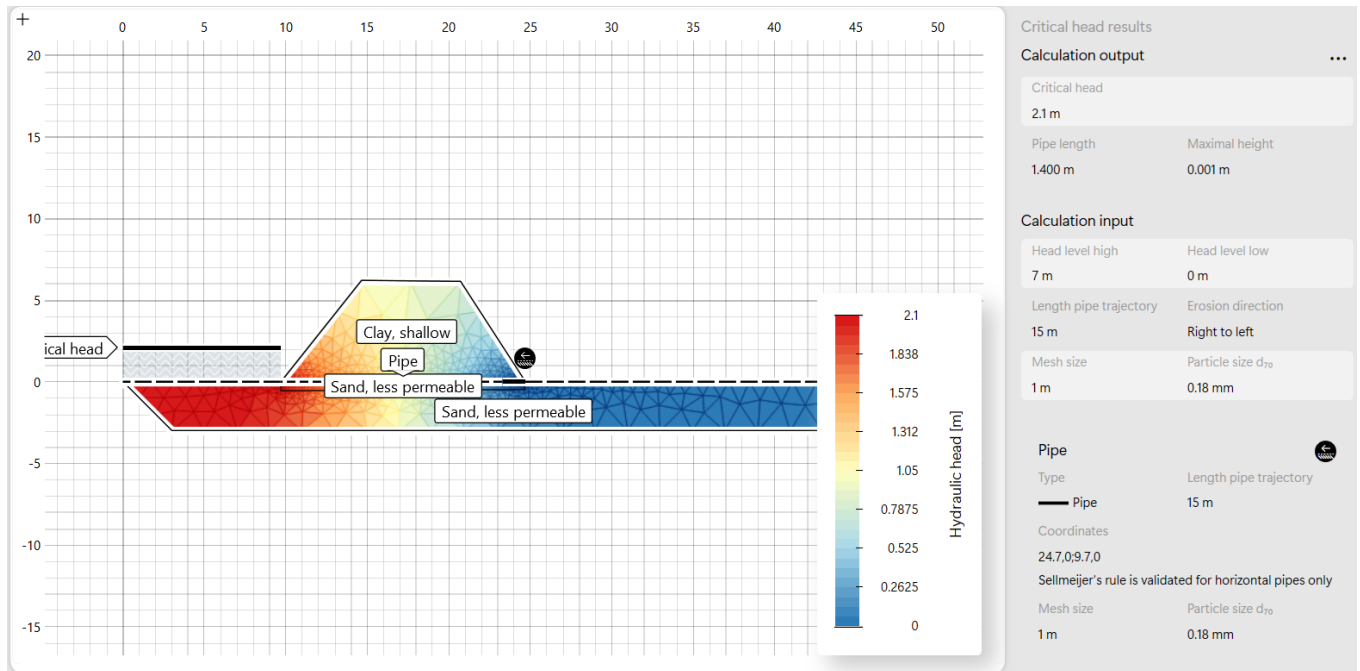


Figure 5.5: D-Geo Flow results with $k=10$ [m/d] and $d_{70}=0.180$ [mm].

The same values of d_{70} and k are used to evaluate the results from D-Geo Flow. The results are found in Figure 5.6. The D-Geo Flow results show similar dependencies on d_{70} and k as the results from the COMSOL model.

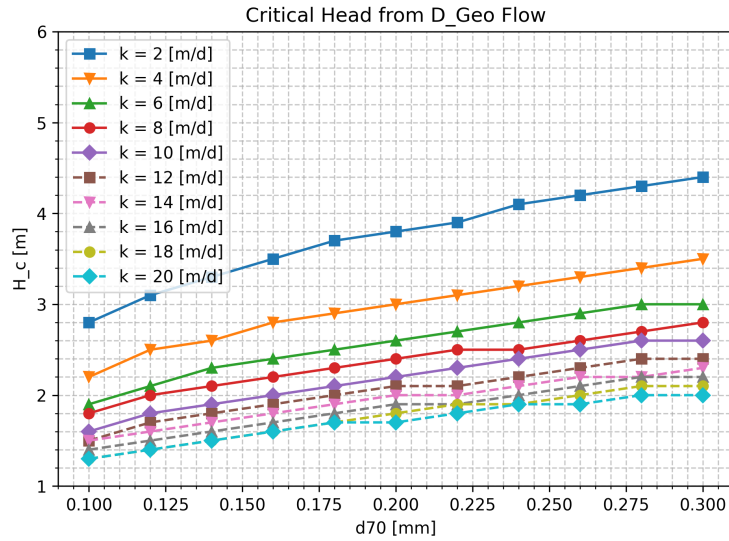


Figure 5.6: Critical head values from D-Geo Flow for IJkdijk with varying d_{70} and k

5.1.4. Model errors

The COMSOL results are compared with results from D-Geo Flow and Sellmeijer 2011 (Eq. 2.4) as seen in Figure 5.7. This plot shows similar trends for all models. D-Geo Flow predicts lower critical heads in general. An important difference between the COMSOL model and D-Geo Flow is the dimensions of the pipe. D-Geo Flow uses 1D pipe elements, COMSOL uses 2D pipe elements. 1D pipe elements lead to more numerical errors at the pipe tip, resulting in higher observed hydraulic gradients at this location (Robbins et al., 2022). An overestimation of the hydraulic gradient causes an underestimation of the critical hydraulic gradient, this could explain the consistent underestimation of D-Geo Flow in comparison with COMSOL.

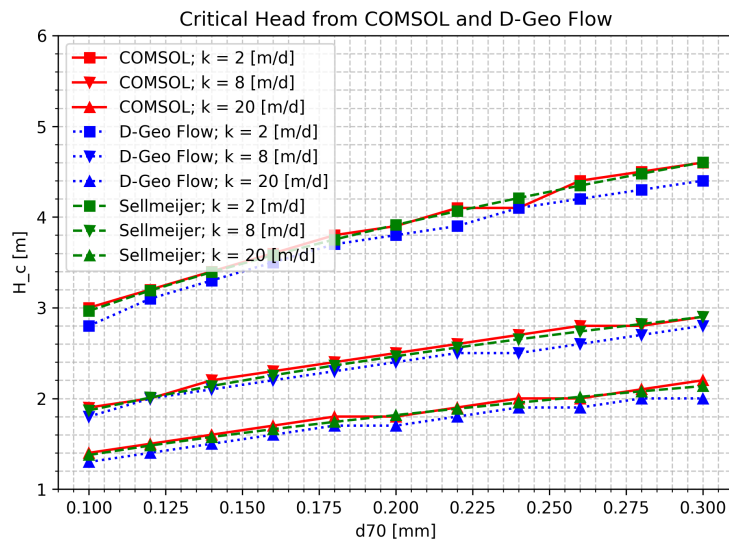


Figure 5.7: Model comparison between COMSOL, D-Geo Flow and Sellmeijer 2011

To validate the COMSOL model, the predicted critical heads from COMSOL are compared with the results from D-Geo Flow by calculating the error in percentages. These results are shown in Figure 5.8a and indicate that the COMSOL model always predicts a higher critical head than the D-Geo Flow model does. Another error plot is made for the comparison with Sellmeijer 2011 in Figure 5.8b, this indicates lower errors than the comparison with D-Geo Flow. Part of the errors will be caused by the hydraulic head step-size used in the COMSOL model of 0.1 m. The lowest observed critical heads are around 1.3 meters, an error of 0.1 m already results in errors of almost 10%. Also some errors could be numerical errors in the model calculations. The errors in Figure 5.8 are calculated with Eq. 5.1 and 5.2.

$$error_{D-Geo\ flow}[\%] = \frac{H_{crit, COMSOL} - H_{crit, D-Geo\ Flow}}{H_{crit, COMSOL}} \cdot 100\% \quad (5.1)$$

$$error_{Sellmeijer}[\%] = \frac{H_{crit, COMSOL} - H_{crit, Sellmeijer}}{H_{crit, COMSOL}} \cdot 100\% \quad (5.2)$$

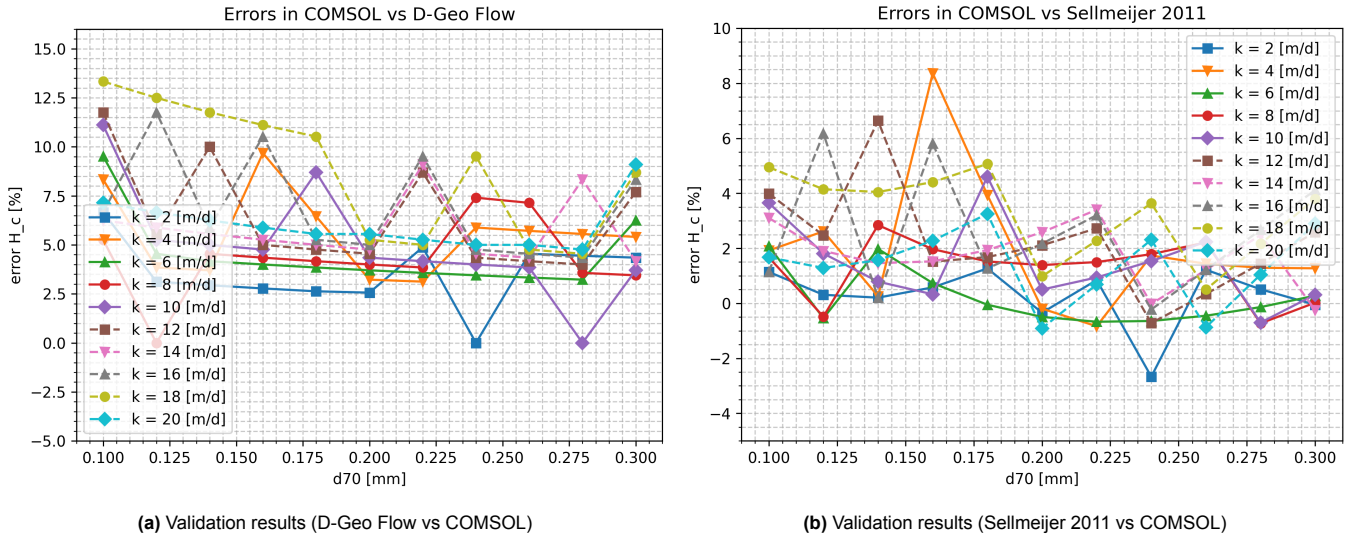


Figure 5.8: Errors between COMSOL, D-Geo Flow and Sellmeijer 2011, found as validation results

5.2. Validation of New Onset of Motion Criterion

In this section a COMSOL model is created with the geometry of a physical experiment to validate the influence of the tidal fines in the onset of motion criterion. The large scale 3D-experiment of the Hedwigepolder was selected for modelling. The experiment parameters are shown in Table 5.3 and the geometry is shown in Figure 5.9. The pipe was observed to be located underneath the upper soil layer, therefore the pipe domain is located below this layer. The upper layer has a low hydraulic conductivity (0.35 [m/d]), therefore the pipe could form underneath this layer. The head at the inner embankment boundary is assumed to be elevated by $0.3 \cdot D_{\text{clay layer}}$ to account for resistance through the clay layer opening.

Table 5.3: Hedwigepolder parameters

Parameter	Value Hedwigepolder	Unit
Upper soil layer conductivity (k)	0.35	[m/d]
Aquifer layer 1 conductivity (k)	1.75	[m/d]
Aquifer layer 2 conductivity (k)	4	[m/d]
Aquifer layer 3 conductivity (k)	2.5	[m/d]
Upper soil layer thickness (D)	0.6	[m]
Aquifer layer 1 thickness (D)	1.4	[m]
Aquifer layer 2 thickness (D)	1.2	[m]
Aquifer layer 3 thickness (D)	0.8	[m]
Representative grain diameter (d_{70})	0.13	[mm]
Potential seepage length (L)	10.0	[m]
Ditch width	1.0	[m]
Mesh size (a_mesh)	0.01	[m]

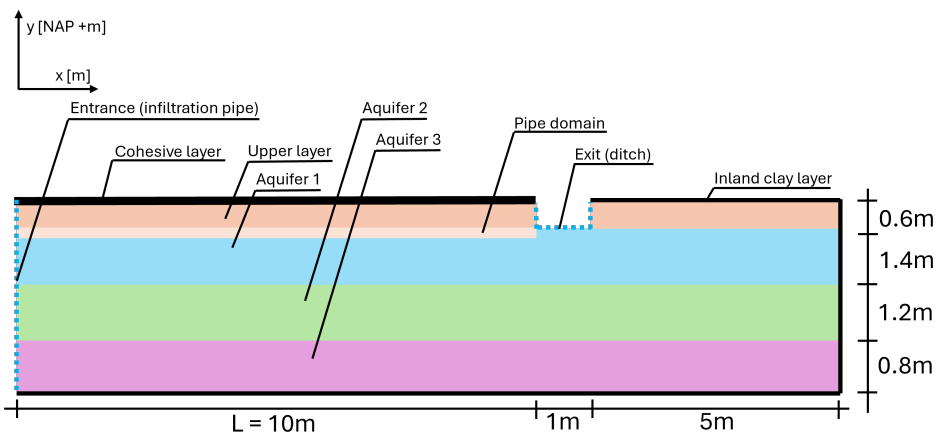


Figure 5.9: Model geometry of Hedwigepolder experiment

The Hedwigepolder experiment consisted of an infiltration pipe at the dike crest, an aquifer consisting of 4 clearly different soil types and an exit point in the dike toe ditch with visible sand boils. Sheet piles are used to border the experiment location and resulted in no-flow boundaries. The different soil layers were all anisotropic, with an anisotropy factor of 3.5 [-]. The upper soil layer was significantly less permeable than the other layers. This layer was first predicted to be the layer where the pipe would grow, however the pipe eventually started to grow in the soil layer below. Figure 5.10 clearly shows the difference in permeability for the different soil layers due to the uneven distribution of the hydraulic head.

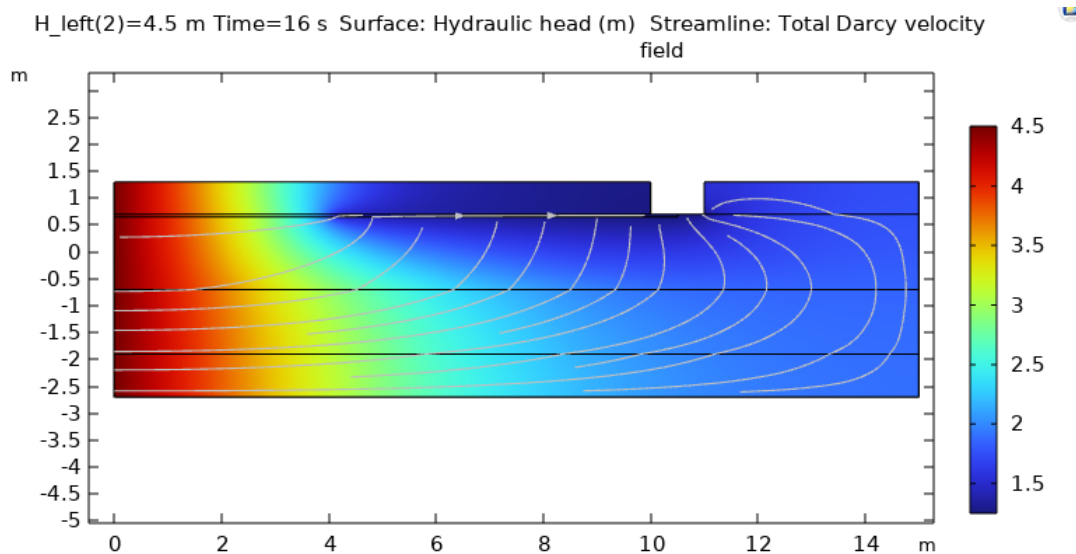


Figure 5.10: Hydraulic head in Hedwigepolder experiment according COMSOL model

The actual critical head as observed in the experiments was NAP +3.65 m, with a head at the ditch of NAP +1.25 m. This results in a critical head difference of 2.4 m. This head occurred in a 3D situation, which is accompanied with more flow towards- and in the pipe than in a 2D situation. The 2D D-Geo Flow model predicted a critical head of NAP +3.1 meters (including anisotropy), which is a critical head difference of 1.85 m. In Table 5.4, results from different combinations of including the anisotropy and fines fractions are shown. It can be observed that including both the anisotropy and fines fraction results in an overestimation of the critical head required for backward erosion piping in the case of the developed model. This overestimation could however also be the cause of modelling the 3D experiment in 2D. In 3D, more groundwater is able to flow to the pipe, which should result in lower critical heads than in a 2D case. Only including the fines fraction and leaving out the anisotropy in the COMSOL numerical model results in the critical head closest to the observed head in the physical experiment. However, the combined influence of fines and anisotropy is closer to the physical reality. The case study will be executed with the fines influences and with no anisotropy influences due to these results being closer to the experiment results, keeping in mind that the combination of fines and anisotropy is theoretically closer to reality.

Table 5.4: Hedwigepolder results

Obtained with	Anisotropy included	Fines fraction included	Critical head [NAP +m]
D-Geo Flow	No	No	3
D-Geo Flow	Yes	No	3.1
COMSOL	No	No	2.9
COMSOL	Yes	No	3.2
COMSOL	No	Yes	3.7
COMSOL	Yes	Yes	4.1
Physical experiment	-	-	3.65

In Figure 5.11 the influence of different clay and silt fractions is shown, according to the COMSOL model including the influence of the fines fraction, but excluding the influence of the anisotropy. The red 'x' shows the silt and clay fraction in the Hedwigepolder experiment. The grey dots show the silt and clay fractions for which the model is ran. The contour plot interpolates linearly between these points.

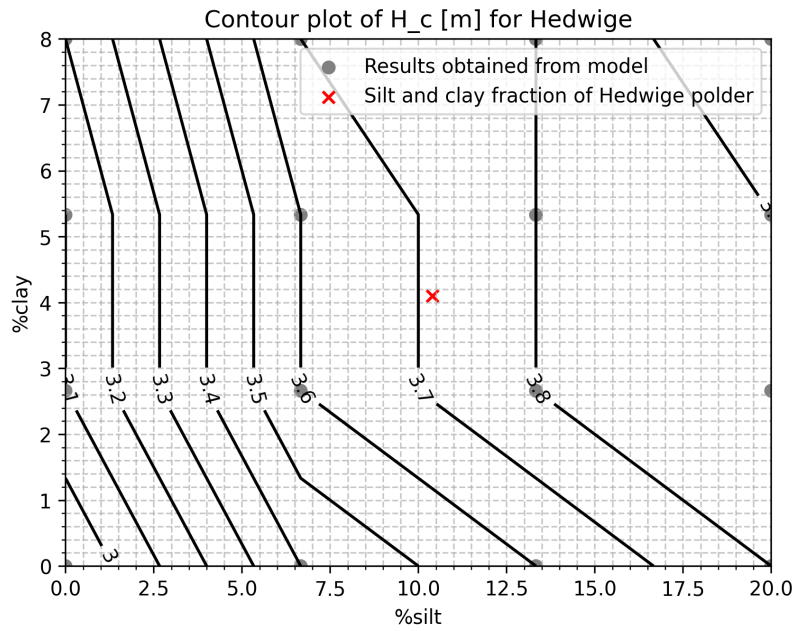


Figure 5.11: Contour plot of critical head values in the Hedwige polder experiment, simulated in COMSOL (fines included, anisotropy excluded)

6.1. Background Groningen sea dikes

6.1.1. Introduction

The model developed in Chapter 5 is applied on two cross-sections of the Groningen sea dikes. A relevant cross-section is found in dike section D of trajectory 6-6, since this section was assessed as vulnerable to backward erosion piping as seen in Figure 6.3 and in Figure 6.4. Also a cross-section which did comply with the current assessment method is selected. This is a cross-section in the more western part of Groningen, in dike section B, which was assessed as safest section against BEP. At this cross-section, a clay layer is expected to be present to possibly form a roof on a pipe. The dike in the eastern part of Groningen lacks a cohesive clay layer and is therefore not sensitive to BEP. The location of cross-section D can be found in Figure 6.1.



Figure 6.1: Section D, the dike section with highest probability of failure (Google, 2025)

6.1.2. History

The sub-soil of the sea dikes in Groningen is formed by tidal deposits. The coast moved seaward due to the deposition of tidal deposits as seen in Figure 6.2. Multiple polders have been made, with new dikes built on tidal deposits. The pumping station Noordpolderzijl is located in dike section D.

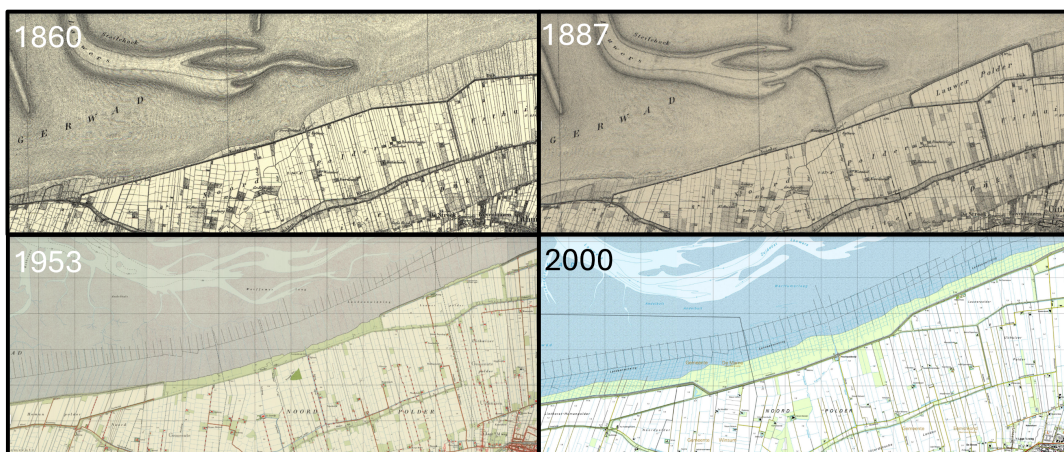


Figure 6.2: History Section D (Topotijdreis, 2025)

6.1.3. Latest assessment

The latest assessment was according to the WBI 2017 (Wettelijk Beoordelingsinstrumentarium) (Rijkswaterstaat, 2023). The assumptions and calculations made for this assessment are recorded in an assessment log by the water authority (Noorderzijlvest, 2022a). Relevant safety limits of dike trajectory 6-6 are shown in Table 6.1.

Table 6.1: Safety limits trajectory 6-6

Limit	Probability [year ⁻¹]
Warning level	1/3000
Lower safety level	1/1000

The result per dike section is shown in Figure 6.3 and 6.4. The safest (location A) and least safe (location B) are shown in the map. These probabilities of failure lower than the warning level and lower safety level as indicated above. This is due to the warning level and lower safety level being indicated over the whole dike trajectory for all possible failure mechanisms. Other failure mechanisms as macro-instability or overtopping also contribute to the total probability of failure. As an initial estimate, backward erosion piping was allowed to contribute 24% to the total probability of failure (Rijkswaterstaat, April 2014). Currently, choices can be made to distribute the contribution of different failure mechanisms differently. Calculating the probability of failure of the dikes is outside the scope of this research. This study aims to determine a deterministic critical head, without incorporating probabilistic parameter distributions.

Vaknaam	Faalkans [jaar-1]	Toetsoordeel per vak
STPH-KMP37100	4.2686E-08	IIv
STPH-KMP38500	4.2686E-08	IIv
STPH-EH13600	FV	Iv
STPH-EH56200	FV	Iv
STPH-KMP48855	FV	Iv
STPH-KMP53040	FV	Iv
STPH-KMP54100	FV	Iv
STPH-KMP56700	1.5632E-06	IIIv
STPH-KMP61100	4.2417E-06	IVv
STPH-KMP66400	1.4636E-07	IIv
STPH-KMP69300	8.5374E-10	Iv
STPH-KMP72000	3.4448E-07	IIv
STPH-KMP76000	3.7402E-06	IIIv
STPH 6-6	8.3598E-05	IIIIt

Figure 6.3: Results of latest BEP assessment (Noorderzijlvest, 2022b) (in Dutch)

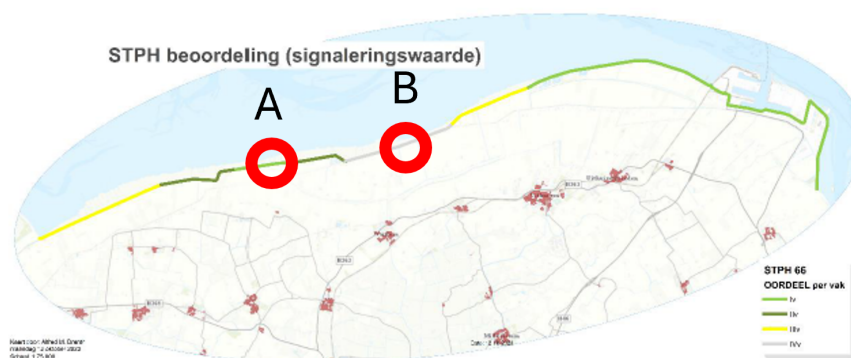


Figure 6.4: The assessment results per section for the BEP mechanism (Noorderzijlvest, 2022b). The sections evaluated as being the strongest and weakest are indicated with location A and B. (in Dutch)

The inland water level was chosen to be equal to the surface level for the latest assessment, based on observations during earlier high water situations. This results in an inland water level of NAP +1.6 m for location A and NAP +1.55 m for location B. The latest assessment assumed no influences of the foreshores, since the ditch directly at the sea side of the dike can possibly cause an entrance point for the seepage. The outer water levels used in the latest assessment are NAP +5.7 m for the warning level and NAP +5.37 m for the lower safety level.

6.1.4. Technical aspects

To apply the numerical COMSOL model to the case study, the subsurface profiles and subsurface properties should be observed. The regional water authority Noorderzijlvest has carried out soil drilling and laboratory experiments for the sea dikes. A subsurface build-up of dike section D (12% fines content with 7% clay particles and 5% silt particles) is shown in Figure 6.5 and Figure 6.6.



Figure 6.5: Subsurface profile example (B63807 00.00-05.00) NAP +1.15m to NAP -2.85m (Wiertsema & Partners, 2018)

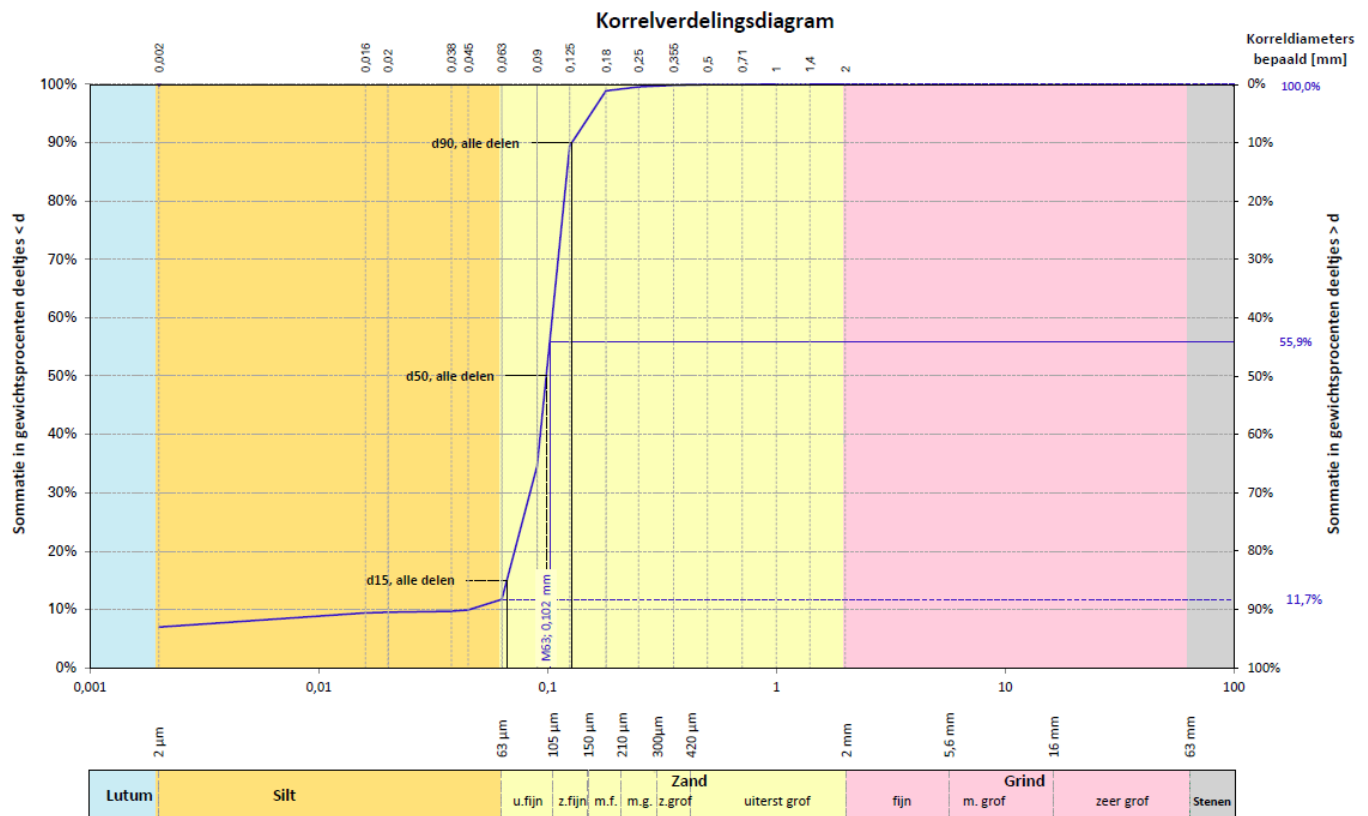


Figure 6.6: Particle grading (MB63807 M006-b) NAP -1.22m to NAP -1.45m (Wiertsema & Partners, 2018) (in Dutch)

The soil drilling profile shows layeredness in the subsoil of the dike. Fugro has conducted an analysis of the soil, also to find the anisotropy underneath the Groningen dikes (Furgo, 2022). It is observed that the anisotropy at location B is around 10 [-]. This anisotropy is however not applied in the model, since Chapter 5 showed that the combined influence of anisotropy and fines results in an overestimation of the strength against backward erosion piping.

6.2. Geometry and materials

6.2.1. Aquifer

The dikes in the western part of Groningen mainly consist of sand. The top layer consists of clay. At a depth of about NAP -15 m a clay layer is present. A heavily sand-clay layered tidal deposit is present at NAP 0 m. The many clay layers could form a cohesive and water tight roof for a pipe, as also assumed in the latest assessment of the Groningen dikes. Two examples of such locations for a pipe are shown in Figure 6.7. The critical cross-sections for backward erosion piping are locations where a thick aquifer is present. The aquifer is located between two cohesive layers. For the Groningen case, the aquifer is between 5-15 meters thick. The locations in the aquifer where BEP could occur are shown in Figure 6.7. Only the vertical indicated location is of importance, the exact horizontal location of the pipe can vary.

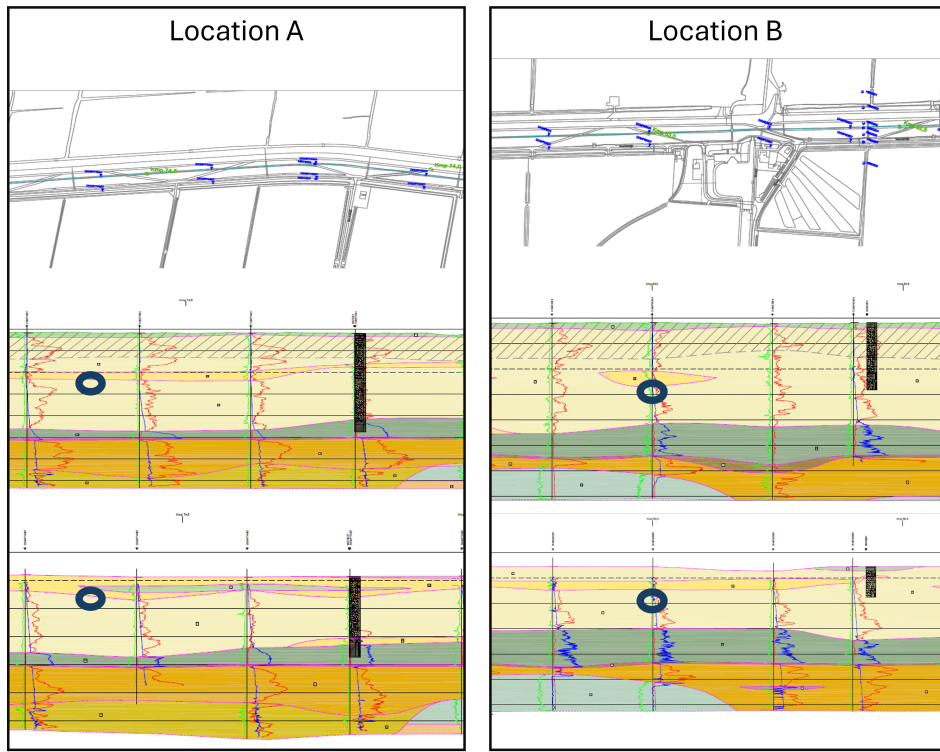


Figure 6.7: The locations selected for modelling in the Groningen dike. The upper figure is the top view, middle figure is the length profile at the crest and the lower figure the length profile at the inner toe.

LITHOSTRATIGRAFISCHE LEGENDA							
1	Hoofdzakelijk klei, zwak tot sterk zandig of silthoudend, plaatselijk puinresten	Opgebracht	Anthropogeen	4	Zand, zeer fijn tot matig fijn, zwak tot matig silthoudend, zwak tot sterk humeus	Formatie van Bortel Laagpakket van Wierden (Eolisch)	Pleistocene Weichselien
2	Hoofdzakelijk zand, zeer fijn tot matig fijn, plaatselijk puinresten			5	Klei, zwak tot matig silthoudend, zwak humeus, plaatselijk gelaagd met zand, plaatselijk houresten	Formatie van Bortel Laagpakket van Singraven (Beekafzettingen)	
1	Klei, plaatselijk zandig, plaatselijk gelaagd met zand, zwak tot matig siltig, zwak humeus, schelpen en schelpresten	Formatie van Naaldwijk (Mariene afzettingen)	HOLOCEEN	6	Zand, zeer fijn tot matig fijn, zwak tot matig silthoudend, schelpresten	Eem Formatie (Mariene afzettingen)	Pleistocene Eemien
2	Zand, zeer fijn tot matig fijn, zwak tot sterk silthoudend, plaatselijk gelaagd met klei, plaatselijk schelpen en schelpresten			7	Klei, zwak tot matig silthoudend, schelpresten	Formatie van Drente Laagpakket van Gieten (Glactaal, morene-afzettingen)	
2a	Zand, zeer fijn tot matig fijn, sterk gelaagd met klei, zwak tot sterk silthoudend, plaatselijk schelpen en schelpresten			8	Keileem, Leem, plaatselijk zandig, grindhoudend		
2b	Klei, plaatselijk zand, plaatselijk gelaagd met zand, zwak tot matig siltig, zwak humeus, schelpen en schelpresten			9	Zand, uiterst fijn tot zeer fijn, plaatselijk kleilagen		Formatie van Peelo (Fluvioglaaciaal)
3	Veen, plaatselijk zwak klei of zandig			10	Potklei, zwak tot matig silthoudend of zandig, plaatselijk gelaagd met zand	Formatie van Peelo Laagpakket van Nieuwolda (Fluvioglaaciaal)	
		Formatie van Nieuwkoop Bastveen laag					

Figure 6.8: Soil legend (in Dutch)

6.2.2. Inflow and exit point

In front of the Groningen dikes, long foreshores are present with lengths varying from 300 to almost 1000 meters. This foreshore consists of extremely fine deposits, but an exact hydraulic conductivity of the foreshore is unknown. The hydraulic conductivity is assumed to be 0.1 m/d, as this conductivity would be closer to the conductivity of clay than of sand. A deep ditch is present directly in front of the dike, this ditch could reach through the whole clayey foreshore layer and be an entrance point for groundwater flow. The model is run with the ditch as inflow point. The geometry without the ditch would lead to a safer dike due to the lengthened seepage path, thus a filling of the ditch could be beneficial.

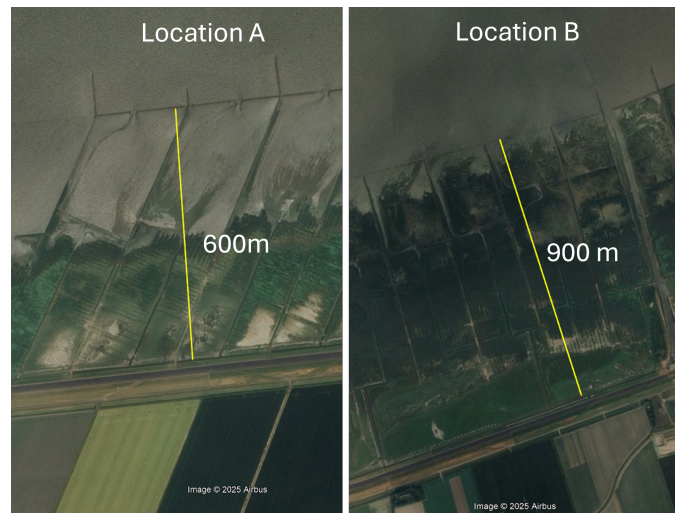


Figure 6.9: Aerial view of the foreshore in front of the Groningen sea dikes (Google, 2025)

The exit point for BEP is most likely the ditch at the inland side of the dike. The water tight clay layer is thinner at this location, therefore uplift could occur more easily. The hinterland behind the ditch is fully covered by a clay layer, given no other possible exit points. No sand boils have been observed behind dikes in Groningen before.

6.2.3. Geometry parameters

The geometry of the Groningen case for both location A and B is shown schematically in Figure 6.10. Besides the usual aquifer and pipe domain, a domain is added to act as the foreshore. This domain has a lower hydraulic conductivity than the aquifer, since the foreshore is formed by slow tidal movement depositing fines. The water enters the aquifer on three different locations, namely in the porous soil in front of the foreshore, through the less permeable foreshore and through the ditch between the foreshore and the dike. Figure 6.10 is not to scale, in reality the x-dimensions in the order of 100 times larger than the y-dimensions. No-flow boundaries are applied on the inland behind the ditch, on the bottom of the aquifer and on the left and right vertical boundaries of the aquifer. In reality, the left and right side of the aquifer are not closed. The model of location B is run once with the left and right boundaries as constant head boundaries instead of no-flow boundaries, this did not influence the observed critical head. The difference between the use of no-flow or constant head boundaries on the left and right boundary might be significant if anisotropy is included in the model. The anisotropy is not included in this model because Chapter 5 concluded that this will possibly lead to an overestimation of the critical head. Used parameters in the COMSOL model are shown in Table 6.2.

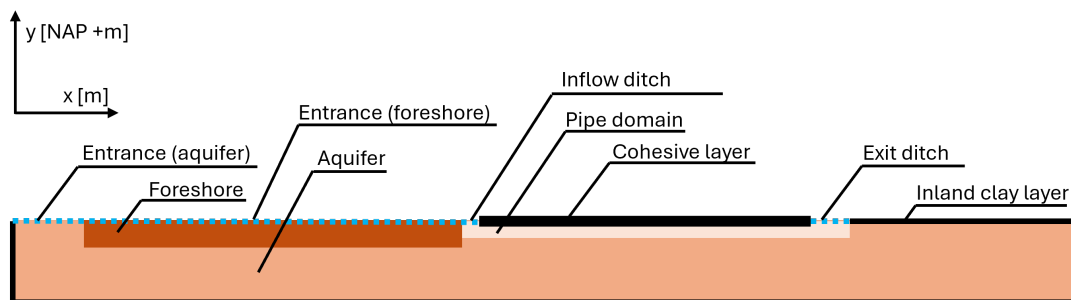


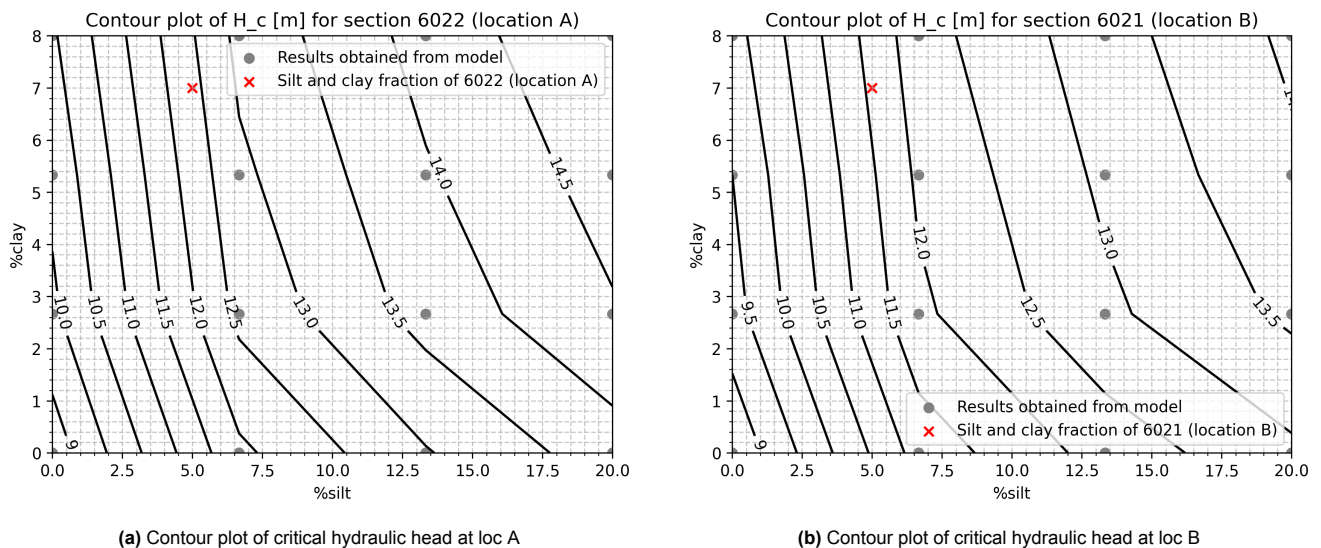
Figure 6.10: Model schematization (not to scale)

Table 6.2: Groningen case parameters (warning level and inland water level are statistically safe, other parameters are mean values)

Parameter	Value location A	Value location B	Source
Foreshore length	600 [m]	900 [m]	Google Earth
Foreshore thickness	2.5 [m]	1.2 [m]	Noorderzijvest, 2022a
Foreshore hydraulic conductivity	0.1 [m/d]	0.1 [m/d]	Assumption
Inflow ditch width	1 [m]	1 [m]	Assumption
Exit ditch width	1 [m]	1 [m]	Assumption
Aquifer thickness	9 [m]	7 [m]	Wiertsema & Partners, 2018
Aquifer hydraulic conductivity	8 [m/d]	8 [m/d]	Noorderzijvest, 2022a
Dike base length	90 [m]	80 [m]	Wiertsema & Partners, 2018
Inland water level	NAP +1.60 [m]	NAP +1.55 [m]	Noorderzijvest, 2022a
Warning level	NAP +5.7 [m]	NAP +5.7 [m]	Noorderzijvest, 2022a
Anisotropy (actual)	10 [-]	10 [-]	Furgo, 2022
Anisotropy (as applied in model)	1 [-]	1 [-]	Assumption
d_{70}	0.1364 [mm]	0.1326 [mm]	Noorderzijvest, 2022a
%clay	7 [%]	7 [%]	Wiertsema & Partners, 2018
%silt	5 [%]	5 [%]	Wiertsema & Partners, 2018
θ	37 [deg]	37 [deg]	White, 1940

6.3. Results

According to the Sellmeijer 2011 rule, the critical head at location A is 8.22 [m] and at location B is 7.75 [m]. These critical heads are significantly higher than the warning level of NAP +5.7 m. The model predicts a higher critical head than the Sellmeijer 2011 rule even when fines content is set to zero. This could be due to the added foreshore and the size of the inflow and exit ditch. The vertical no-flow boundaries of the aquifer were suspected to also influence the results, the model was however also run with constant head boundaries on the vertical aquifer boundaries and this did not influence the critical head. In Figure 6.11a and Figure 6.11b contour plots are shown with the influence of silt and clay. For location A the 5% silt and 7% clay result in a critical head of 12.4 meters and for location B a critical head of 11.6 meters. This results in a strength factor of 1.5 [-] for both locations. The strength factor is defined as the ratio of the critical head predicted by the COMSOL model to that predicted by the Sellmeijer 2011 rule. The critical head found with the COMSOL model is thus 50% higher than the critical head predicted by Sellmeijer 2011. Both locations are modelled with the same silt and clay fraction, therefore it is expected that they have the same strength factor. The Python code is found in Appendix C.

**Figure 6.11:** Contour plots of critical heads dependent on silt and clay fractions

It is important to take into account the limitations of these results. The model provides a 2D approximation of a 3D physical situation, this leads to overestimation of the critical head. The model also uses an onset of motion criterion which is based on limited physical experiments with different influences of anisotropy. The final numerical model is highly sensitive to the clay and silt fractions. The clay and silt fraction are however not constant over vertical or horizontal distances and can vary a lot. The silt and clay fractions are based on laboratory tests of soil samples from the aquifer closest to the assessed locations. It should be noted that the possibility exists that the silt and clay fraction is different at a location of multiple meters from the assessed locations and this research did not include statistical distributions of soil property variation in space.

7.1. Soil profile heterogeneities

Soil profiles are highly heterogeneous. This causes uncertainties in the schematization of dike geometries in the numerical model. Each soil layer is modelled as having one global characteristic particle diameter (d_{70}), permeability and porosity, however this varies in reality. These heterogeneities influence the pipe shape and the direction of the pipe propagation. In the used numerical model, the pipe is assumed to propagate in a straight line. In reality, the pipe will follow the path of least resistance and can change direction if weaker soils are found close to the pipe path.

The new onset of motion criterion is heavily dependent on soil properties now the clay and silt fractions are included in the equation. Clay and silt fractions are however hard to determine over the whole length of a dike trajectory. Uncertainty in soil properties should be taken into account in the assessment of dikes by using stochastic input parameters. To realistically include the clay and silt fractions in the assessment, many soil samples have to be observed in a laboratory to be certain on the actual presence of these fines. This will be an expensive and time consuming process, however not as expensive as new dike reinforcements.

7.2. Physical understanding of BEP process

7.2.1. Limited dataset of tidal deposit experiments

There is limited data available on individual influences by %clay versus %silt. These fractions have different influences on the physical behaviour of BEP. The clay influences the cohesion and silt causes different particle embedding in a fine matrix. Most sediments used in experiments include both a clay and a silt fraction. If more experiments will be focused on using only a clay or only a silt fraction, the different influences of these fractions can be distinguished better.

Anisotropy and a fines fraction are both present in tidal deposits, both influencing the strength against backward erosion piping. Most physical experiments on fines did not include the influence of anisotropy, since the soil samples of small and medium scale tests are placed by hand. Small and medium scale tests can possibly even include a tilted version of anisotropy, if soil samples are prepared in tubes, layer by layer, causing the horizontal hydraulic conductivity to be lower than the vertical conductivity. Only the large scale experiments contained the realistic influence of anisotropy and multilayeredness. When modelling the Hedwigepolder experiment, combinations with influences of both anisotropy and the fines fraction were looked at. This however showed that taking into account both the anisotropy and the fines fraction results in an overestimation of the strength against backward erosion piping.

7.2.2. 3D effects and time-dependencies

3D effects are present in real-life BEP problems, with both 3D pipe propagation and 3D groundwater flow. In the model used in this thesis, only 2D calculations are made with pipe progression in a single direction. Large scale experiments as the Hedwigepolder experiment are conducted in a 3D BEP environment. Using data from these experiments for the validation of a 2D model is questionable since the third dimension significantly influences the groundwater flow towards the pipe and therefore also the forcing of the sediment particles inside the pipe.

In real-life situations, the hydraulic head is also time-dependent and will not stay at a maximum value for days in a row. The tidal fluctuations of the water levels can be included in time-dependent BEP models to take into account this limited exposure to high water levels. The developed model cannot give an indication on the time it takes for the pipe to fully develop underneath the dike.

7.2.3. Pipe size and shape

In the developed model, equations are used for the pipe depth profile which are validated with physical experiments. These equations have not been used in numerical models before. This approach should be further validated. The fictitious permeability formulation assumes a wide and shallow pipe geometry, which may not reflect the actual pipe dimensions observed in physical experiments. It is hard to obtain physical experiment results for the pipe shapes and sizes as found in reality, because physical experiments are man-made setups, often with a transparent and smooth plate as the pipe roof. The behaviour of a pipe underneath a dike is hard to monitor without interfering in the piping process.

7.3. Numerical limitations

Numerical models are not exact, therefore all numerical models will contain numerical errors to some extent. These errors occur in time or in space and are often dependent on the (time) step size or mesh size of the model. No time-dependency is added in the model developed in this report, but due to the stepwise steady-state nature of the model, the step size could still lead to numerical errors. Errors due to the step size can be caused by increasing the pipe length with too large steps. If the pipe progression step is too large, the model may bypass the critical pipe length at which backward erosion initiates, leading to an underestimation of the system's vulnerability. Spatial numerical errors can occur between the pipe- and aquifer domain, while the highest shear stresses inside the pipe are observed close to this location. A sudden jump in permeability is applied at the border between the pipe and the aquifer, this sudden jump is hard to locate exactly as the mesh size of the model is relatively large. The accuracy of the stresses at the pipe tip are however of significant importance when searching for the peak stresses in the pipe to check the onset of motion criterion. The mesh size is selected larger than 0.01 meters for full analysis. Smaller mesh sizes decrease the computational speed, making the analysis not possible in a short time-span. The bigger mesh sizes can however cause larger errors in the model results, making the results less reliable.

7.4. Case study

For the case study in Groningen, a strength factor has been found of 1.5 [-] for both locations. This result is however dependent on some assumptions made for the case study. These assumptions are related to the influence of the foreshore, not taking into account anisotropy, the selection of the silt and clay fractions, the focus on BEP propagation instead of BEP initiation and uncertainties due to the scale of the dike cross-sections.

Foreshore and anisotropy influences

The foreshore can influence the seepage length of the dike. In the case study, the ditch in front of the dike is assumed to be deeper than the height of the foreshore. This caused the influence of the foreshore to be limited to the size of the inflow point and having no influence on the seepage length. If the anisotropy was included, the vertical intrusion of groundwater in the ditch would experience a high resistance due to the lower vertical permeability of the soil. Including anisotropy could therefore increase the strength against BEP even further. Anisotropy could however also influence the strength negatively in certain cases.

Selected silt and clay fraction

To select the clay and silt fractions of the right location, some assumptions are made. Multiple laboratory experiments have been conducted to determine the sieve curves for different locations at different depths. Many of these sieve curves are taken from samples inside non-representative soil layers. The relevant soil layer will be the aquifer just below an aquitard. Only one of the found sieve curves was found to be in this relevant layer, since most sieve curves were from the aquitard itself with clay fractions of higher than 8%. More sieve curves have to be made to include more accurate silt and clay fractions.

BEP failure path

The model as developed in this thesis looks into the propagation of backward erosion piping. The model is run with an initial pipe present in the geometry and the model determines whether the pipe will continue to progress or remain stable. However, other conditions have to be met for the pipe to initiate. The clay layer inside the ditch behind the dike has to be ruptured by uplift for the groundwater to start flowing outside the aquifer. Heave has to start after this to start forming a pipe. The case is not checked on uplift or heave, this is not taken into account in the critical head. However, this must be considered to perform a full assessment and determine the probability of failure of the dike.

Uncertainties due to the scale of the dike cross-section

The Groningen sea dike has a long seepage path of almost 100 meters at some locations. This scale will influence the uncertainty of the results negatively, since the possibility of the presence of pipe paths with lower resistance will increase. In this research however no uncertainty is taken into account for the soil characteristics. The implementation of soil characteristics uncertainties is needed to draw usable conclusions on the actual safety of the dike against BEP. To estimate the probability of failure for the Groningen sea dike, stochastic parameters have to be used as input for the model.

Conclusion and Recommendations

8.1. Conclusion

The conclusion is drawn by looking into the sub-questions as shown in the next subsections at first. A final subsection reflects on the main research question as determined in the introduction.

8.1.1. How is backward erosion piping currently modelled?

Currently, the analytical Sellmeijer 2011 rule is used in the assessment of dikes on BEP. In research, numerical models are developed to assess dikes on BEP and are applied in the official assessments (D-Geo Flow). Numerical models can give a more tailored assessment, since these models give the possibility to include more complex geometries, interaction between different processes, 3D behaviour and time-dependencies. The influence of tidal fines is however not yet included in the official used numerical model.

8.1.2. How do tidal deposits influence soil properties?

Tidal deposits are formed by sedimentation of soil particles near and at the shore. Light fines are able to settle due to slow tidal water flow. Coarser particles are able to settle near shore during storms. Flow velocities are constantly larger in rivers, therefore coarser and more homogeneous particles are present in riverine deposits. The fines fraction ($< 63 \mu\text{m}$) can be split up in a clay fraction ($< 2 \mu\text{m}$) and in a silt fraction ($2 \mu\text{m} < \text{silt} < 63 \mu\text{m}$). Clay causes cohesive forces in the soil, giving more strength against BEP. Silt influences the embedding in the fine soil matrix, influencing the bedding angle of the soil, also resulting in more strength against BEP.

Tidal deposits also consist of more small sand and clay layers with different properties. The layering is present on different scales and can cause different hydraulic conductivities in horizontal and vertical direction. The presence of different soil layers in meter scale is defined as multilayeredness. Differences in horizontal and vertical conductivities on particle scale is described with the term anisotropy, causing different hydraulic conductivities in vertical and horizontal direction in one single soil layer.

8.1.3. When will erosion progress in soils with a fines fraction?

Erosion will progress when the shear force on a sediment particle is larger than the critical shear force. The main forces on the particle are drag and weight. These forces are balanced by the normal force which is dependent on the bedding angle. The drag force is caused by water flow, which is initiated by a hydraulic gradient. A commonly used onset of motion criterion for BEP is the criterion developed by White. White used a constant bedding angle and no cohesive forces. By adding a dependency on the silt fraction in the bedding angle and a dependency on clay in an additional cohesion term in the onset of motion criterion, the influence of a fines fraction is included. Cohesion is only implemented as a horizontal acting force, since the horizontal forces on the particle are dominant. The parameters describing the dependencies on clay and silt are empirically fitted with data of physical experiments by Deltares.

Different fits are explored. Silt and clay fractions are found to be better predictors than mud or the fines fraction as a whole. Also the use of a 95% conservativeness is recommended, since the spread of the physical experiment results is large. Only 5% of the observed experiments have a lower critical head than the head as predicted by the onset of motion criterion following from the fit on silt and clay with a 95th percentile conservative estimate.

8.1.4. What is the current water safety situation at the Groningen sea dike?

In the latest assessment of the Groningen sea dikes in 2022, one dike section is assessed as possibly not compliant with the lowest safety standard on BEP. Other sections are assessed more positively and the eastern sections have been assessed to not be prone to BEP due to the lack of a suitable cohesive layer to act as a pipe roof. The local water authority however expected the negatively assessed sea dikes to be possibly stronger than the current assessment indicated due to the presence of tidal fines.

At the Groningen sea dikes, also anisotropy is observed and large foreshores are present, up to a length of 1000 meters. This also influences the strength against BEP positively. The influence of the foreshore is limited due to a deep ditch at the sea side of the dikes.

8.1.5. How to develop and validate a numerical model to assess BEP in tidal deposits?

A 2D stepwise steady-state model is developed in COMSOL-Multiphysics 6.2. The model assumes Darcyan water flow, with a fictitious permeability inside the pipe domain. The pipe follows a cube root shape, making it shallower near the tip than at the exit at the inland side. For each model step, the maximum shear stress inside the pipe is compared with the critical shear stress. If the critical shear stress is exceeded, the pipe will be deepened and the new depth is used to calculate a new pipe length. The pipe keeps progressing, until the pipe has grown fully over the length of the dike.

The basic model is validated by comparing it with D-Geo Flow. The IJkdijk geometry is used with different hydraulic conductivities and particle diameters. Errors in the difference in critical hydraulic heads between D-Geo Flow and COMSOL are between 0-10%.

The influence of the fines fraction and anisotropy is validated with a D-Geo Flow model of the Hedwigepolder experiment. This showed that the combined influence of fines and anisotropy causes overestimation of the safety against BEP. If only the influence of the fines fraction is used, the predicted head is 3.7 meters, instead of the actual 3.65 meters as observed in the experiment.

8.1.6. How are the Groningen sea dikes evaluated on safety against BEP according to a numerical model for BEP in tidal deposits?

A higher strength factor than the analytical 1.4 [-] rule, can be found for soils with high fractions of clay and silt by fitting the onset of motion criterion on the results of multiple physical experiments. For the Groningen case, a strength factor of 1.5 [-] is found with a silt fraction of 5% and a clay fraction of 7% at location A and B. This extra strength is strongly dependent on the exact clay and silt fractions, which are hard to determine with a high precision at each location. The limitations of this result are discussed in Chapter 7. The model finds the critical hydraulic head for both locations to be significantly larger than the design water level, this indicates that the sea dikes are safe. However, no stochastic parameters are used in the model, therefore the uncertainties of different parameters are not taken into account and the probability of failure of the dike sections is not calculated.

8.1.7. Main research question

In Chapter 1 the main research question was stated as follows:

- What is the impact of an onset of motion criterion including the fines fraction on the assessment of backward erosion piping using numerical models?

It can be concluded that using an onset of motion criterion including the fines fractions in numerical models results in higher predicted critical hydraulic heads. This increase in critical head is in specific cases larger than the strength factor of 1.4 [-] as determined for analytical assessments. Smaller clay and silt fractions can result in strength factors smaller than 1.4 [-]. A clay fraction has a stronger influence on the strength factor than a silt fraction. The final fit of the onset of motion criterion is a conservative fit and follows a rooted dependency. A non-conservative fit was tested and resulted in more linear dependencies. The conservative fit is finally selected due to the large spread in experimental results. A conservative fit with dependencies on mud and fines is explored, but is found to result in strength factors below 1.4 [-] for each possible mud and fines fraction. It is important to note that the current implementation of a new onset of motion criterion in a numerical model is limited as described in Chapter 7. Many of these limitations can however be overcome, by upgrading the 2D model to a 3D model, by using stochastic parameters or by conducting more research on the physical behaviour of soil particles in sediments containing clay and silt fractions.

8.2. Recommendations

8.2.1. Future physical BEP experiments

The exact influences of cohesion and embedding in a fine soil matrix on the strength against backward erosion piping are still hard to grasp. In this research the final used influences are fitted on experiments which in most cases contain both clay and silt. More experimental BEP results relating the critical shear stress to respectively cohesion and embedding in a fine matrix are needed to better capture the physical behaviour.

Also the combined influence of fines and anisotropy should be explored further. Anisotropy and fines can be present simultaneously in real life cases. In all small- and medium-scale tests, only fines were present and no influences of the anisotropy were added in the experimental setups.

8.2.2. Future physical experiments on particle scale

The parameters inside the new onset of motion criterion are determined by fitting data of physical BEP experiment. The onset of motion criterion is analysed fundamentally by focusing on a single particle and analysing the influence of bedding angle and cohesion on the onset of motion. Experiments on the effect of cohesion on the onset of motion of a single particle could help determine the relation between the clay fraction, the fraction of area of a particle over

which cohesion works and the total cohesive force on a particle. Also a better relationship between silt fraction and bedding angle can be determined by measuring the onset of motion of a particle on a sand bed with different silt fractions.

8.2.3. Increase computational capabilities

The results of this thesis are partly limited by the computational time of the numerical model. A finer mesh gives a more accurate result, but takes more time to obtain the results. The model already uses a consistent mesh, making the re-meshing of the model unnecessary. Re-meshing is time consuming, therefore it is advised to also use a consistent mesh for next models. If longer connections to the TU-Delft server are possible, or if faster computers are available, the computational time will be less of a limiting factor. The model can also be made more efficient, by possibly increasing the pipe growth steps. If the pipe grows in depth with steps of d_{70} instead of $0.5 \cdot d_{70}$, less calculations are required for the pipe to reach its maximum length. This however decreases the precision of the model.

8.2.4. Implementation in a 3D model

The model developed for this research uses 2D geometries and equations. In real life, most BEP situations take place in 3D. 3D models are more conservative than 2D models, since the groundwater flow towards the pipe originates from all directions near the pipe. By implementing the new onset of motion criterion in a 3D model, the model comes closer to reality, hopefully resulting in more realistic critical heads.

8.2.5. Implementation of statistical analysis

The current model is able to find a deterministic critical hydraulic head for a certain cross-section. Multiple input parameters do however follow a certain probabilistic distribution which is now not taken into account. To do a full assessment of a dike and to determine its probability of failure, it is needed to also use stochastic input parameters. Important parameters to look into from a probabilistic perspective are the particle diameter (d_{70}), hydraulic conductivity (k), clay and silt fractions, anisotropy, soil particle and water volumetric densities (ρ) and the bedding angle. The probability of the critical hydraulic head to be significantly lower than the deterministic model predicts, is high when some of these parameters have high standard deviations.

8.2.6. Case study

Adding to the research recommendations, some recommendations to the local water authority are made on the safety of the Groningen sea dikes against backward erosion piping. The recommendations are focused on data collection and possible dike reinforcements. The current results imply that the dike is safe enough since the critical hydraulic head is larger than the design water level, but no actual probability of failure is determined due to the lack of using stochastic parameters.

Data collection

The parameters as used in the current model are based on extensive research on the sea dikes in Groningen. Some of the parameters are however not yet determined on all locations. This is the case for the silt and clay fractions, which have to be determined for the aquifer which is prone to BEP and not any other layer. Also the hydraulic conductivity of the foreshore is not known, while the foreshore is implemented in the model.

For the parameters which are present, also the standard deviations have to be used in the model to find a probability of failure. These can be found by analysing the sieve curves of relevant locations, the depth measurements of the foreshore, the thickness of the aquifer at different locations, and the anisotropy on different locations. A statistical approach will give insight in the actual safety of the dike.

Further measures against BEP

If the results of a stochastic assessment of the dike indicate the need of reinforcement, a measure has to be taken. The least expensive physical measure will be the filling of the inflow ditch and making sure that the whole foreland can act as a impermeable layer, lengthening the seepage path. This will at least double the seepage length and will likely result in the dike being assessed as safe.

References

- Aguilar-López, J., Warmink, J., Schielen, R., & Hulscher, S. (2016). Piping erosion safety assessment of flood defences founded over sewer pipes. *European Journal of Environmental and Civil Engineering*, 22(6), 707–735. <https://doi.org/10.1080/19648189.2016.1217793>
- Allan, R. J. (2018). Backward erosion piping. *PhD Thesis*.
- Bersan, S., Jommi, C., Koelewijn, A., & Simonini, P. (2013). Applicability of the fracture flow interface to the analysis of piping in granular material. *Excerpt from the Proceedings of the 2013 COMSOL Conference in Rotterdam*.
- Bligh, W. G. (1910). Dams, barrages and weirs on porous foundations. *Engineering Record*, 64(26), 708–710.
- Chang, D., & Zhang, L. (2013). Extended internal stability criteria for soils under seepage. *Soils and Foundations*, 53(3), 569–583. <https://doi.org/http://dx.doi.org/10.1016/j.sandf.2013.06.008>
- Clibborn, J., & Beresford, J. S. (1902). Experiments on the passage of water through sand. *Govt. of India, Central Printing Office*.
- Davis Jr., R. A., & Dalrymple, R. W. (2012). *Principles of tidal sedimentology* [ISBN 978-94-007-0122-9]. Springer.
- Deltares & Rijkswaterstaat Noord Nederland. (2025, March). *Waddenviewer- depth average flow velocity*. <https://viewer.openearth.nl/wadden-viewer/?folders=93790295,TdEAeLFfSy6ZuBkW2OX5Ow,93795238,154102245&layers=154102711&layerNames=Stroomsnelheid%20p50>
- Esri. (2024, October). *Esri satellite*. https://server.arcgisonline.com/ArcGIS/rest/services/World_Imagery/MapServer/tile/%7Bz%7D/%7By%7D/%7Bx%7D
- Furgo. (2022). *Onderzoek opdrukveiligheid asfaltbekleding primaire kering nabij de emmapolder*.
- Google. (2025, January). *Google earth*. <https://earth.google.com/web/>
- Griffith, W. (1914). The stability of weir foundations on sand and soil subject to hydrostatic pressure. *Institution of Civil Engineers*, 197, 221–232.
- Hanses, U. (1985). Zur mechanik der entwicklung von erosionskanälen in geschichtetem untergrund unter stauanlagen. *Ph.D. dissertation*.
- Hijma, M., Van der Kolk, B., Karaoulis, M., & Van Tilborg, R. (2021). Pipingproef vijfhuisterdijk - eindrapportage. *HWBP / Waterschap Hollandse Delta*.
- Hijma, M., Van Goor, G. R., De Bart, H., Pruijn, N., & Van Beek, V. M. (2023). Eindrapport piping in getijdenzand. *HWBP / Waterschap Hollandse Delta*.
- Hijma, M., Van Goor, G. R., Pruijn, N., Van Beek, V. M., & Wiersma, A. (2023). Analyserapport grootschalige pipingproeven hedwigepolder. *HWBP / Waterschap Hollandse Delta*.
- Hijma, M., Van Goor, G. R., Pruijn, N., Van Beek, V. M., Wopereis, L., & Wiersma, A. (2023). Analyse kleine en medium schaalproeven. *HWBP / Waterschap Hollandse Delta*.
- Lane, E. W. (1935). Security from under-seepage- masonry dams on earth foundations. *Transactions of ASCE*, 100(1), 1235–1272.
- Lucker, S., & Robbins, B. (2023). Backwards erosion piping through silty sand mixtures. *Symposium "Management for Safe Dams" - 91st Annual ICOLD Meeting*, 1825–1832.
- Methorst, A. (2020). Piping in sandy tidal deposits. *Master thesis TU Delft*.
- Miesel, D. (1978). Rückschreitende erosion unter bindiger deckschicht. *Baugrundtagung 1978*, 599–626.
- Mitchell, K. M., & Soga, K. (2005). *Fundamentals of soil behaviour* (3rd ed.). John Wiley Sons. Inc.
- Muller-Kirchenbauer, H. (1980). Zum zeitlichen verlauf der rückschreitenden erosion in geschichtetem untergrund unter dammen und stauanlagen. *Talsperrenbau und bauliche Probleme der Pumpspeicherwerke*, 43, 1–25.
- Noorderzijlvest. (2022a). Logboek stph dijktraject 6-6.
- Noorderzijlvest. (2022b). Waterveiligheidsbeoordeling dijktraject 6-6.
- Normalisatie-instituut, N. (1989). Geotechnics - classification of unconsolidated soil samples. *NEN 5104:1989 nl*.
- Pol, J. C. (2022). Time-dependent development of backward erosion piping. *PhD (TU Delft)*. <https://doi.org/https://doi.org/10.4233/uuid:eb5ed3b2-4210-489e-b329-59722a0c50a0>
- Pol, J. C., Kanning, W., Jonkman, S. N., & Kok, M. (2024). Time-dependent reliability analysis of flood defenses under cumulative internal erosion. *Structure and Infrastructure Engineering*. <https://doi.org/10.1080/15732479.2024.2416434>
- ResearchGate. (2025, February). *Hydrologic-process-based soil texture classifications for improved visualization of landscape function - scientific figure on researchgate*. https://www.researchgate.net/figure/USDA-Soil-Texture-Triangle_fig2_279631053
- Rijkswaterstaat. (2021, May). *Schematiseringshandleiding piping*.
- Rijkswaterstaat. (2023). *Kunstwerken, handleiding overstromingskansanalyse, groene versie*.
- Rijkswaterstaat. (April 2014). *Handreiking ontwerpen met overstromingskansen*.

- Robbins, B. A. (2022). Finite element modelling of backward erosion piping. *PhD Thesis*.
- Robbins, B. A., Montalvo-Bartolomei, A. M., & Griffiths, D. V. (2020). Analyses of backward erosion progression rates from small-scale flume experiments. *Journal of Geotechnical and Geoenvironmental Engineering*, 146. [https://doi.org/https://doi.org/10.1061/\(ASCE\)GT.1943-5606.0002338](https://doi.org/https://doi.org/10.1061/(ASCE)GT.1943-5606.0002338)
- Robbins, B. A., Van Beek, V. M., Lopez-Soto, J., Montalvo-Bartolomei, A. M., & Murphy, J. (2018). A novel laboratory test for backward erosion piping. *Int. J. Phys. Modell. Geotech.*, 18(5), 266–279. <https://doi.org/https://doi.org/10.1680/jphmg.17.00016>
- Robbins, B. A., Van Beek, V. M., Pol, J., & Griffiths, D. V. (2022). Errors in finite element analysis of backward erosion piping. *Geomechanics for Energy and the Environment*, 31. <https://doi.org/https://doi.org/10.1016/j.gete.2022.100331>
- Schmertmann, J. H. (1995). Report on flume tests for piping and scour erosion of hl-2 sands.
- Schmertmann, J. H. (2000). The no-filter factor of safety against piping through sands [American Society of Civil Engineers]. *Judgement and Innovation*, 65–133.
- Sellmeijer, J. B. (1988). On the mechanism of piping under impervious structures. *Ph.D. dissertation*.
- Sellmeijer, J. B. (2006). Numerical computation of seepage erosion below dams (piping). *Proceedings 3rd International Conference on Scour and Erosion (ICSE-3)*.
- Sellmeijer, J. B., Calle, E. O. F., & Sip, J. W. (1989). Influence of aquifer thickness on piping below dikes and dams [Copenhagen: ICOLD]. *Proceedings of international symposium on analytical evaluation of dam related problems*, 357–366.
- Sellmeijer, J. B., De la Cruz, J. L., Van Beek, V. M., & Knoeff, H. (2011). Fine-tuning of the backward erosion piping model through small-scale, medium-scale and ijdijk experiments. *European Journal of Environmental and Civil Engineering*, 15(8), 1139–1154. <https://doi.org/10.1080/19648189.2011.9714845>
- Sellmeijer, J. B., & Koenders, M. A. (1991). A mathematical model for piping. *Applied Mathematical Modelling*, 15(11-12), 646–651.
- Shields, A. (1936). Anwendung der ahnlichkeitsmechanik und turbulenzforschung auf die geschiebebewegung [In German]. *Mitteilungen der Preußischen Versuchsanstalt für Wasserbau und Schiffbau*.
- Silvis, F. (1991). Verificatie piping model: Proeven in de deltagoot -evaluatierapport. *Grondmechanica Delft*.
- Topotijdreis. (2025, January). *200 jaar topografische kaarten*. <https://www.topotijdreis.nl/>
- Townsend, F., Schmertmann, J., Logan, T., Pietrus, T., & Wong, Y. (1981). An analytical and experimental investigation of a quantitative theory for piping in sand. *Technical report, University of Florida*.
- Van Asselen, S., Hijma, M. P., & Kanning, W. (2019). Anisotropie in doorlatendheid: Een literatuuronderzoek naar anisotropie in doorlatendheid en de effecten hiervan op piping. *Deltares*.
- Van Beek, V. M. (2015). Backward erosion piping - initiation and progression. *PhD dissertation*.
- Van Beek, V. M., & Hoffmans, G. (2017). Evaluation of dutch backward erosion piping models and a future perspective. *25th Meeting of the European Working Group on Internal Erosion*.
- Van Beek, V. M., Knoeff, H., & Schweckendiek, T. (2011). Piping: Over 100 years of experience. *A FEELING FOR SOIL AND WATER – A TRIBUTE TO PROF. FRANS BARENDS*, 143–158.
- Van Beek, V. M., Knoeff, H., & Sellmeijer, H. (2011). Observations on the process of backward erosion piping in small-, medium- and full-scale experiments. *European Journal of Environmental and Civil Engineering*, 15(8), 1115–1137. <https://doi.org/10.1080/19648189.2011.9714844>
- Van Beek, V. M., Robbins, B., Rosenbrand, E., & Van Esch, J. (2022). 3d modelling of backward erosion piping experiments. *Geomechanics for Energy and the Environment*, 31.
- Van Beek, V. M., Robbins, B. A., Hoffmans, G. J. C. M., Bezuijen, A., & Van Rijn, L. C. (2019). Use of incipient motion data for backward erosion piping models. *International Journal of Sediment Research*, 34, 401–408. <https://doi.org/10.1016/j.ijsrc.2019.03.001>
- Van der Linde, E., Aguilar-Lopez, J., Wewer, M., Robbins, B., Colomes, O., & Jonkman, S. (n.d.). Numerical modelling of backward erosion piping: A literature review. *Graphical Abstract*.
- Van der Zee, R. (2011). Influence of sand characteristics on the piping process. *Master Thesis TU Delft*.
- Van Esch, J., Sellmeijer, J., & Stolle, D. (2013). Modeling transient groundwater flow and piping under dikes and dams.
- Vandenboer, K. (2019). A study on the mechanisms of backward erosion piping. *Ph.D. thesis, Ghent University*.
- Wewer, M., Aguilar-López, J. P., Kok, M., & Bogaard, T. (2021). A transient backward erosion piping model based on laminar flow transport equations. *Computers and Geotechnics*, 132. <https://doi.org/10.1016/j.compgeo.2020.103992>
- White, C. M. (1940). The equilibrium of grains on the bed of a stream. *Proceedings of the Royal Society*, 174, 322–338. <https://doi.org/10.1098/rspa.1940.0023>
- Wiertsema & Partners. (2018). Beoordeling primaire kering wbi 2017.
- Wit, J. M. D. (1984). Onderzoek zandmeevoerende wellen rapportage modelproeven. *Grondmechanica Delft report CO-220887/10*.

- Wooldridge, L. J., Worden, R. H., Griffiths, J., Utley, J. E. P., & Thompson, A. (2018). The origin of clay-coated sand grains and sediment heterogeneity in tidal flats. *Sedimentary Geology*, 373, 191–209. <https://doi.org/https://doi.org/10.1016/j.sedgeo.2018.06.004>
- Yokoi, H. (1968). Relationship between soil cohesion and shear strength. *Soil Science and Plant Nutrition*, 14(3), 89–93. <https://doi.org/10.1080/00380768.1968.10432750>

A

Python code: Onset of motion criterion fit

fitting_fines

June 10, 2025

```
[ ]: import numpy as np
import pandas as pd
import matplotlib.pyplot as plt
from scipy.optimize import curve_fit
from sklearn.model_selection import train_test_split
import os

[ ]: file_path = r"C:\Users\syitze\OneDrive - Delft University of
↳Technology\Q3_Thesis\Model\calibration_input2.csv"
calibration_data = pd.read_csv(file_path, delimiter=';')

# Define the directory to save figures
save_dir = r"C:\Users\syitze\OneDrive - Delft University of
↳Technology\Q3_Thesis\Afbeeldingen\Python"

# Extract fines data
fines = calibration_data['%fines'] # %

# Extract clay data
clay = calibration_data['%lutum'] # %

# Extract mud data
mud = calibration_data['%slib'] # %

# Extract sf data
sf = calibration_data['safety_factor'] # -

# Extract d70 data and unit conversion from mm to m
d70 = calibration_data['d70']/1000 # m

silt = fines-clay

names_exp = calibration_data['Experiment']

[3]: D = 3 # m
L = 15 # m
white=0.25 # -
```

```

gamma_p_eff=16.6 # kN/m3
gamma_w=10 # kN/m3
g=9.81 # m/s2
theta=37/180*np.pi # rad
k=5/24/60/60 # m/d
rho_w=1000 # kg/m3
dyn_visc=0.001 # Pa*s
kappa=k*dyn_visc/(rho_w*g) # m2
d70m=0.000208 # m

def F_g():
    return 0.91*(D/L)**(0.28/((D/L)**2.8-1)+0.04)

def F_r_basic():
    return white*gamma_p_eff/gamma_w*np.tan(theta)

def F_s(d70):
    return d70/((kappa*L)**(1/3))*(d70m/d70)**0.6

def sell(d70):
    return F_g()*F_r_basic()*F_s(d70)*L

```

```

[4]: filtered_indices = []
silt_max=20
clay_max=8
for i in range(len(fines)):
    if silt[i] < silt_max:
        if clay[i] < clay_max:
            filtered_indices.append(i)

# Convert to numpy array for indexing
filtered_indices = np.array(filtered_indices)

# Filter the arrays
fines = np.array(fines)[filtered_indices]
clay = np.array(clay)[filtered_indices]
sf = np.array(sf)[filtered_indices]
mud = np.array(mud)[filtered_indices]
silt = np.array(silt)[filtered_indices]
#rd=np.array(rd)[filtered_indices]
d70=np.array(d70)[filtered_indices]
names_exp=np.array(names_exp)[filtered_indices]

```

```

[5]: fg = F_g()
fs = F_s(d70)
fr_b = F_r_basic()

```

```

target_F_r = (sf*sell(d70)) / (fg * fs * fr_b * L)

train_indices, val_indices = train_test_split(
    range(len(silt)),
    test_size=0.2 , # 20% for validation
    random_state=42 # For reproducibility
)
sf_final_val=sf[val_indices]
sf = sf[train_indices]
clay_final_val=clay[val_indices]
clay = clay[train_indices]
d70_final_val=d70[val_indices]
d70 = d70[train_indices]
silt_final_val=silt[val_indices]
silt = silt[train_indices]
names_exp_final_val=names_exp[val_indices]
names_exp = names_exp[train_indices]

print(f'Experiment names: {names_exp}')
print(f'Silt % :{silt}')
print(f'clay % :{clay}')
print(f'd70 [m] :{d70}')
print(f'sf [-] :{sf}')

```

```

Experiment names: ['B146' 'MSP43_HWP3' 'HWP_264' 'GTZG_1_207' 'GTFZ_3_214'
'HWP_269'
'GTFZ_251' 'HWP_265' 'HWP_263' 'B15_3K' 'GTZG_2_208' 'GTZG_3_209'
'hedwige noord' 'GTFZ_2_214' 'B15_1K' 'hedwige zuid' 'HWP_271' 'Bms19'
'HWP_273' 'HWP_253' 'HWP_260' 'HWP_267' 'HWP_272' 'GTFZ_252']
Silt % :[ 0.   6.6 17.9  2.7 18.   8.3 11.9 17.9 14.4  0.6  2.7  2.7 10.7 18.
 0.2 10.7  7.9  0.  10.8  6.3 11.7 13.1 12.8 12.6]
clay % :[0.   2.3 7.5 2.2 1.   4.6 2.7 7.5 2.7 2.4 2.2 2.2 4.1 1.   0.8 4.1 3.6 0.
 4.9 4.5 1.4 6.9 6.7 2.1]
d70 [m] :[0.00015  0.000148 0.000131 0.00016  0.00013  0.00014  0.000118
0.000131
0.000122 0.000171 0.00016  0.00016  0.000138 0.00013  0.000171 0.000138
0.000139 0.00015  0.000149 0.000138 0.000127 0.000122 0.000118 0.000123]
sf [-] :[1.   1.3  5.2  2.4  2.3  1.5  2.3  4.7  1.4  3.3  1.9  1.7  1.4  2.6
 1.3  1.4  4.1  1.06 1.3  1.4  2.2  1.8  1.8  6.1 ]

```

```

[6]: print(f'Experiment names: {names_exp_final_val}')
print(f'Silt % :{silt_final_val}')
print(f'clay % :{clay_final_val}')
print(f'd70 [mm] :{d70_final_val}')
print(f'sf [-] :{sf_final_val}')

```

```

Experiment names: ['B145' 'HWP_268' 'MSP42_HWP2' 'HWP_270' 'HWP_254' 'HWP_256']

```

```

Silt % :[ 0.  11.  10.2  7.9  6.3  0.8]
clay % :[0.  6.9  4.4  3.6  4.5  1.8]
d70 [mm] :[0.00015  0.000115  0.000135  0.000139  0.000138  0.000171]
sf [-] :[1.  1.7  1.2  2.1  2.2  1.7]

```

```

[ ]: pad = 0.01 # set pad for plotting colorbars

# Define the slope n, Hc_actual and the full X array
n = silt_max / clay_max # Slope silt/clay
H_c_actual = sf * sell(d70)
X_full = np.column_stack((silt, clay, sf, d70))
target_safety = 95 #aimed % determined right

# Step 1: Define the polynomial model for sf
def polynomial_model(X, a, b, c, d):
    silt = X[:, 0]
    clay = X[:, 1]
    f_r=white*gamma_p_eff/gamma_w*np.tan(theta*(1+a*silt**c))+b*clay**d
    return f_r/fr_b

# Step 2: Define the lower fit polynomial model for sf
def polynomial_fit(X, a, b, c, d):
    silt = X[:, 0]
    clay = X[:, 1]
    sf = X[:, 2]
    array=[]
    for i in range(len(sf)):
        array=np.append(array,np.percentile(polynomial_model(X, a, b, c, d)-sf,
↳target_safety))
    return array

initial_guess_poly = [0.05, 0.1, 1, 1] # Use boundary parameters as initial
↳guess
bounds_poly = ([ 0,0, 0, 0], [np.inf, np.inf, np.inf,np.inf])

# Step 2.2 Fit the polynomial model to the full resampled dataset

zeros = np.zeros(len(silt))
X_boundary = np.column_stack((silt, clay, sf))

try:
    popt, pcov = curve_fit(
        polynomial_fit,
        X_boundary,
        zeros,
        p0=initial_guess_poly,
        bounds=bounds_poly,

```

```

        maxfev=10000
    )
    a, b, c, d = popt

except RuntimeError as e:
    print(f"Fit {i+1} (polynomial) failed: {e}")
    a, b, c, d = initial_guess_poly
    pcov = np.zeros((4, 4))

# Compute sf for the entire dataset using the fitted parameters
sf_fitted_unscaled = polynomial_model(X_full, a, b, c, d)

# Analyze the variance in the fitted parameters
param_stats = {
    'a': {'value': a},
    'b': {'value': b},
    'c': {'value': c},
    'd': {'value': d}
}
print(param_stats)

# Step 3: Define the final scaled sf_fitted function (updated to handle array/
↳ scalar inputs)
def sf_fitted(silt, clay):
    # Convert inputs to numpy arrays
    silt = np.atleast_1d(silt)
    clay = np.atleast_1d(clay)
    # Broadcast scalars to match the shape of the other input
    if silt.size == 1 and clay.size > 1:
        silt = np.full_like(clay, silt.item())
    elif clay.size == 1 and silt.size > 1:
        clay = np.full_like(silt, clay.item())
    elif silt.shape != clay.shape:
        raise ValueError(f"silt and clay shapes are incompatible: {silt.shape}↳
↳vs {clay.shape}")
    # Compute sf using the mean parameters from the bootstrap
    X = np.column_stack((silt, clay))
    sf = polynomial_model(X, a, b, c, d)
    return sf

# Compute sf_fitted for the entire dataset
sf_fitted_full = sf_fitted(silt, clay)
sf_fitted_val = sf_fitted(silt_final_val, clay_final_val)

def F_r_fitted_calibrated(silt, clay):
    sf = sf_fitted(silt, clay)

```

```

fr_basic = F_r_basic()
result = sf * fr_basic
#Ensure result is a scalar or matches the input shape
if not np.isscalar(result):
    if isinstance(result, (list, np.ndarray)):
        if result.size == 1:
            result = result.item()
        elif result.shape != (len(np.atleast_1d(silt)),):
            raise ValueError(f"F_r_fitted_calibrated output shape {result.
↪shape} does not match input shape")
    else:
        raise ValueError(f"F_r_fitted_calibrated should return a scalar or ↪
↪array, but got {type(result)}")
    return result

# Step 4: Update the Sellmeijer equation with the calibrated F_r
def sell2_calibrated(d70, silt=0, clay=0):
    H_c = F_g() * F_r_fitted_calibrated(silt, clay) * F_s(d70) * L
    # Ensure H_c is a scalar or matches the input shape
    if not np.isscalar(H_c):
        if isinstance(H_c, (list, np.ndarray)):
            if H_c.size == 1:
                H_c = H_c.item()
            elif H_c.shape != (len(np.atleast_1d(d70)),):
                raise ValueError(f"H_c output shape {H_c.shape} does not match ↪
↪input shape")
        else:
            raise ValueError(f"H_c should be a scalar or array, but got ↪
↪{type(H_c)}")
    return max(H_c, 0) if np.isscalar(H_c) else np.maximum(H_c, 0)

# Step 5: Generate 5000 random samples for %silt, %clay, and d70 with positive ↪
↪correlation
np.random.seed()
n_samples = 5000
random_clay = np.random.uniform(0, silt_max/n, n_samples)
random_silt = np.clip(n * random_clay + np.random.normal(0, 5, n_samples), 0, ↪
↪silt_max)
random_d70 = np.random.uniform(min(d70), max(d70), n_samples)

# Step 6: Compute calibrated H_c values for random samples
sf_values = sf_fitted(random_silt, random_clay)
fr_basic = F_r_basic()
F_r_values = sf_values * fr_basic
F_s_values = np.array([F_s(d) for d in random_d70])
H_c_calibrated_random = fg * F_r_values * F_s_values * L

```

```

# Compute H_c_calibrated for the entire dataset
F_r_values_full = sf_fitted_full * fr_basic
F_s_values_full = np.array([F_s(d) for d in d70])
H_c_calibrated = fg * F_r_values_full * F_s_values_full * L

F_r_values_val = sf_fitted_val * fr_basic
F_s_values_val = np.array([F_s(d) for d in d70_final_val])
H_c_calibrated_val = fg * F_r_values_val * F_s_values_val * L

# Step 7: Compute sf values for the entire dataset and random samples
sf_actual_full = H_c_actual / sell(d70)
sf_fitted_rand = H_c_calibrated_random / np.array([sell(d) for d in random_d70])

# Step 8: Plotting functions with enhanced labels, finer grid, and horizontal
↳ lines

# H_c vs %clay
plt.figure(figsize=(6, 6))
scatter1 = plt.scatter(random_clay, H_c_calibrated_random, c=random_silt,
↳ cmap='autumn', label='Random Samples', alpha=0.7, s=100)
scatter2=plt.scatter(clay, H_c_calibrated, c=silt, cmap='cool', marker='^',
↳ label='Calibrated', alpha=0.7, s=100)
scatter3=plt.scatter(clay_final_val, H_c_calibrated_val, c=silt_final_val,
↳ cmap='cool', marker='v', label='Validation', alpha=0.7, s=100)
plt.scatter(clay, sell(d70), marker='x', color='green', label='Sellmeijer
↳ 2011', alpha=0.7, s=100)
plt.scatter(clay, (sf * sell(d70)), marker='+', color='black', label='H_c
↳ Actual', alpha=0.7, s=100)
plt.scatter(clay_final_val, (sf_final_val * sell(d70_final_val)), marker='1',
↳ color='black', label='H_c validation', alpha=0.7, s=100)

plt.colorbar(scatter1, pad=pad,label='%silt')
plt.colorbar(scatter2, pad=pad,label='%silt')
plt.xlabel('%clay', fontsize=12)
plt.ylabel('Calibrated H_c (m)', fontsize=12)
plt.title('Calibrated H_c vs %clay (Color: %silt)', fontsize=14, pad=15)
plt.grid(True, which='both', linestyle='--', alpha=0.7)
plt.minorticks_on()
for hc in range(1, 9):
    plt.axhline(y=hc, color='gray', linestyle='--', alpha=0.5)
plt.legend(fontsize=10)
plt.ylim(0, clay_max)
plt.ylim(2, 8)
plt.tight_layout()

```

```

plt.savefig(os.path.join(save_dir, 'H_c_vs_clay.png'), dpi=300,
    ↳bbox_inches='tight')
plt.show()

# H_c vs %silt
plt.figure(figsize=(6, 6))
scatter1 = plt.scatter(random_silt, H_c_calibrated_random, c=random_clay,
    ↳cmap='autumn', label='Random Samples', alpha=0.7, s=100)
scatter2=plt.scatter(silt, H_c_calibrated, c=clay, cmap='cool', marker='^',
    ↳label='Calibrated', alpha=0.7, s=100)
scatter3=plt.scatter(silt_final_val, H_c_calibrated_val, c=clay_final_val,
    ↳cmap='cool', marker='v', label='Validation', alpha=0.7, s=100)
plt.scatter(silt, sell(d70), marker='x', color='green', label='Sellmeijer
    ↳2011', alpha=0.7, s=100)
plt.scatter(silt, (sf * sell(d70)), marker='+', color='black', label='H_c
    ↳Actual', alpha=0.7, s=100)
plt.scatter(silt_final_val, (sf_final_val * sell(d70_final_val)), marker='1',
    ↳color='black', label='H_c validation', alpha=0.7, s=100)

plt.colorbar(scatter1, pad=pad, label='%clay')
plt.colorbar(scatter2, pad=pad, label='%clay')
plt.xlabel('%silt', fontsize=12)
plt.ylabel('Calibrated H_c (m)', fontsize=12)
plt.title('Calibrated H_c vs %silt (Color: %clay)', fontsize=14, pad=15)
plt.grid(True, which='both', linestyle='--', alpha=0.7)
plt.minorticks_on()
for hc in range(1, 9):
    plt.axhline(y=hc, color='gray', linestyle='--', alpha=0.5)
plt.legend(fontsize=10)
plt.ylim(2, 8)
plt.xlim(0, silt_max)
plt.tight_layout()
plt.savefig(os.path.join(save_dir, 'H_c_vs_silt.png'), dpi=300,
    ↳bbox_inches='tight')
plt.show()

# sf vs %clay
plt.figure(figsize=(6, 6))
scatter1 = plt.scatter(random_clay, sf_fitted_rand, c=random_silt,
    ↳cmap='autumn', label='Random Samples', alpha=0.7, s=100, zorder=1)
scatter2=plt.scatter(clay, sf_fitted_full, c=silt, cmap='cool', marker='^',
    ↳label='Fitted', alpha=0.7, s=100, zorder=2)
scatter2=plt.scatter(clay_final_val, sf_fitted_val, c=silt_final_val,
    ↳cmap='cool', marker='v', label='Validation', alpha=0.7, s=100, zorder=2)
plt.scatter(clay, sf, marker='+', color='black', label='sf Actual', alpha=0.7,
    ↳s=100, zorder=3)

```

```

plt.scatter(clay_final_val, sf_final_val, marker='1', color='black', label='sf_
↳validation', alpha=0.7, s=100, zorder=3)

plt.colorbar(scatter1, pad=pad, label='%silt')
plt.colorbar(scatter2, pad=pad, label='%silt')
plt.xlabel('%clay', fontsize=12)
plt.ylabel('Strength Factor (sf)', fontsize=12)
plt.title('Strength Factor (sf) vs %clay (Color: %silt)', fontsize=14, pad=15)
plt.grid(True, which='both', linestyle='--', alpha=0.7)
plt.minorticks_on()
for sf_value in range(1, 9):
    plt.axhline(y=sf_value, color='gray', linestyle='--', alpha=0.5)
plt.legend(fontsize=10)
plt.ylim(1, 7)
plt.xlim(0, clay_max)
plt.tight_layout()
plt.savefig(os.path.join(save_dir, 'sf_vs_lutum.png'), dpi=300,
↳bbox_inches='tight')
plt.show()

# sf vs %silt
plt.figure(figsize=(6, 6))
scatter1 = plt.scatter(random_silt, sf_fitted_rand, c=random_clay,
↳cmap='autumn', label='Random Samples', alpha=0.7, s=100, zorder=1)
scatter2=plt.scatter(silt, sf_fitted_full, c=clay, cmap='cool', marker='^',
↳label='Fitted (All Data)', alpha=0.7, s=100, zorder=2)
scatter2=plt.scatter(silt_final_val, sf_fitted_val, c=clay_final_val,
↳cmap='cool', marker='v', label='Fitted (All Data)', alpha=0.7, s=100,
↳zorder=2)
plt.scatter(silt, sf, marker='+', color='black', label='sf Actual', alpha=0.7,
↳s=100, zorder=3)
plt.scatter(silt_final_val, sf_final_val, marker='1', color='black', label='sf_
↳validation', alpha=0.7, s=100, zorder=3)

plt.colorbar(scatter1, pad=pad, label='%clay')
plt.colorbar(scatter2, pad=pad, label='%clay')
plt.xlabel('%silt', fontsize=12)
plt.ylabel('Strength Factor (sf)', fontsize=12)
plt.title('Strength Factor (sf) vs %silt (Color: %clay)', fontsize=14, pad=15)
plt.grid(True, which='both', linestyle='--', alpha=0.7)
plt.minorticks_on()
for sf_value in range(1, 9):
    plt.axhline(y=sf_value, color='gray', linestyle='--', alpha=0.5)
plt.legend(fontsize=10)
plt.ylim(1, 7)
plt.xlim(0, silt_max)

```

```

plt.tight_layout()
plt.savefig(os.path.join(save_dir, 'sf_vs_silt.png'), dpi=300,
    ↳bbox_inches='tight')
plt.show()

# New Plot 1: sf vs %silt with lines for different %clay values (0% to 8%)
plt.figure(figsize=(6, 6))

# Define the range of %silt values to plot
silt_range = np.linspace(0, silt_max, 100) # Use 100 points for smoother lines

# Define %clay values from 0% to 8%
clay_values = np.arange(0, 10, 2) # 0%, 1%, ..., 8%

# Define colors for the lines (consistent with previous plots)
colors = ['blue', 'cyan', 'green', 'lime', 'orange', 'red', 'magenta',
    ↳'purple', 'black']

# Plot a line for each %clay value
for i, clay_val in enumerate(clay_values):
    # Compute sf for the current %clay value across the silt range (vectorized)
    sf_values = sf_fitted(silt_range, clay_val)
    plt.plot(silt_range, sf_values, label=f'%clay = {clay_val}%', linewidth=2,
    ↳color=colors[i])

plt.xlabel('%silt', fontsize=12)
plt.ylabel('Strength Factor (sf)', fontsize=12)
plt.title('Strength Factor (sf) vs %silt for Different %clay Values',
    ↳fontsize=14, pad=15)
plt.grid(True, which='both', linestyle='--', alpha=0.7)
plt.minorticks_on()
for sf_value in np.arange(0.5, 3.5, 0.5): # Adjusted to match y-axis range
    plt.axhline(y=sf_value, color='gray', linestyle='--', alpha=0.5)
plt.legend(fontsize=10, title='%clay')
plt.ylim(1, 1.75) # As specified
plt.xlim(0, silt_max) # Ensure x-axis matches silt range
plt.tight_layout()
plt.savefig(os.path.join(save_dir, 'sf_lines_vs_silt.png'), dpi=300,
    ↳bbox_inches='tight')
plt.show()

# New Plot 2: sf vs %clay with lines for different %silt values (0% to 18%)
plt.figure(figsize=(6, 6))

# Define the range of %clay values to plot
# Use clay_max if defined, otherwise use 8 as the maximum %clay
try:

```

```

    clay_range = np.linspace(0, clay_max, 100) # From 0 to clay_max, 100 points
except NameError:
    clay_range = np.linspace(0, 8, 100) # Default to 8 if clay_max is not
    ↪defined

# Define %silt values from 0% to 18% in steps of 2
silt_values = np.arange(0, 21, 4) # 0%, 2%, ..., 18%

# Define colors for the lines
colors = ['blue', 'cyan', 'green', 'lime', 'orange', 'red', 'magenta',
    ↪'purple', 'black', 'gray']

# Plot a line for each %silt value
for i, silt_val in enumerate(silt_values):
    # Compute sf for the current %silt value across the clay range
    sf_values = sf_fitted(silt_val, clay_range)
    plt.plot(clay_range, sf_values, label=f'%silt = {silt_val}%', linewidth=2,
    ↪color=colors[i])

plt.xlabel('%clay', fontsize=12)
plt.ylabel('Strength Factor (sf)', fontsize=12)
plt.title('Strength Factor (sf) vs %clay for Different %silt Values',
    ↪fontsize=14, pad=15)
plt.grid(True, which='both', linestyle='--', alpha=0.7)
plt.minorticks_on()
for sf_value in np.arange(0.5, 2.5, 0.25):
    plt.axhline(y=sf_value, color='gray', linestyle='--', alpha=0.5)
plt.legend(fontsize=10, title='%silt')
plt.ylim(1, 1.75) # Adjusted to match your desired range
plt.xlim(0, clay_max) # Adjusted to match %clay range
plt.tight_layout()
plt.savefig(os.path.join(save_dir, 'sf_lines_vs_lutum.png'), dpi=300,
    ↪bbox_inches='tight')
plt.show()

# Step 9: Calculate and print the correlation coefficient
correlation = np.corrcoef(random_silt, random_clay)[0, 1]
print(f"Correlation coefficient between %silt and %clay: {correlation:.4f}")

# Step 10: Compute and print F_r_fitted(7, 5) / F_r_basic
fr_ratio = F_r_fitted_calibrated(7, 5) / F_r_basic()
print(f"F_r_fitted_calibrated(7, 5) / F_r_basic(): {fr_ratio:.4f}")

# Step 11: Test the sf_fitted function
sf_example = sf_fitted(np.array([7]), np.array([5]))
print(f"Example: sf_fitted(clay=7, silt=5) = {sf_example.item():.4f}")

```

```

# Step 12: Evaluate conservative prediction using the entire dataset
below_prediction = np.sum(H_c_actual < H_c_calibrated)
total_points = len(H_c_actual)
percentage_below = (below_prediction / total_points) * 100
print(f"Number of actual H_c values below predicted H_c: {below_prediction}/
↪{total_points}")
print(f"Percentage of actual H_c values below predicted H_c: {percentage_below:.
↪2f}% (targeted at {100-target_safety:.2f}%)")

# Step 13: Test sf_fitted(7, 10)
sf_test = sf_fitted(np.array([7]), np.array([10]))
print(f"sf_fitted(clay=7, silt=10) = {sf_test.item():.4f}")

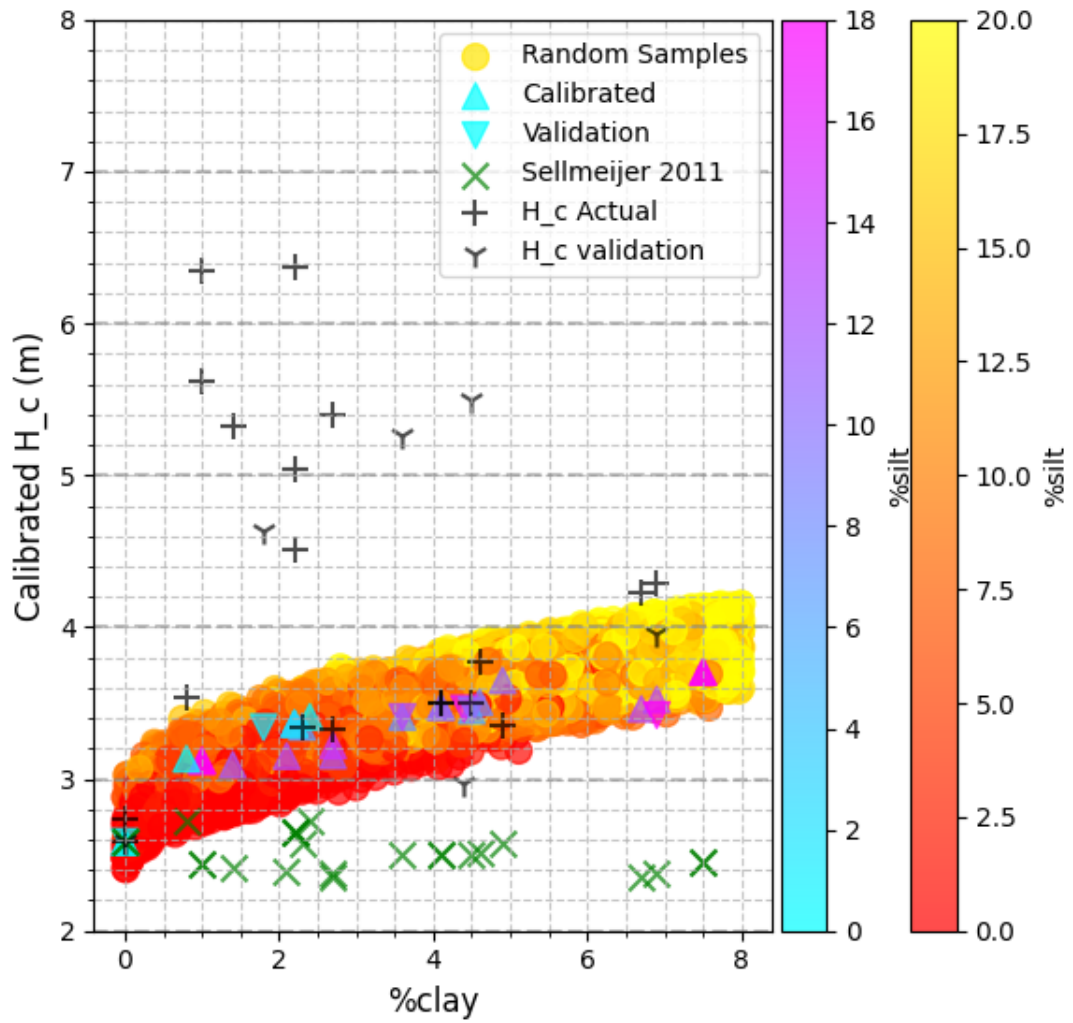
```

```

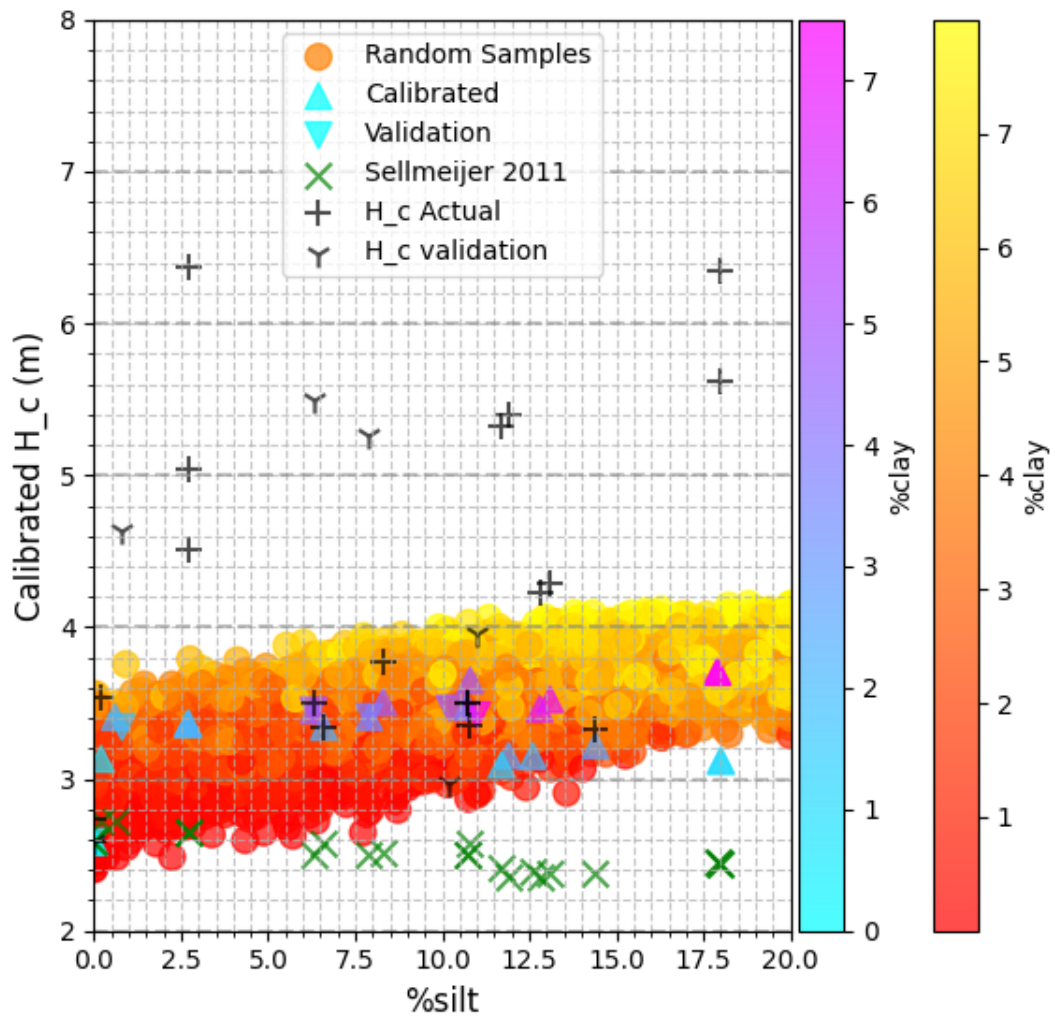
{'a': {'value': np.float64(0.02343992309249021)}, 'b': {'value':
np.float64(0.046879846184980374)}, 'c': {'value':
np.float64(0.4687984618498039)}, 'd': {'value': np.float64(0.468798461849804)}}

```

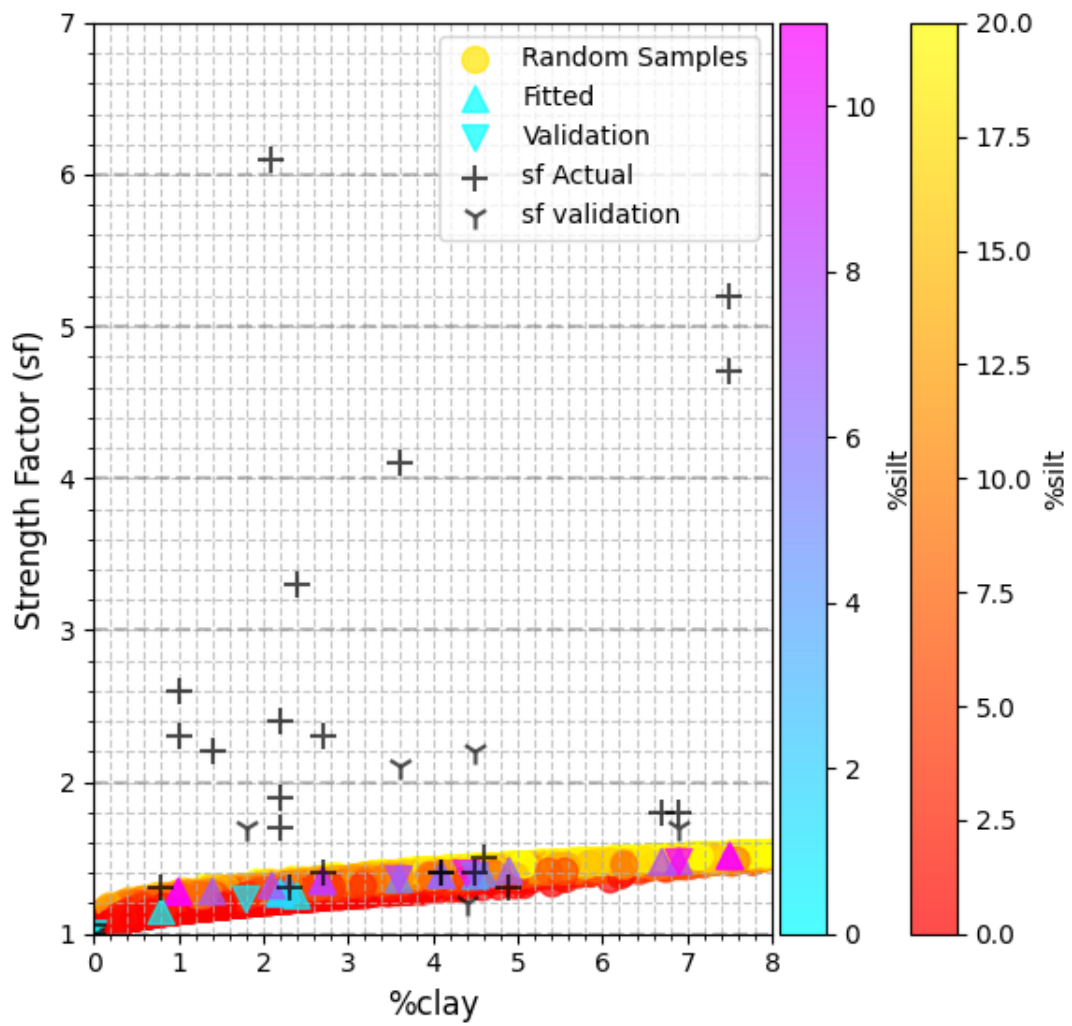
Calibrated H_c vs %clay (Color: %silt)



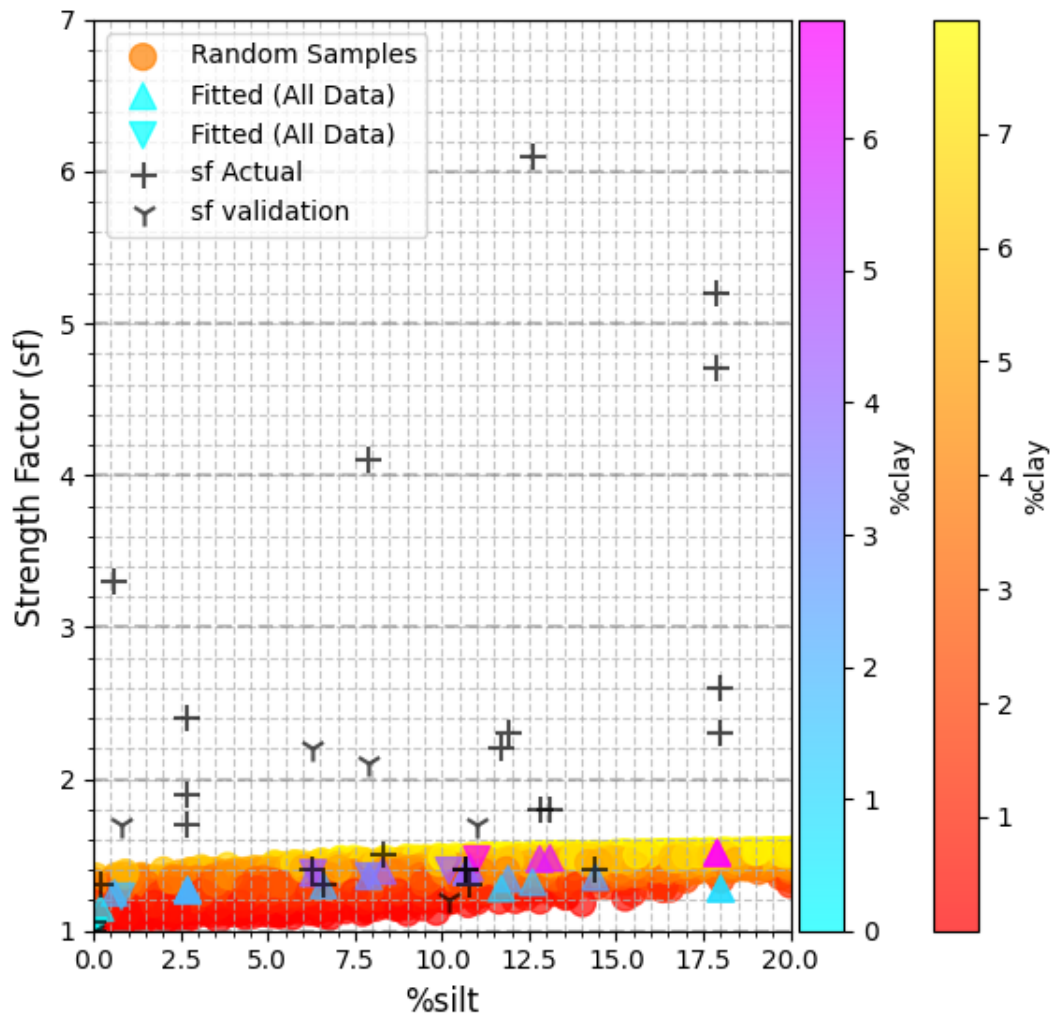
Calibrated H_c vs %silt (Color: %clay)



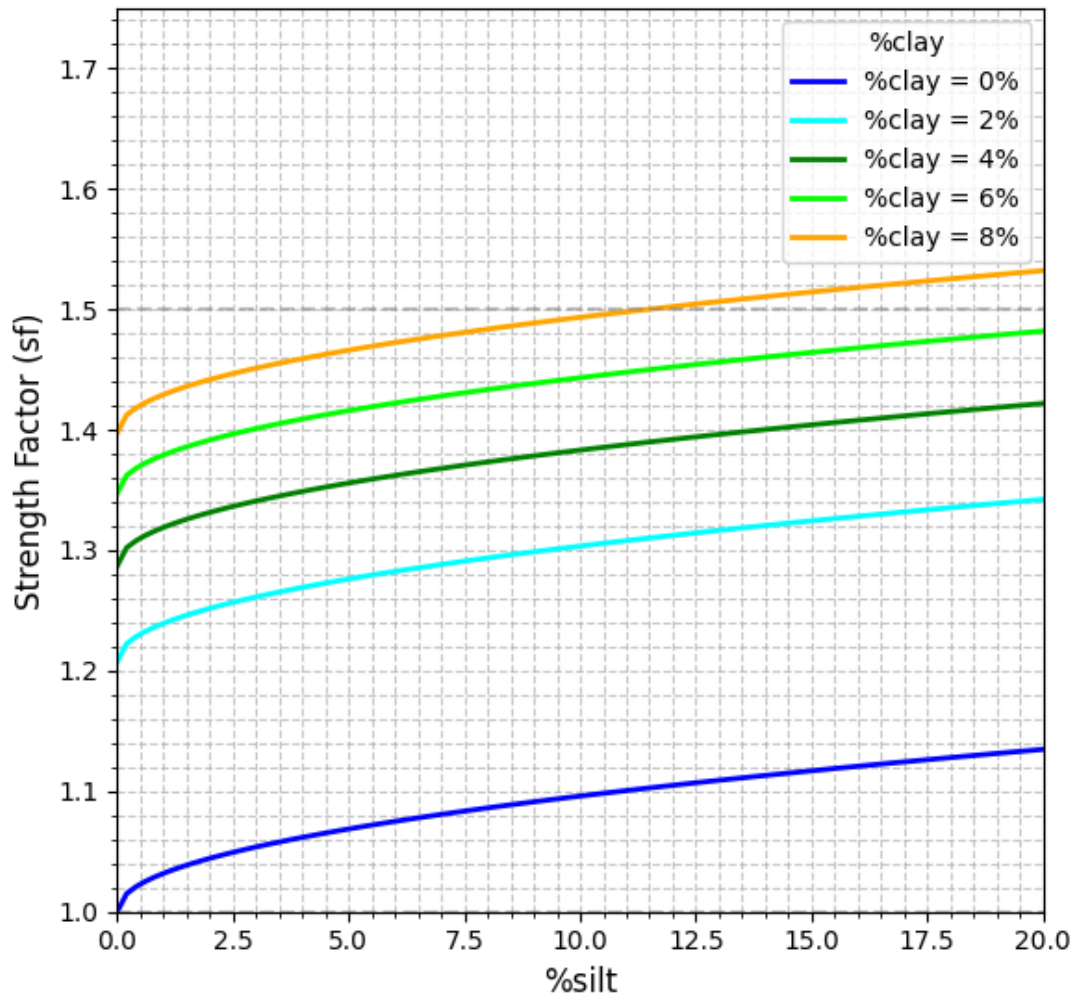
Strength Factor (sf) vs %clay (Color: %silt)



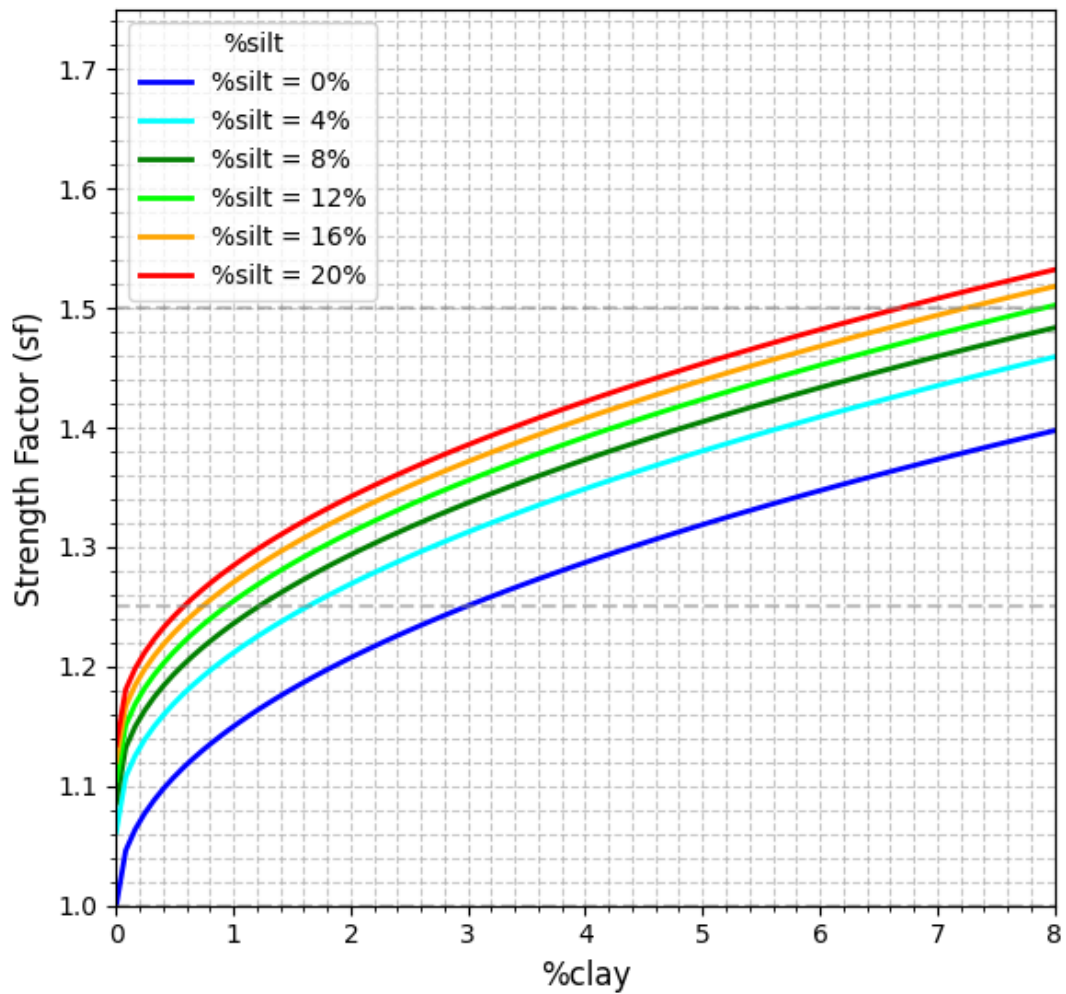
Strength Factor (sf) vs %silt (Color: %clay)



Strength Factor (sf) vs %silt for Different %clay Values



Strength Factor (sf) vs %clay for Different %silt Values



Correlation coefficient between %silt and %clay: 0.7624

$F_{r_fitted_calibrated}(7, 5) / F_{r_basic}()$: 1.3995

Example: $sf_{fitted}(clay=7, silt=5) = 1.3995$

Number of actual H_c values below predicted H_c : 2/24

Percentage of actual H_c values below predicted H_c : 8.33% (targeted at 5.00%)

$sf_{fitted}(clay=7, silt=10) = 1.5219$

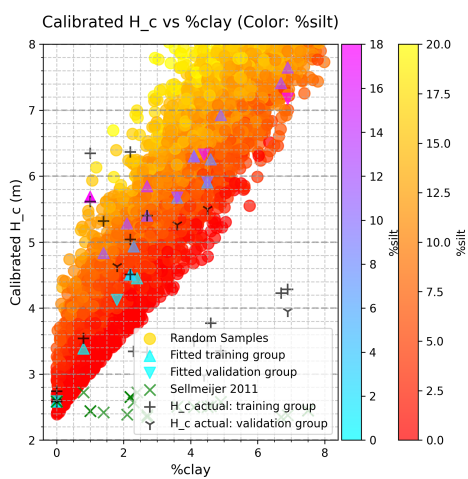
Other fits for onset of motion criterion

B.1. 50% percentile fit

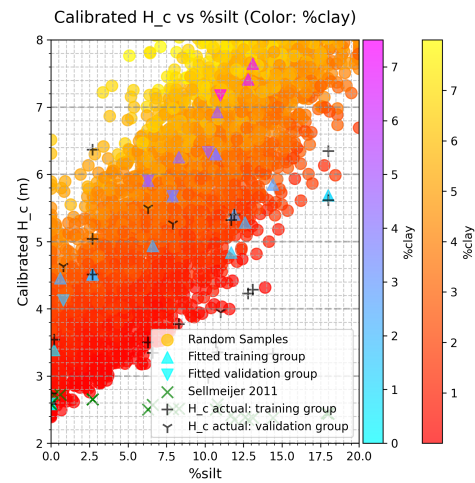
Different fits of new parameters inside the adapted onset motion criterion are looked into. In Chapter 3 the final fit is chosen to have a 95% certainty of under predicting the critical head. Eq. B.1 is the result of a fit with a 50% certainty of under predicting the critical head.

$$\tau_c = \eta \frac{\pi}{6} \rho' g d_x \tan(\theta \cdot (1 + 0.044 \cdot \%_{silt}^{0.87})) + (0.087 \cdot \%_{clay}^{0.87}) \tag{B.1}$$

Plots of the influence of this adapted fit are shown in Figure B.1, B.2 and B.3. This fit results in larger strength factors and higher exponential dependencies than the conservative fit. The critical head of many experiments would have been overestimated, possibly resulting in a higher probability of failure of a dike if this would be used in practice. The dependencies of the strength factor on clay and silt now show more linear and even exponential behaviour than the rooted behaviour as found for the more conservative fit. This is due to some of the experiments with high silt and clay to have resulted in relatively low strength factors. The conservative fit tries to stay below these strength factors and therefore stops increasing in strength factor rapidly.

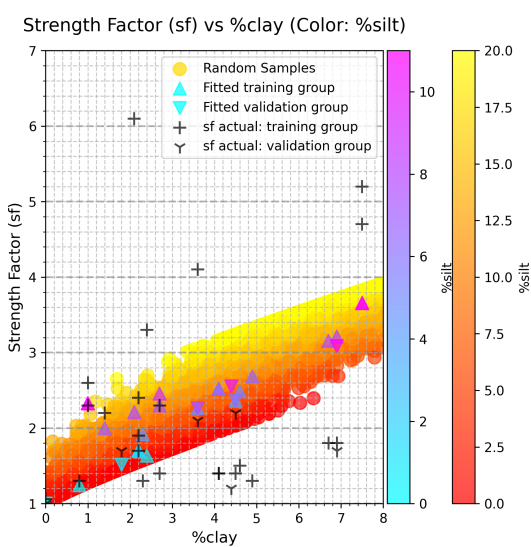


(a) Plot of %clay versus critical head with experiment results

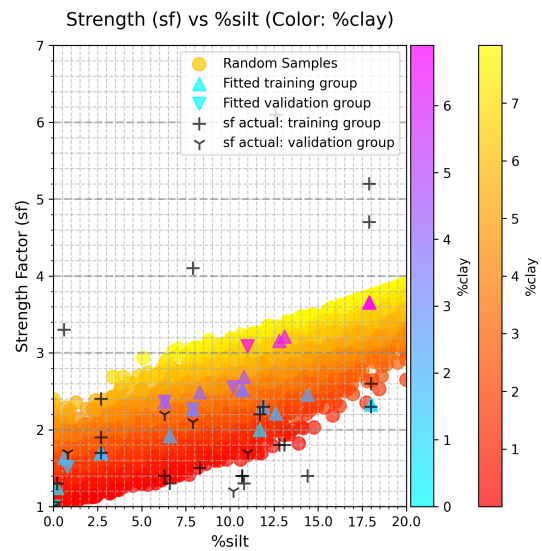


(b) Plot of %silt versus critical head with experiment results

Figure B.1: Plots of critical head with experimental- and predicted results (50% conservative)



(a) Plot of %clay versus strength factor with experiment results



(b) Plot of %silt versus strength factor with experiment results

Figure B.2: Plots of strength factor with experimental- and predicted results (50% conservative)

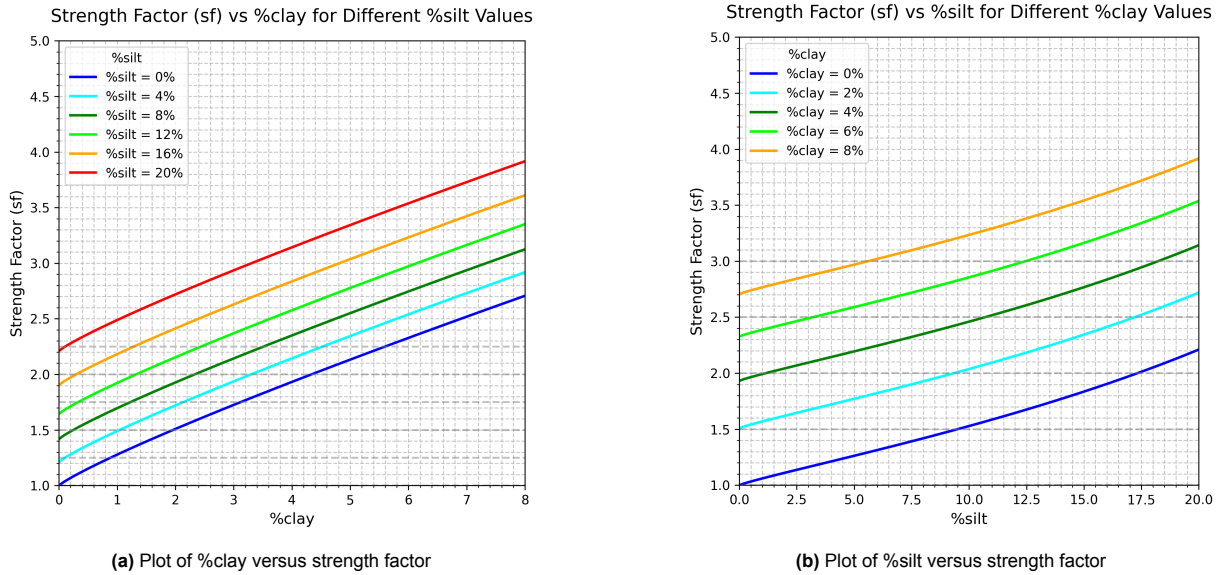


Figure B.3: Plots of the influence on silt- and clay fractions on the strength factor (50% conservative)

B.2. 95% fit on mud and fines

Not only the amount of under prediction can be changed, but also the variables inside the onset of motion criterion can be adapted. Eq. B.2 shows a new onset of motion criterion which is dependent on mud and fines. Mud is defined as all particles smaller than 16 μm . This onset of motion criterion based on mud and fines is not theoretically backed, but Deltares has observed that the mud fraction is an important predictor for the added safety against backward erosion piping.

$$\tau_c = \eta \frac{\pi}{6} \rho' g d_x \tan(\theta \cdot (1 + 0.014 \cdot \%_{fines}^{0.28})) + (0.028 \cdot \%_{mud}^{0.28}) \tag{B.2}$$

This equation however leads to extremely low strength factors. The influence of this onset of motion criterion on the critical head and strength factor can be found in Figure B.4, B.5 and B.6.

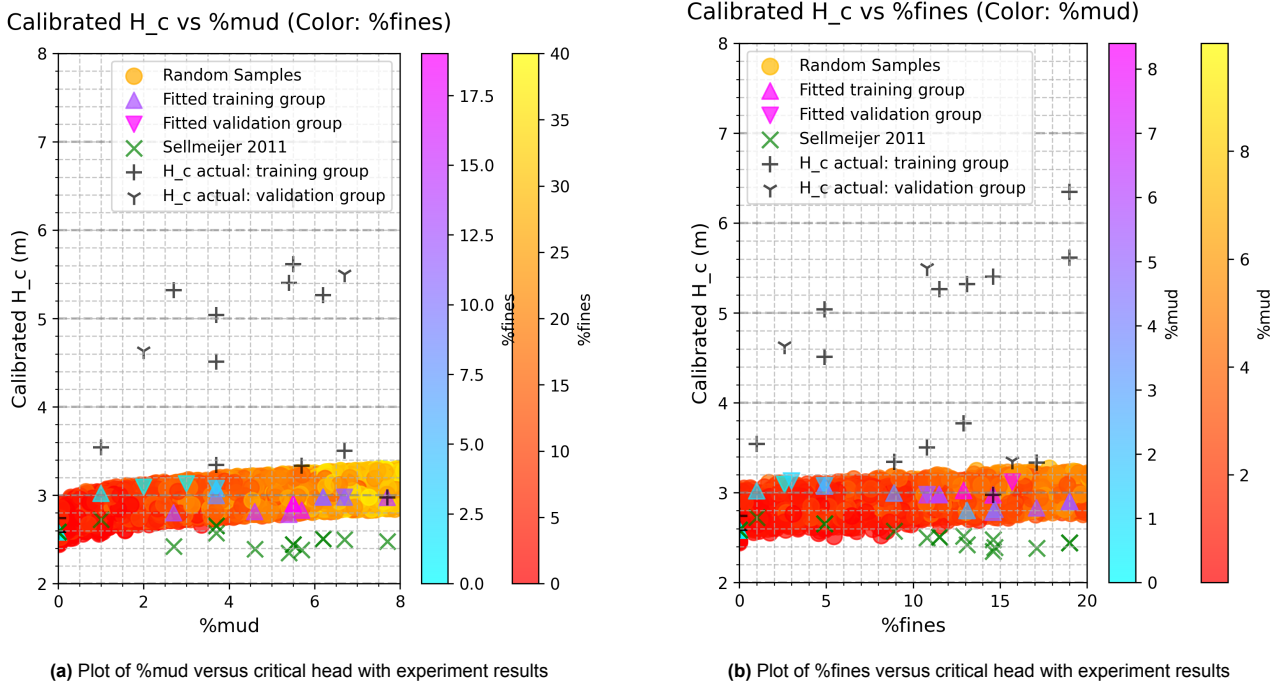
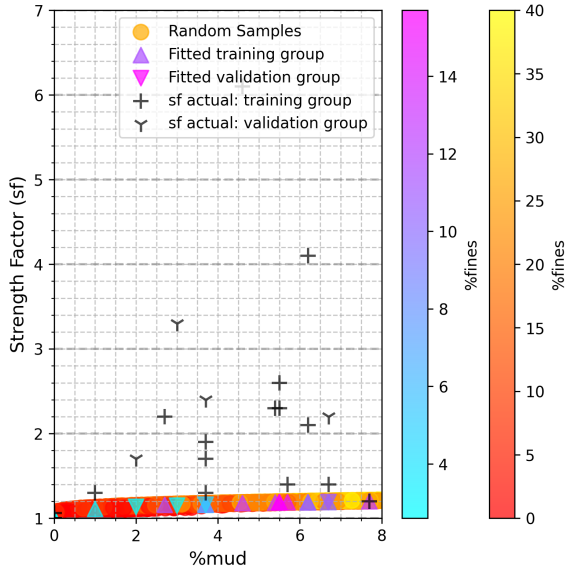


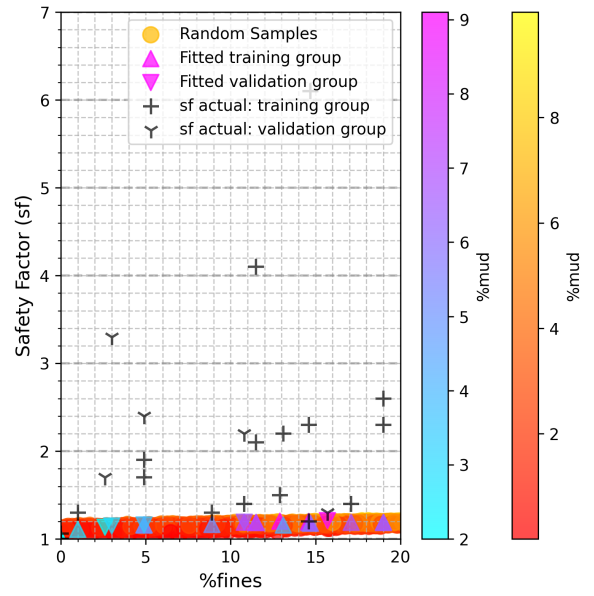
Figure B.4: Plots of critical head with experimental- and predicted results for mud and fines (95% conservative)

Strength Factor (sf) vs %mud (Color: %fines)



(a) Plot of %mud versus strength factor with experiment results

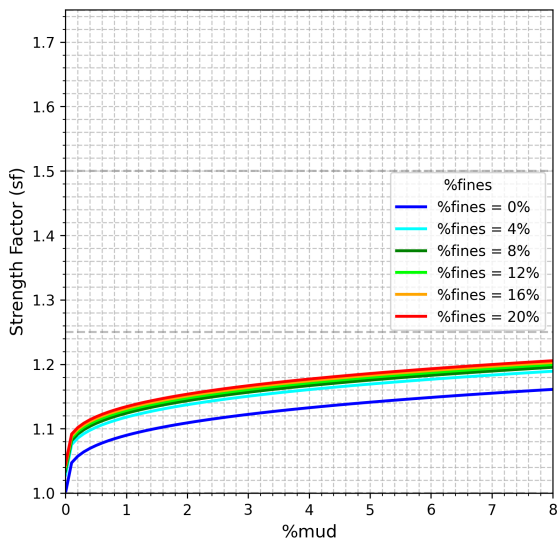
Safety Factor (sf) vs %fines (Color: %mud)



(b) Plot of %fines versus strength factor with experiment results

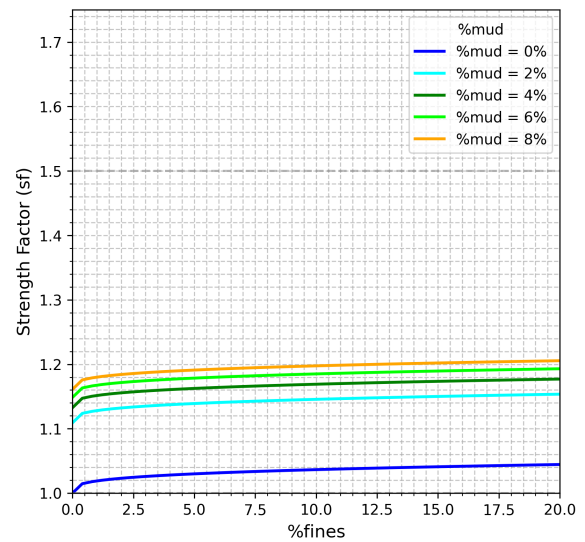
Figure B.5: Plots of strength factor with experimental- and predicted results for mud and fines (50% conservative)

Strength Factor (sf) vs %mud for Different %fines Values



(a) Plot of %mud versus strength factor

Strength Factor (sf) vs %fines for Different %mud Values



(b) Plot of %fines versus strength factor

Figure B.6: Plots of the influence on fines- and mud fractions on the strength factor (95% conservative)

C

Python code: run COMSOL for contour plot

Model_COMSOL_contourplot6021_B

May 30, 2025

Determine head

```
[ ]: #CMD commands to start COMSOL server:

#cd "C:\Program Files (x86)\COMSOL62\Multiphysics\bin\win64"
#comsolmphserver.exe

[ ]: import numpy as np
import matplotlib.pyplot as plt
import mph
import time
import pandas as pd
import os

[ ]: # Connect to the server
client = mph.Client(port=2036)
model = client.load(r"C:\Users\sytze\OneDrive - Delft University of
↳Technology\Q3_Thesis\Model\Model_section6021_week14.mph")
sweep_file_path = r"C:\Users\sytze\OneDrive - Delft University of
↳Technology\Q3_Thesis\Model\sweep.txt"

#Create list of to be observed critical heads
sweep_values_list = np.linspace(7,13.5,66)

#Create to be observed silt and clay (lutum) values
silt_array = np.linspace(0,20,4)
lutum_array = np.linspace(0,8,4)

#Set empty array to store results
H_c_array = np.zeros((len(silt_array),len(lutum_array)))

#Set basic values
model.parameter('d70', '0.1326 [mm]')
model.parameter('k_sand', '8 [m/d]')
model.parameter('c_an', '1')

#Run through model and find results
for j in range(len(silt_array)):
```

```

for z in range(len(lutum_array)):
    model.parameter('per_silt', f'{silt_array[j]}')
    model.parameter('per_lutum', f'{lutum_array[z]}')
    try:
        ↵
↪print('-----')
        print(f'silt: {silt_array[j]}|lutum: {lutum_array[z]}')

        # Debug all studies to find correct tags
        print("Available studies:")
        study_sequence = model.java.study() # Get the study sequence
        for i, study in enumerate(study_sequence):
            try:
                ↵
↪A'
                study_name = study.name() if hasattr(study, 'name') else 'N/'

                except Exception as e:
                    study_name = f"Error retrieving name: {e}"
                    print(f"Study {i}: tag={study.tag()}, name={study_name}")

            # Access the study sequence and find std1
            study1_node = None
            for i, study in enumerate(study_sequence):
                if study.tag() == "std1":
                    study1_node = study
                    print(f"Found Study 1 with tag: {study.tag()}")
                    break

            if study1_node:
                # Debug all features under std1
                print("Features under Study 1:")
                features = study1_node.feature()
                for feature in features:
                    print(f"Feature tag: {feature.tag()}")

            # Iterate through sweep values until H_c indicates erosion ↵
↪(non-zero)
            critical_h_left = None
            initial_guess_1 = H_c_array[j,z-1]
            initial_guess_2 = H_c_array[j-1,z]
            initial_guess_3 = 8
            initial_guess = np.max(np.array((initial_guess_1, ↵
↪initial_guess_2, initial_guess_3)))
            sweep_values_list = np.
↪linspace(initial_guess, initial_guess+5, 51)

            for value in sweep_values_list:
                try:

```

```

# Set the parameter for this iteration
model.parameter('H_left', str(value) + '[m]')
print(f"Attempting to solve Study 1 with H_left = {value} m")

# Solve the study
study1_node.run()
print(f"Study 1 completed for H_left = {value} m")
# Add a longer delay to ensure dataset is fully ready
time.sleep(3)

# Debug available datasets and select the correct one
print("Available datasets:")
datasets = model.java.result().dataset()
dataset_name = None # Target the solution with stop

condition

for i, dataset in enumerate(datasets):
    current_name = dataset.name()
    print(f"Dataset {i}: tag={dataset.tag()}")

    name={current_name}")

    if current_name == dataset_name:
        print(f"Selected dataset name: {dataset_name}")
        break
    else:
        print(f"Could not find dataset '{dataset_name}'.")

Using default dataset.")

    dataset_name = None

# Test if the model is valid by evaluating comp1.p

pressure)

try:
    test_value = model.evaluate('comp1.p', unit=None,
dataset=dataset_name, inner='last', outer=None)
    print(f"Test evaluation of 'comp1.p' (pressure)
with dataset '{dataset_name or 'default'}': {test_value}")
except Exception as e:
    print(f"Failed to evaluate test variable 'comp1.p'
with dataset '{dataset_name or 'default'}': {e}")

# Evaluate comp1.length to debug stop condition
try:
    length_value = model.evaluate('comp1.length',
unit=None, dataset=dataset_name, inner='last', outer=None)
    print(f"Evaluation of 'comp1.length' with dataset
'{dataset_name or 'default'}': {length_value}")
except Exception as e:

```

```

        print(f"Failed to evaluate 'comp1.length' with
↳dataset '{dataset_name or 'default'}': {e}")

        # Evaluate dike_base to debug stop condition
        try:
            dike_base_value = model.evaluate('dike_base',
↳unit=None, dataset=dataset_name, inner='last', outer=None)
            print(f"Evaluation of 'dike_base' with dataset
↳'{dataset_name or 'default'}': {dike_base_value}")
        except Exception as e:
            print(f"Failed to evaluate 'dike_base' with dataset
↳'{dataset_name or 'default'}': {e}")

        # Try evaluating comp1.H_c without indexing
        try:
            h_c_value = model.evaluate('comp1.H_c', unit=None,
↳dataset=dataset_name, inner='last', outer=None)
            print(f"H_left = {value} m, H_c (using dataset
↳'{dataset_name or 'default}', inner=last) = {h_c_value}")
            if h_c_value != 0:
                print(f"Stop Condition 1 activated; H_c
↳determined as {h_c_value} m")
                critical_h_left = value
                H_c_array[j,z]=critical_h_left
                break
            else:
                print("Stop Condition 1 not activated; H_c is
↳0, continuing to next H_left")
        except Exception as e:
            print(f"Failed to evaluate comp1.H_c with dataset
↳'{dataset_name or 'default'}': {e}")
            print("Note: comp1.H_c might not be updated by the
↳Events > find H_c node. Please verify the stop condition and event settings.
↳")

        except Exception as e:
            print(f"Error during solve at H_left = {value} m: {e}")
            break

        if critical_h_left is not None:
            h_c_sell = model.evaluate('comp1.H_c_sell', unit=None,
↳dataset=dataset_name, inner='last', outer=None)
            print(f"Critical H_left where erosion begins:
↳{critical_h_left} m with H_c = {h_c_value} m")
            print(f"Critical H_left Sellmeijer 2011: {h_c_sell} m")
        else:

```

```

        print("No critical H_left found where erosion begins within
↳the sweep range.")

    else:
        raise Exception("Study 'std1' not found in the model.")

except Exception as e:
    print(f"Error: {e}")

#Store results in .csv file
df = pd.DataFrame(H_c_array)
df.to_csv(r"C:\Users\sytze\OneDrive - Delft University of
↳Technology\Q3_Thesis\Model\Python\H_c_array_6021B.csv")

```

```

[ ]: #Create save path
save_dir = r"C:\Users\sytze\OneDrive - Delft University of
↳Technology\Q3_Thesis\Afbeeldingen\Python"
fig, ax = plt.subplots()

#Load path to the stored results in H_c_array
file_array = r"C:\Users\sytze\OneDrive - Delft University of
↳Technology\Q3_Thesis\Model\Python\H_c_array_6021B.csv"
# Read the CSV file with semicolon delimiter
H_c_pd = pd.read_csv(file_array, delimiter=',')
H_c_pd=H_c_pd.set_index('Unnamed: 0')
H_c_array=np.array(H_c_pd)

#Create contour plot
CS = ax.contour(silt_array, lutum_array,H_c_array, colors='black',levels=np.
↳linspace(8.5, 14, 12))
for i in range(len(silt_array)):
    for j in range(len(lutum_array)):
        if i +j == 0:
            plt.scatter(silt_array[i], lutum_array[j], color='grey',
↳label='Results obtained from model')
        else:
            plt.scatter(silt_array[i], lutum_array[j], color='grey')
plt.scatter(5,7, marker='x', color='red', label='Silt and clay fraction of 6021
↳(location B)')
ax.clabel(CS, fontsize=10)
plt.xlabel('%silt')
plt.ylabel('%clay')
plt.title('Contour plot of H_c [m] for section 6021 (location B)')
plt.legend()
plt.grid(True, which='both', linestyle='--', alpha=0.7)
plt.minorticks_on()

```

```
#Save plot
plt.savefig(os.path.join(save_dir, 'Contourplot_6021_h_c_an1_black.png'),
            dpi=300, bbox_inches='tight')
```

